

**DOKUZ EYLÜL UNIVERSITY
GRADUATE SCHOOL OF NATURAL AND APPLIED
SCIENCES**

**SYNTHESIS OF SUPERCONDUCTING FILMS
AND IMPROVEMENT OF THEIR FLUX
PINNING PROPERTIES WITH BARIUM
ZIRCONATE NANOPARTICLES USING
CHEMICAL SOLUTION DEPOSITION METHOD**

by
Işıl BİRLİK

**June, 2011
İZMİR**

**SYNTHESIS OF SUPERCONDUCTING FILMS
AND IMPROVEMENT OF THEIR FLUX
PINNING PROPERTIES WITH BARIUM
ZIRCONATE NANOPARTICLES USING
CHEMICAL SOLUTION DEPOSITION METHOD**

**A Thesis Submitted to the
Graduate School of Natural and Applied Sciences of Dokuz Eylül University
In Partial Fulfillment of the Requirements for the Degree of Doctor of
Philosophy in Metallurgy and Materials Engineering, Metallurgy and Materials
Engineering Program**

**by
Işıl BİRLİK**

**June, 2011
İZMİR**

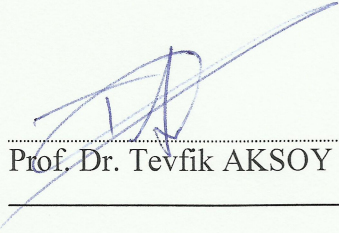
Ph.D. THESIS EXAMINATION RESULT FORM

We have read the thesis entitled “SYNTHESIS OF SUPERCONDUCTING FILMS AND IMPROVEMENT OF THEIR FLUX PINNING PROPERTIES WITH BaZrO₃ NANOPARTICLES USING CHEMICAL SOLUTION DEPOSITION METHOD” completed by İŞİL BİRLİK under supervision of PROF. DR. ERDAL ÇELİK and we certify that in our opinion it is fully adequate, in scope and in quality, as a thesis for the degree of Doctor of Philosophy.



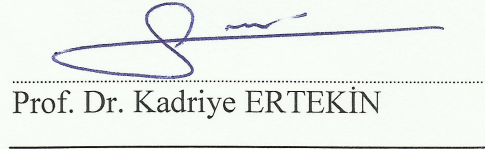
Prof. Dr. Erdal ÇELİK

Supervisor



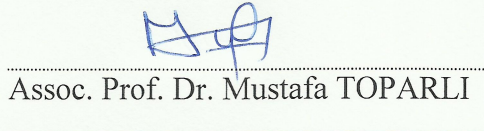
Prof. Dr. Tevfik AKSOY

Thesis Committee Member



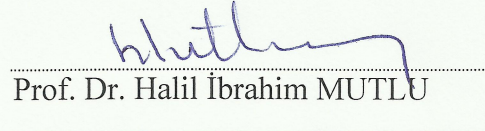
Prof. Dr. Kadriye ERTEKİN

Thesis Committee Member



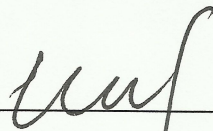
Assoc. Prof. Dr. Mustafa TOPARLI

Examining Committee Member



Prof. Dr. Halil İbrahim MUTLU

Examining Committee Member



Prof. Dr. Mustafa SABUNCU

Director

Graduate School of Natural and Applied Sciences

ACKNOWLEDGMENTS

First of all, I would like to express my deepest gratitude to my advisor Prof. Dr. Erdal elik for his constructive ideas and scientific guidance throughout the course of this thesis. I am proud to have had such an excellent advisor. I would also like to thank my committee members, Prof. Dr. Tevfik Aksoy and Prof. Dr. Kadriye Ertekin for reviewing my work and offering valuable suggestions about my thesis. I owe a huge debt of gratitude to the head of Leibniz Institute for Solid State and Materials Research Dresden (IFW), Prof. Dr. Ludwig Schultz and head of Superconducting Materials Group, Prof. Dr. Bernhard Holzapfel for their scientific guidance and great hospitality during my PhD studies in the IFW, Dresden.

I wish to extend special thanks to Assist. Prof. Dr. Funda Ak Azem for sincere assistance and support at all times. I would like to thank Esra Dokumacı, Aslıhan Süslü, Assist. Prof. Dr. Aylin Ziylan Albayrak, Mehtap Özdemir, Faruk Ebeođlugil, Mustafa Erol and Murat Bektaş for their kind friendship and helps. Additional thanks to my colleagues in IFW, Annia Kario and Manuela Erbe for their assistance and friendship during my stay in Dresden. I would also like to express my gratitude to each person that it would be impossible to name all here.

I gratefully acknowledge the financial assistance provided by The Scientific and Technological Research Council of Turkey (TUBITAK), under project number 109M054. Besides, I would also like to thank EU-FP6 Research Project "NanoEngineered Superconductors for Power Applications" NESPA no. MRTN-CT-2006-035619 which gave me the opportunity to get experience and perform measurements through nine months in IFW, Dresden.

Finally, I reserve my most sincere thanks to my family for their concern, confidence and support. I extend my greatest thanks to my husband İnanç who has been immeasurably receptive, incentive and patient with me during this time. No word can do justice to my appreciation for them.

Işıl BİRLİK

**SYNTHESIS OF SUPERCONDUCTING FILMS AND IMPROVEMENT OF
THEIR FLUX PINNING PROPERTIES WITH BARIUM ZIRCONATE
NANOPARTICLES USING CHEMICAL SOLUTION DEPOSITION
METHOD**

ABSTRACT

The present thesis demonstrates synthesis and characterization of BZO doped YBCO and GdBCO superconducting thin films on STO and LAO single crystal substrates using chemical solution deposition technique for high magnetic field applications. With this respect, transparent solutions were prepared both from commercially available YBCO powder and metal acetates separately by using different types of solvents as methanol, ethanol and propionic acid. Contact angle values of these solutions on STO and LAO substrates were determined to estimate their wettability features. A detailed rheological characterization was performed to determine shear profile and scrutinize effect of temperature on viscosity. The solutions were spin coated on the substrates and heat treated according to the profile. Thermal, microstructural and electrical properties of BZO doped superconducting thin films were determined through DTA-TG, FTIR, XRD, SEM-EDS, AFM, inductive critical transition temperature, inductive critical current density and transport measurements. The results show that six mol percentage BZO doped YBCO samples on both substrates possess the highest critical current density value for all magnetic fields. Additionally, GdBCO superconducting thin films exhibit higher critical transition temperature and self-field critical current density values in comparison to the YBCO films. According to the measurement results of GdBCO samples, the twelve mol percentage BZO doped GdBCO sample on STO substrate possess the highest critical current density value for all magnetic fields. These results indicate that the BZO dopant in the structure act as artificial pinning centers and increased the current carrying capability of films in magnetic field conditions.

Keywords: Chemical solution deposition, flux pinning, YBCO, GdBCO, BZO

KİMYASAL ÇÖZELTİ DEPOZİTLEME YÖNTEMİ KULLANILARAK SÜPERİLETKEN FİMLERİN ÜRETİLMESİ VE BARYUM ZİRKONAT NANOPARTİKÜLLERİ İLE AKI İĞNELENMESİ ÖZELLİKLERİNİN GELİŞTİRİLMESİ

ÖZ

Sunulan bu tez BZO katkılı YBCO ve GdBCO süperiletken ince filmlerin yüksek manyetik alan uygulamaları için STO ve LAO tek kristal altlıklar üzerine kimyasal çözelti depozitleme yöntemi ile sentezlenmesini ve karakterizasyonunu içermektedir. Bu bağlamda, ticari olarak temin edilen YBCO tozları ve metal asetat başlangıç kimyasalları ile metanol, etanol ve propiyonik asit çözücüleri kullanılarak saydam çözeltiler hazırlanmıştır. Kayma profilinin belirlenmesi ve sıcaklığın vizkozite üzerindeki etkisinin incelenmesi için kapsamlı bir reolojik karakterizasyon çalışması yapılmıştır. Hazırlanan çözeltiler spin kaplama ile altlıklar üzerine kaplanmış ve ısıtma işlemi uygulanmıştır. BZO katkılı süperiletken filmlerin termal, mikroyapısal ve elektriksel özellikleri DTA/TGA, FTIR, XRD, SEM, AFM, indüktif kritik geçiş sıcaklığı, indüktif kritik akım yoğunluğu ve transport ölçümleri ile belirlenmiştir. Sonuçlar, yüzde altı mol BZO katkılı YBCO örneklerinin her iki altlık üzerinde manyetik alan altında en yüksek kritik akım yoğunluğu değerine sahip olduğunu göstermektedir. Buna ilave olarak, GdBCO süperiletken ince filmleri YBCO filmlere göre daha yüksek kritik geçiş sıcaklığı ve kritik akım yoğunluğu değerlerine sahiptir. GdBCO örneklerinde yapılan ölçüm sonuçlarına göre, yüzde oniki mol BZO katkılı örnekler, STO altlık üzerinde tüm manyetik alan değerlerinde en yüksek kritik akım yoğunluğu değerine sahiptir. Bu sonuçlar, BZO katkısının yapı içerisinde yapay iğneleme merkezleri olarak etki ettiğini ve manyetik alan altında akım taşıma kapasitesinin arttığını göstermektedir.

Anahtar sözcükler: Kimyasal çözelti depozitleme, akı iğnelenmesi, YBCO, GdBCO, BZO

CONTENTS

	Page
PhD. THESIS EXAMINATION RESULT FORM	ii
ACKNOWLEDGEMENT	iii
ABSTRACT	iv
ÖZ	v
CHAPTER ONE-INTRODUCTION	1
1.1 Background	1
1.2 Overview of the Thesis	3
CHAPTER TWO-FUNDAMENTALS OF SUPERCONDUCTIVITY	5
2.1 Introduction to Superconductivity	5
2.2 Elementary Theories of Superconductivity	9
2.2.1 The London Theory	9
2.2.2 The Ginzburg-Landau Theory	10
2.2.3 Type I and Type II Superconductors	11
2.2.4 Mixed State	12
2.3 Fundamental Properties of YBCO	13
2.3.1 Crystal Structure	13
2.3.2 Oxygen Stoichiometry	15
2.3.3 Irreversibility Line	17
2.3.4 Anisotropy Factor	18
2.4 Flux Vortices, Pinning and Critical Currents in Type II Superconductors	19
2.4.1 Flux Vortices	19
2.4.2 Flux Flow	22
2.4.3 Flux Pinning	23
2.4.4 Flux Creep	24
2.4.5 Sources of Pinning	24
2.5 YBCO Thin Films	25

2.5.1 Artificial Pinning Centers in YBCO Thin Films.....	26
2.6 Applications of Superconductors	28
CHAPTER THREE-CHEMICAL SOLUTION DEPOSITION.....	31
3.1 Deposition Methods for Superconducting Thin Films	31
3.1.1 Physical Deposition Methods.....	31
3.1.2 Chemical Deposition Methods	32
3.1.2.1 Aqueous Deposition.....	34
3.1.2.2 Sol-Gel Process.....	34
3.1.2.3 Metalorganic Decomposition.....	35
3.2 Steps of Chemical Solution Deposition Method.....	35
3.2.1 The Precursor Solution Synthesis.....	37
3.2.2 Precursor Solution Coating	39
3.2.3 Pyrolysis.....	41
3.2.4 Nucleation and Crystal Growth.....	42
CHAPTER FOUR-EXPERIMENTAL STUDIES	53
4.1 Substrate Materials	53
4.2 Production Procedures.....	54
4.2.1 Solution Preparation	54
4.2.2 Coating Procedure	57
4.2.3 Heat Treatment.....	58
4.3 Solution Characterization	59
4.3.1 Viscosity Measurement	59
4.3.2 Contact Angle Measurement.....	60
4.4 Material Characterization	60
4.4.1 Differential Thermal Analysis-Thermogravimetry (DTA-TG)	60
4.4.2 Fourier Transform Infrared Spectroscopy (FTIR).....	61
4.4.3 X-Ray Diffraction (XRD)	63
4.4.4 Scanning Electron Microscopy (SEM).....	65

4.4.5 Atomic Force Microscopy (AFM)	66
4.5 Electrical Characterization.....	67
4.5.1 Inductive T_c Measurement	67
4.5.2 Inductive J_c Measurement	70
4.5.3 Transport Measurement	70
CHAPTER FIVE-RESULTS AND DISCUSSION.....	73
5.1 YBCO Thin Film Production from Commercially Available Oxide Powder ..	73
5.1.1 Preparation and Characterization of Precursor Solution from YBCO Powder.....	73
5.1.2 Preparation and Structural Characterization of YBCO Thin Films	79
5.1.3 Electrical Characterization of YBCO Thin Films	82
5.2 YBCO Thin Film Production from Acetate Based Precursors	84
5.2.1 Preparation and Characterization of Acetate-based Precursor Solutions ..	85
5.2.2 Detailed Heat Treatment and Process Route Investigation of Superconducting YBCO Thin Film Production.....	90
5.2.3 Structural Properties of YBCO Thin Films Prepared from Methanol-, Ethanol- and Propionic acid-Based Solutions with BZO Pinning Centers	94
5.2.4 Superconducting Properties of YBCO Thin Films Prepared from Methanol-, Ethanol- and Propionic acid-Based Solutions with BZO Pinning Centers.....	107
5.3 GdBCO Thin Film Production from Gd-acetate based Precursor	116
5.3.1 Precursor Solution Characterization.....	118
5.3.2 Crystallization Temperature Determination for GdBCO Thin Films.....	121
5.3.3 Structural Properties of GdBCO Thin Films with BZO Pinning Centres	125
5.3.4 Superconducting Properties of GdBCO Thin Films with BZO Pinning Centres.....	131
CHAPTER SIX-CONCLUSIONS AND FUTURE PLANS	136
REFERENCES.....	141

CHAPTER ONE

INTRODUCTION

1.1 Background

Superconductivity was first discovered in 1911 by the Dutch physicist, Heike Kammerlingh Onnes. He discovered that the electrical resistance goes to zero when mercury is cooled at about 4.2 K (Onnes, 1911). Later researches showed that many metals, such as lead, tin, niobium were also superconductive when cooled to extremely low temperatures. Initial materials identified to be superconductive were elemental metals like Hg, Pb, Nb, followed by solid solutions like NbTi and intermetallics Nb₃Sn, V₃Si and Nb₃Ge.

The first widely-accepted theoretical understanding of superconductivity was outlined in 1957 by American physicists John Bardeen, Lean Cooper and John Schrieffer. Their theory of superconductivity known as the BCS Theory (Bardeen, Cooper, & Schrieffer, 1957). Superconductivity remained interesting but of little practical use because of low “cryogenic” temperatures. Progress at this research area was extremely slow up and until 1986, the highest critical transition temperature (T_c) achieved was 23 K. Liquid helium was still required for cooling. Then in 1987, a truly breakthrough discovery was made. Alex Müller and Georg Bednorz created a brittle ceramic lanthanum, barium, copper and oxygen compound that has a T_c of 35 K, (12 degrees above the old record for a superconductor). This discovery was so remarkable because ceramics normally do not conduct electricity well at all so, researchers had not considered them as possible superconductor candidates (Bednorz, & Müller, 1987). Once the barrier was broken, hundreds of scientists rushed to try various chemical compounds to see which one would give the highest T_c . In March of 1987, during the American Physical Society meeting, a perovskite ceramic material, YBa₂Cu₃O_{7- δ} (YBCO), was announced to superconduct at 92 K. That was a significant discovery because it became possible to use liquid nitrogen as a coolant which is a commonly available one inasmuch as these materials superconduct at significantly higher temperatures; they are referred as “High

Temperature Superconductors (HTS)”. Subsequently, attention was focused on copper oxides and the compound bismuth lead strontium calcium copper oxide was found with T_c of 105 K that was followed by the discovery in 1988 of thallium barium calcium copper oxide with $T_c = 125$ K. Almost 5 years elapsed before the mercury compounds boosted the T_c record to 133 K. Under extremely high pressure, it is possible to push up T_c over 150 K (Sheahen, 2002).

The discovery of HTS conductors led to an unprecedented explosion of research and development efforts world-wide because of the significant potential for practical applications. Superconductivity is considered as one of the technologies which can prevent environmental destruction by allowing energy to be used with high efficiency. The possibility of practical applications of superconductivity depends on the maximum current density which superconductors can carry, the value of losses which superconductors consume, the maximum magnetic field strength in which superconductors can be used, etc. These factors are directly related to the flux pinning of quantized magnetic flux lines in superconductors. Also, pinning interactions between various defects and individual flux lines, maximum pinning strength of defects, shape and size of pinning centers are key parameters that effect mechanisms of pinning.

Since their discovery, significant progress has been made in the fabrication of high quality, low-cost YBCO superconducting thin films. A major challenge facing the commercialization of HTS conductors is reducing the cost of manufacturing while maintaining the performance required for practical applications. Various processes to fabricate YBCO superconducting films are proposed as pulsed laser deposition method (PLD), physical vapour deposition (PVD), chemical vapor deposition (CVD) and chemical solution deposition (CSD). Of these techniques, CSD processing has the potential to realize such a cost saving approach and is considered to be one of the most promising techniques for the preparation of high temperature superconductor films without use of high vacuum techniques. Easy precise composition control of the final product and a convenient way of coating on long length metal tapes and on large area substrates are advantages of this process

(Yamagiwa et al., 2001). CSD film fabrication can be grouped as sol-gel process and metal organic deposition (MOD) techniques.

The sol-gel technique offers a low temperature method for synthesizing materials which are totally inorganic in nature or composed of inorganic and organics. This process can produce thin bond coating to provide excellent adhesion between the metallic substrate and the top coat. Resultant products have high homogeneity and purity (Bhuiyan, Paranthaman & Salama, 2006).

Metal organic deposition has a cost advantage over most of other CSD techniques employed for HTS film preparation. A precise control of the composition and formation of large films are also easy by means of MOD. One of the most important MOD processes for the fabrication of YBCO films uses trifluoroacetates to prepare fluorinated precursor films, from which superconducting films are synthesized by heating them in a humid atmosphere (Iguchi, Araki, Yamada, Hirabayashi & Ikuta, 2002). YBCO films fabricated by trifluoroacetic acid-metalorganic deposition (TFA-MOD) exhibit high superconducting critical temperatures and high critical current densities under high magnetic field conditions. The artificial pinning centers that are added into the structure at the solution preparation step contribute to the enhancement of the pinning efficiency.

1.2 Overview of the Thesis

In this work, we have studied the characterization of high temperature $\text{REBa}_2\text{Cu}_3\text{O}_{7-\delta}$ (REBCO, RE: Y and Gd) superconducting thin films prepared by the TFA-MOD process onto single crystal substrates. Solution characterization was performed by measuring contact angle and viscosity of solutions. In order to use suitable process regime, define chemical structure and reaction type of intermediate temperature products, Differential Thermal Analysis-Thermogravimetry (DTA-TG) and Fourier Transform Infrared (FTIR) devices were used prior to the film production. Structural analysis of the produced films was performed using multipurpose X-Ray Diffraction (XRD) and surface morphology was investigated

using Scanning Electron Microscopy/Energy Dispersive Spectroscopy (SEM/EDS) and Atomic Force Microscopy (AFM). The critical transition temperature (T_c) and critical current density (J_c) of the films were measured by an inductive method. Transport measurements up to 7 T at 77 K on bridges of 0.8 mm length and 50 μm widths were carried out with a physical properties measurement system (PPMS). The correlation of optimum dopant concentration with microstructure, pinning and superconducting properties was investigated and discussed in this concept.

In Chapter 2, fundamental properties and elementary theories of superconductivity is presented. Crystal structure of YBCO high temperature superconductors are discussed in detail. Pinning mechanisms and artificial pinning centers are explained for YBCO thin films. Finally a summary of application fields of superconductors are described.

In Chapter 3, deposition methods for superconductor thin films and film growth processes are described in detail. Steps of chemical solution deposition method are explained.

Chapter 4 concerns measurements performed on superconducting thin film growth. All characterization techniques are described briefly.

Chapter 5 covers the synthesis and characterization of thin films. First section deals with the YBCO system and investigates the effects of BaZrO_3 (BZO) artificial pinning centers into the thin films prepared separately from four different kinds of precursor solutions. The differences between powder precursors and acetate precursors as well as solvents and their effect on thin film structure are presented. Additional to YBCO system, GdBCO thin films are also presented in the last section.

Finally, we present the general conclusions of this study and future plans about the work.

CHAPTER TWO

FUNDAMENTALS OF SUPERCONDUCTIVITY

2.1 Introduction to Superconductivity

The superconductors are materials that lose electric resistance below a certain critical temperature, T_c . Kammerlingh Onnes who discovered the superconductivity first, pointed out that the electrical resistance goes to zero when mercury is cooled at about 4.2 K. Later research showed that many metals, such as lead, tin, niobium were also superconductive when cooled to extremely low temperatures (Goebel, 2005).

The mechanism to avoid the dissipation of the superconducting state is the weak coupling of a conduction electron with another one in the form of pairs, called Cooper pairs. They can flow without any dissipation, there is no scattering of the “individual” pairs with atoms or impurities, and therefore there is no resistivity. The correlation distance between two electrons of the Cooper pair is named the coherence length, $\xi(T)$.

According to BCS theory, as one negatively charged electron passes by positively charged ions in the conductor lattice, the lattice distorts. This in turn causes phonons to be emitted which form a trough of positive charges around the electron. Figure 1 illustrates a wave of lattice distortion due to attraction to a moving electron. Before the electron passes by and the lattice springs back to its normal position, a second electron is drawn in to the trough. Then the two electrons which should repel one another, link up. The forces exerted by the phonons overcome the electrons natural repulsion. The electron pairs are coherent with one another as they pass through the conductor in unison. The electrons are screened by the phonons and are separated by some distance. When one of the electrons that make up a Cooper pair and passes close to an ion in the crystal lattice, the attraction between the negative electron and the positive ion cause a vibration to pass from ion to ion until the other electron of the pair absorbs the vibration. The net effect is that the electron has emitted a phonon and the other electron has absorbed the phonon. It is this exchange that keeps the

Cooper pairs together. It is important to understand that the pairs are constantly breaking and reforming. Since the electrons are indistinguishable particles, it is easier to think of them as permanently paired (Whelan, 2003).

The Cooper pairs within the superconductor are supercurrent carriers and they experience perfect conductivity. From a mathematical aspect, cooper pair is more stable than a single electron within the lattice, it experiences less resistance. In addition, physically the cooper pair is more resistant to vibrations within the lattice therefore pairs move through the lattice relatively unaffected by thermal vibrations below the critical temperature (Shekhter, Galperin, Garelik, Isacsson, & Jonson, 2003).

The phonon-linkage mechanism associated with cooper pairs in low-temperature superconductor can not work at high temperatures, since thermal vibrations would quickly break the phonon linkages. The most popular theory is that the pair coupling occurs due to subtle magnetic effects created by the HTS lattice, but there is not a clear explanation how it occurs.

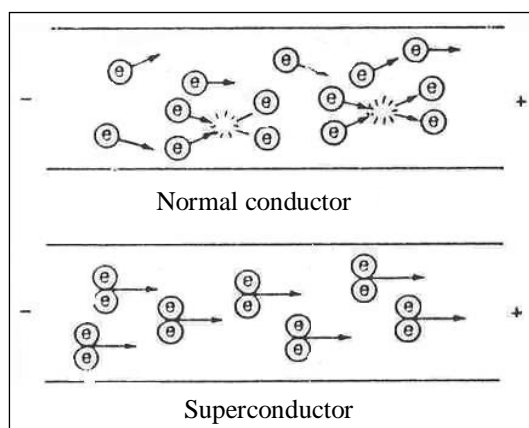


Figure 2.1 Schematic illustrating the difference, according to the BCS theory, between normal conduction and zero-resistance superconduction (Shekhter et al., 2003).

The BCS theory successfully shows that electrons can be attracted to one another through interactions with the crystalline lattice. This occurs despite the fact that

electrons have some charge when the atoms of the lattice oscillate as positive and negative regions; the electron pair is alternatively pulled together and pushed apart without a collision. The electron pairing is favorable because it has the effect of putting the material into a lower energy state. When electrons are linked together in pairs, they move through the superconductor in an orderly fashion.

By 1933 W. Meissner and R. Ochsenfeld discovered that superconductors are more than a perfect conductor of electricity and they also have an interesting magnetic property of excluding a magnetic field. A superconductor will not allow a magnetic field to penetrate its interior. It causes currents to flow that generate a magnetic field inside the superconductor that just balances the field that would have otherwise penetrated the material. This effect is called as the Meissner Effect (Sheahen, 2002).

Once a magnetic field is applied to a superconductor at a temperature below T_c , surface currents flow so that the magnetic field they generate just cancels the applied field within the material. Because the net flux in the material is zero the superconductor behaves like a perfect diamagnet (Warnes, 2003).

Diamagnetism involves the way a magnetic field interacts with a material. A nondiamagnetic material will not be affected by a magnetic field. The lines of a magnetic force will penetrate the material as if it were not there. In a diamagnetic material, the magnetic field does not penetrate, but is repelled. This phenomenon is illustrated in Figure 2.2.

This ‘perfect diamagnetism’ demonstrates that superconductivity is a true thermodynamic state and that in moving from the normal to the superconducting state, a material undergoes a thermodynamic phase transition. In order for this to happen, the overall free energy must be lower in the superconducting state than in the normal state and this energy difference, which depends on the temperature, is known as the condensation energy.

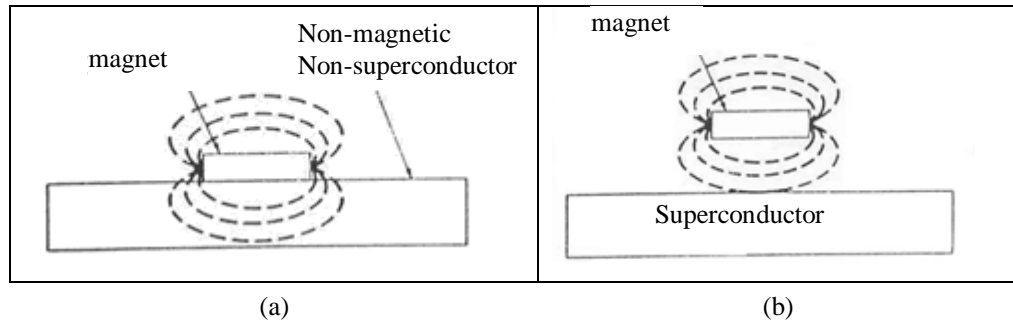


Figure 2.2 Comparison between the interaction of a magnet with (a) a nondiamagnetic material and (b) a diamagnetic superconductor (Whelan, 2003).

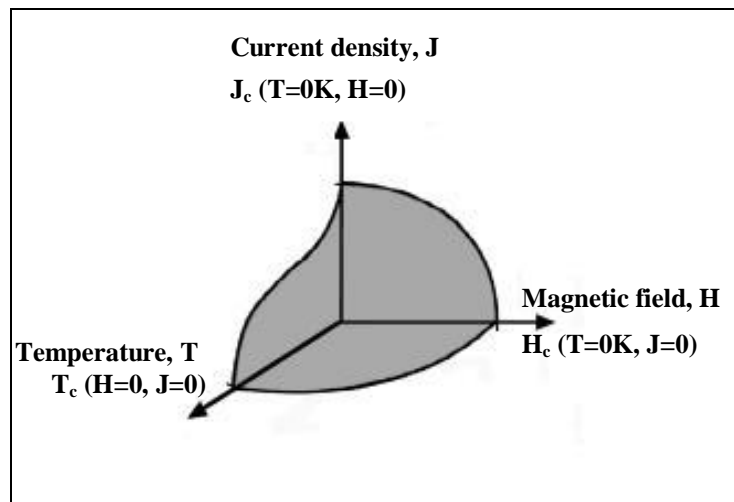


Figure 2.3 Critical temperature, current density and magnetic field boundary separating superconducting and normal conducting states (Callister, 2000).

When a magnetic field is applied to a material in the superconducting state, energy is required to prevent it from penetrating. If that is larger than the condensation energy, the material will lower its overall free energy by returning to its normal state. Thus there is a critical magnetic flux density, B_c , which is a function of temperature:

$$f_n(T) - f_s(T) = \frac{B_c^2(T)}{2\mu_0} \quad (2.1)$$

where f_n and f_s are the Helmholtz free energies of the normal and superconducting states respectively and μ_0 is the permeability of free space. In addition to the

requirement that the temperature and magnetic field must be below some value, there is also a limit on the current density in a superconducting material. Hence the three critical values T_c , H_c and J_c , which are all interdependent, are shown in Figure 2.3, and a material will only remain in the superconducting state within the volume shaded.

2.2 Elementary Theories of Superconductivity

2.2.1 The London Theory

Two equations describing electrodynamics in superconductors were proposed by F. and H. London (1935). This model is not derived from physical principles, justified from observations of behavior. Therefore it is a phenomenological theory. F. and H. London proposed the following equations to govern the microscopic electric field, \mathbf{E} , and magnetic field, \mathbf{h} , in superconductors.

$$\mathbf{E} = \frac{\partial}{\partial t} (\Lambda \mathbf{J}_s) \quad (2.2)$$

$$\mathbf{h} = -\nabla \times (\Lambda \mathbf{J}_s) \quad (2.3)$$

where;

$$\Lambda = \mu_o \lambda_L^2 = m_e / n_s e^2 \quad (2.4)$$

for a number density of superconducting electrons n_s , where \mathbf{J}_s is the supercurrent density and m_e the electronic mass. Equation 2.2 is an acceleration equation which describes the perfect electrical conductivity.

Equation 2.3 may be combined with the Maxwell equation $\nabla \times \mathbf{h} = \mu_o \mathbf{J}$;

$$\nabla^2 \mathbf{h} = \mathbf{h} / \lambda_L^2 \quad (2.5)$$

to give the solution of which is the exponentially decaying $\mathbf{h}=\mathbf{h}_0\exp(-x/\lambda_L)$, i.e. the magnetic field is screened from the interior of a sample within a distance λ_L , known as the ‘penetration depth’ (London & London, 1935).

2.2.2 The Ginzburg-Landau Theory

In 1950, Ginzburg and Landau proposed a theory based on Landau’s general theory of 2nd order phase transitions. The superconducting electrons were described by a complex wave function, ψ , such that $ns=|\psi|^2$. By expanding the expression for the free energy, a differential equation may be derived for ψ :

$$\frac{1}{2m} (-i\nabla + 2e\mathbf{A})^2 \psi + (\alpha + \beta\psi\psi^*)\psi = 0 \quad (2.6)$$

The supercurrent density is given by:

$$\mathbf{J}_s = \frac{ie}{m} (\psi^* \nabla \psi - \psi \nabla \psi^*) - \frac{4e^2}{m} \mathbf{A} \psi \psi^* \quad (2.7)$$

where \mathbf{A} is the magnetic vector potential such that $\mathbf{B} = \text{curl } \mathbf{A}$.

The Ginzburg-Landau equations lead to two characteristic lengths, the G-L penetration depth, λ_{GL} ,

$$\lambda_{GL} = \sqrt{(m\beta / 4\mu_0 e^2 |\alpha|)} \quad (2.8)$$

and the coherence length, ξ

$$\xi = \sqrt{(\hbar^2 / 2m|\alpha|)} \quad (2.9)$$

in which α is proportional to $(T-T_c)$ and β is approximately independent of T .

The penetration depth is, like the London penetration depth, the characteristic length for the decay of the magnetic field in a superconductor. The coherence length may be described as the length scale over which the order parameter varies. As both λ_{GL} and ξ are inversely related to α , they are dependent on temperature and both diverge as T approaches T_c . However, the ratio of the parameters,

$$K = \lambda_{GL} / \xi \quad (2.10)$$

This is known as the Ginzburg-Landau parameter, does not depend on α and is therefore approximately independent of temperature (Ginzburg & Landau, 1950).

2.2.3 Type I and Type II Superconductors

Type I superconductors are materials that completely expel magnetic flux from their interior, by means of surface currents. The distance of the sample region through which the surface currents flow is called superconducting penetration depth, $\lambda(T)$. Type I superconductors are very pure metals that typically have critical fields too low for use in superconducting magnets.

In 1957, Abrikosov showed that solutions of the Ginzburg-Landau equations fall into two distinct categories. For $\kappa < 1/\sqrt{2}$, the surface energy of the interface between the normal and superconducting phases is positive. Thus the behavior noted by Meissner is observed, whereby flux is completely excluded from the material below T_c . This behavior is known as Type I.

However, for $\kappa > 1/\sqrt{2}$, the surface energy of a normal/superconducting interface is negative and it will therefore be energetically favorable for flux to exist within the superconducting material. It is called Type II behavior. In order to achieve the minimum energy state, the area of the boundary between superconducting and normal material is maximized and so the normal regions are subdivided until a quantum limit is reached. Thus for Type II materials, there are two critical induction fields: the lower critical field \mathbf{B}_{c1} and the upper critical field \mathbf{B}_{c2} . The flux is

completely expelled only up to the induction field \mathbf{B}_{c1} . In applied induction fields smaller than \mathbf{B}_{c1} , the type II superconductor behaves like as type I superconductor. Above \mathbf{B}_{c1} the magnetic flux partially penetrates into the material until the upper critical field \mathbf{B}_{c2} , is reached. Above \mathbf{B}_{c2} the material reaches the normal state (Abrikosov, 1957).

2.2.4 Mixed State

Between \mathbf{B}_{c1} and \mathbf{B}_{c2} the superconductor is said to be in the mixed state in which the magnetic flux partially penetrates the superconducting specimen in the form of tiny microscopic filaments called vortices, each one containing a flux quantum (Figure 2.4). A vortex consists of a normal core (size in the order of $\sim\xi$), in which no Cooper pairs exist, surrounded by a superconducting region (size in the order of $\sim\lambda$) in which a persistent supercurrent flows, which generates a field within the core equivalent to a flux quantum. The number of vortices gradually increases as the field is raised from \mathbf{B}_{c1} to \mathbf{B}_{c2} .

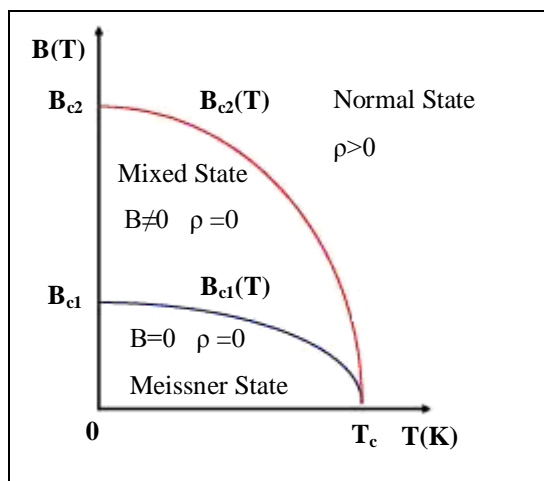


Figure 2.4 Magnetic phase diagram of a Type-II superconductor. The variations of \mathbf{B}_{c1} and \mathbf{B}_{c2} as a function of temperature illustrated (Gonzales, 2005).

When a current density (\mathbf{J}) is applied to a type II superconductor in the mixed state, the Lorentz force ($\mathbf{F}_L = \mathbf{J} \times \mathbf{B}$) acts on the vortex leading to flux motion if there is no barrier for flux motion. When vortices move at the velocity of \mathbf{v} , an electric field (\mathbf{E}) is created in the direction of the current as $\mathbf{E} = \mathbf{v} \times \mathbf{B}$ and a voltage appears. This creates non-desirable energy dissipation and a zero-resistance state is obtained. In real materials, there are impurities and imperfections in the atomic lattice to pin these vortices (F_p , pinning force) and avoid their movement and therefore dissipation.

Thanks to this partial flux penetration, the material can withstand strong applied magnetic fields without ongoing to the normal state. Superconductivity does persist in the mixed state up to the upper critical field \mathbf{B}_{c2} .

For high power applications, type II superconductors are the only candidates to transport high currents in high magnetic fields. The high temperature superconductors (HTS) are ceramic compounds (type II) based on copper oxides, they have critical temperatures close to 100 K. One of the compounds more intensely studied is YBCO. It has a critical temperature of ~ 92 K. This temperature is higher enough to enable to use liquid nitrogen (77 K) as cooling liquid, thus enlarging its engineering applications to power applications.

Nowadays, the low T_c superconductors can be explained by the weak coupling of Cooper pairs (electron-electron coupling via a phonon) described by the BCS theory developed in 1957. Nevertheless, the HTS can not be explained by the BCS theory, because it is not possible to explain the coupling energy necessary at high temperatures. Other strong-electron coupling theories are required.

2.3 Fundamental Properties of YBCO

2.3.1 Crystal Structure

After the discovery of the superconducting ceramic system La-Ba-Cu-O with critical transition temperature 30-40 K, other families of copper-oxide based

ceramics have been synthesized with higher critical temperatures. These oxides include the Y-Ba-Cu-O series ($T_c=90$ K), Bi-Sr-Ca-Cu-O series ($T_c=80-115$ K) and the Tl-Ba-Ca-Cu-O group ($T_c=85-125$ K). YBCO remains the most studied ceramic superconductor in spite of the fact that other ceramic oxide systems have been found to have higher T_c 's than YBCO (Alecu, 2004).

The unit cell of YBCO is based on a stack of three perovskite cells as shown in Figure 2.5 and the lattice type is either tetragonal or orthorhombic, depending on the oxygen content. The central perovskite cell contains a Y atom, sandwiched between CuO_2 planes. Adjacent to the CuO_2 planes are layers of BaO_2 and at the top and bottom of the cell there are Cu-O chains which have variable oxygen content, dependent upon the overall oxygenation level of the material.

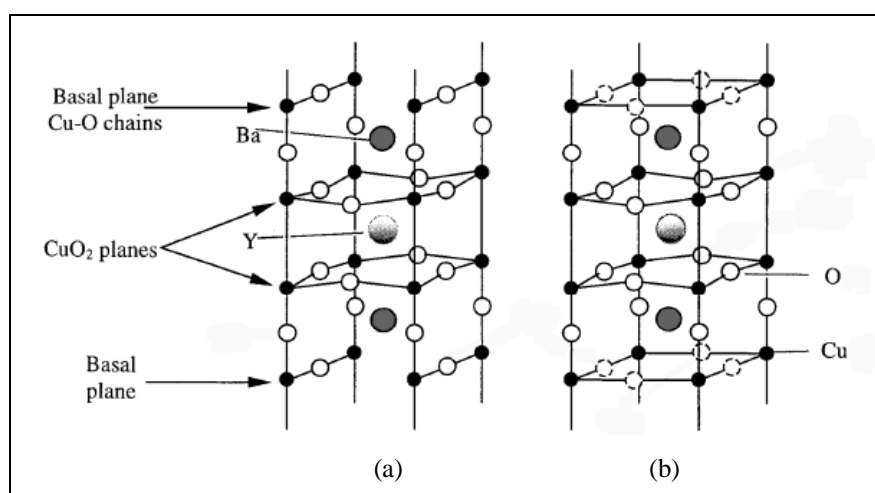


Figure 2.5 Unit cell of (a) $\text{YBa}_2\text{Cu}_3\text{O}_7$ and (b) $\text{YBa}_2\text{Cu}_3\text{O}_{7-\delta}$. The dashed circles indicate oxygen sites which are partially filled (Rutters, 2001).

The crystal structure may be represented as in Figure 2.6. Each square based pyramid has O atoms at its apices and a Cu atom at the centre of the base. The square Cu-O sheets have an O atom at each corner and a Cu atom at the centre. Note that in order to show two complete blocks of CuO_2 planes, the origin of Figure 2.6 is shifted by $(0,0,1/2)$ relative to the conventional cell shown in Figure 2.5 (Shaked, Keane, Rodriguez, Owen, Hitterman, & Jorgensen, 1994).

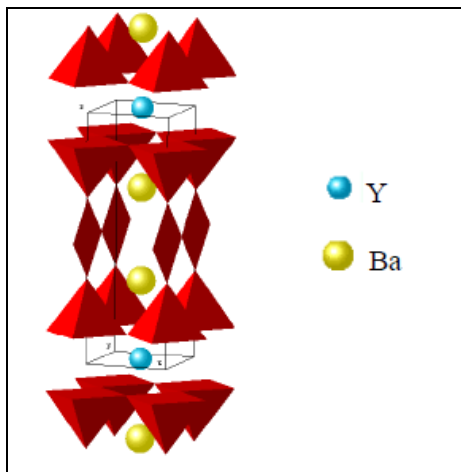


Figure 2.6 The crystal structure of YBCO. The pyramids have O atoms at the apices and Cu atoms at the centre of the base (Shaked et al., 1994).

2.3.2 Oxygen Stoichiometry

The variation of the oxygen content in $\text{YBa}_2\text{Cu}_3\text{O}_{7-\delta}$ is extremely important in determining the superconducting properties. The effect of reducing the oxygen content below 7 atoms per unit cell is depicted in Figure 2.7. In all of the HTS cuprates, charge doping plays a critical role in determining the superconducting properties as shown in Figure 2.8. For YBCO superconductor, the charge carriers are holes. By varying the charge concentration through chemical substitutions or changes in the oxygen stoichiometry, the transport properties of the YBCO can be varied from superconducting to insulating.

Also important for the superconducting properties of YBCO is the existence of chains of Cu-O atoms, which have metal-like electrical properties and reduce the anisotropy of the superconductor. The variation of the unit cell parameters of YBCO with oxygen content is shown in Figure 2.9, which demonstrates the tetragonal-orthorhombic transition at around $\delta=0.6$ (Cyrot, & Pavuna, 1995).

It is well established that YBCO can exist in at least two different structures, depending on the overall oxygen content and ordering of the oxygen atoms in the

CuO basal planes. In the tetragonal phase the oxygen sites in the CuO basal planes are occupied at random and the material is insulating. The high- T_c YBCO (92 K) compound has orthorhombic symmetry and exhibits complete ordering of the oxygen atoms in one dimensional CuO chains along the b-axis, called metallic chains. For an oxygen content of $\delta \sim 0.6$, a tetragonal to orthorhombic phase transition is observed and furthermore a decrease of the c parameter with increasing oxygen content is also observed in Figure 2.9.

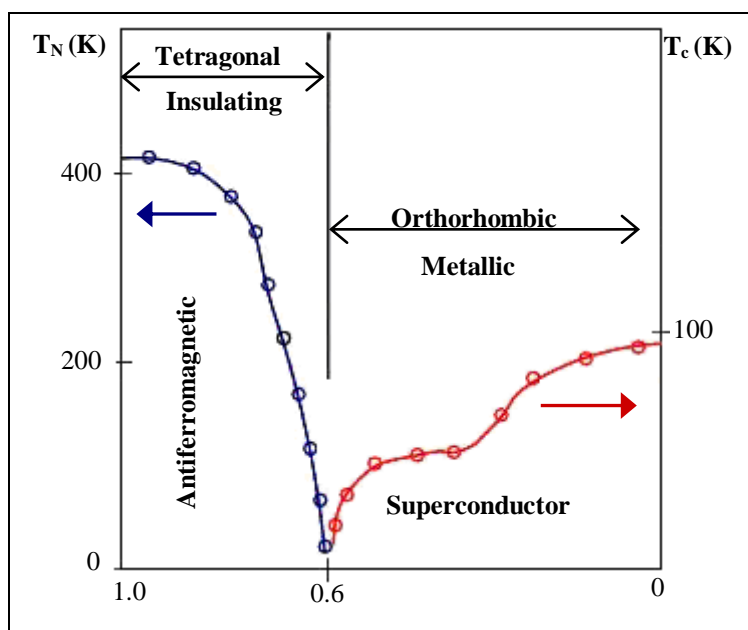


Figure 2.7 The effect of oxygen content on the T_c of $\text{YBa}_2\text{Cu}_3\text{O}_{7-\delta}$ (Cyrot et al., 1995).

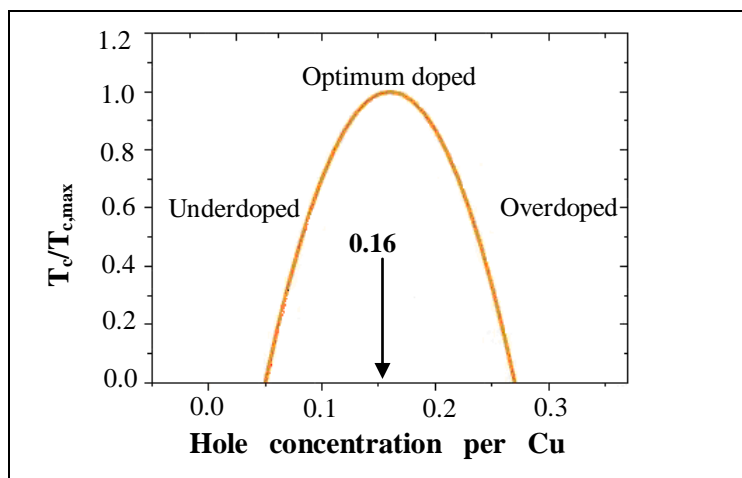


Figure 2.8 Doping curve of maximum charge carrier.

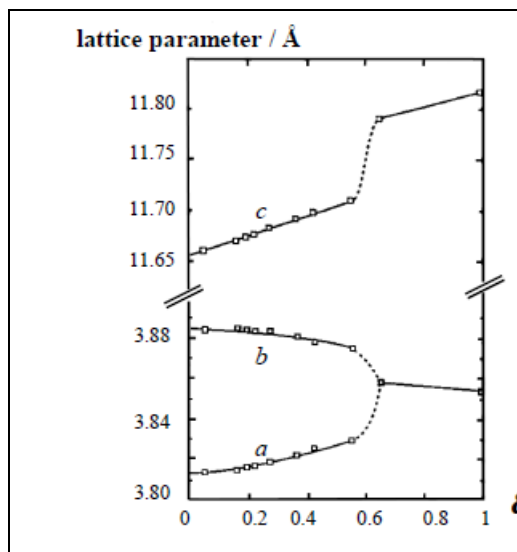


Figure 2.9 The unit cell parameters of YBCO as a function of the oxygen content (Waldram, 1996).

2.3.3 Irreversibility Line

An important property of YBCO relates to the ability of this material to carry significant currents at high magnetic induction field and as any type II superconductor, magnetic induction field penetrate the HTS cuprates in the form of vortices in the mixed state. At a given temperature, each HTS material has a maximum magnetic field, \mathbf{B}_{irr} , above which loss-free dc current flow is not possible, dissipation starts due to motion of vortices at any small applied current, i.e. the mixed state enters to a reversible state where $\mathbf{J}_c=0$.

The field-temperature line ($\mathbf{B-T}$) dividing $J_c \neq 0$ from the $J_c=0$ states is defined as the irreversibility line (IL). This line is very important for application purpose since it sets the position from where the material is not anymore useful even though it is still in the superconducting state. Figure 2.10 shows IL for typical superconductors and temperatures of cryogenic liquids. As it is denoted in Figure 2.10, YBCO is the best candidate for high-power applications at 77 K at high external magnetic fields.

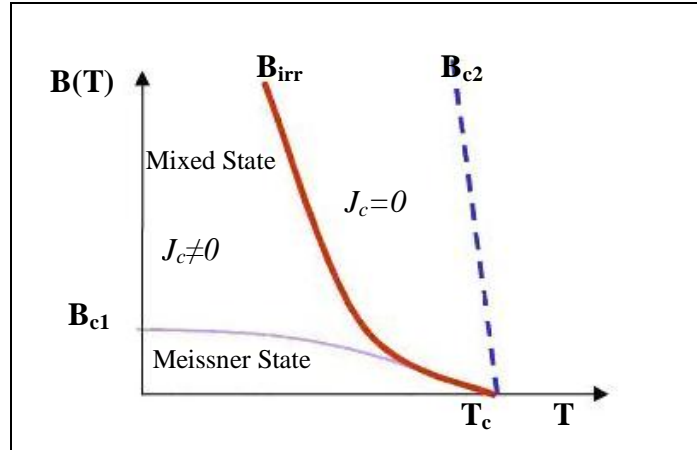


Figure 2.10. Scheme of irreversibility line \mathbf{B}_{irr} and the critical magnetic fields \mathbf{B}_{c1} and \mathbf{B}_{c2} as a function of temperature (Gonzales, 2005).

2.3.4 Anisotropy Factor

The large anisotropy of the crystal structure has consequences for the physical properties as the effective mass of the electrons moving in the a-b plane, m_{ab} , is different from that in the c direction, m_{c} . This difference is characterized by an anisotropy parameter, γ , such that $\gamma^2 = m_{\text{c}}/m_{\text{ab}}$. The anisotropy parameter is a measure of the ratio of the coherence length and the penetration depth in the a-b plane and c-direction. For YBCO, γ is approximately 5-7 as demonstrated by the values shown in Table 2.1 (Datta, 1992).

Table 2.1 Anisotropy of ξ and λ in YBCO (T=0 K) (Datta, 1992).

	Coherence length ξ (nm)	Penetration depth λ (nm)
a-b plane	2	140
c-direction	0.3	900

The layered structure of HTS leads to a very anisotropic materials. The superconducting coherence length, $\xi(T)$, is defined as the correlation distance between two electrons of the Cooper pair, is then also anisotropic and quite small in the YBCO compound. The typical values for YBCO are in the order of atomic space, $\xi_{\text{ab}}(T) \sim 30 \text{ \AA}$, $\xi_{\text{c}}(T) \sim 4 \text{ \AA}$. The conductivity in the a-b plane is then also very different from the one in the c-direction, thus it tends to flow mainly along a-b planes, i.e.

$J_c^{ab} \gg J_c^c$. Therefore, for high power applications we need the YBCO c-axis grains grown perpendicular to the substrate as illustrated in Figure 2.11 (Zheng et al., 1994).

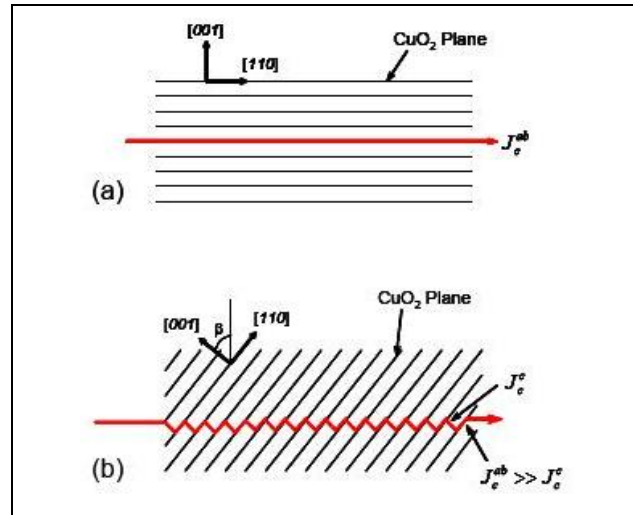


Figure 2.11 Scheme of circulating current in YBCO film (a) c-axis oriented and (b) inclined c-axis oriented regard to the substrate surface (Gonzales, 2005).

2.4 Flux Vortices, Pinning and Critical Currents in Type II Superconductors

HTS conductors in applications will invariably be in the mixed state, between \mathbf{B}_{c1} and \mathbf{B}_{c2} . Thus in order to understand the superconducting properties of such materials it is important to examine the behavior of magnetic field within such materials. Many potential applications for type II superconducting oxide systems would use these materials in such geometry that external fields would penetrate the superconductor with $\mathbf{H} \parallel \mathbf{c}$. Thus, in order to be useful, pinning centers need to be added to this material in such a way that these flux lines can be effectively immobilized. This concerning topics will be discussed in the forthcoming part.

2.4.1 Flux Vortices

Magnetic flux penetrates into a type II superconductor in the form of flux lines or vortices. The vortex, a cylinder with a core of radius ξ contains a region of

suppressed order parameter which decreases to zero at the vortex centre, whilst the local magnetic field rises to a maximum as shown in Figure 2.12.

Abrikosov (1957) predicted by solving the Ginzburg-Landau equations that vortices inside a type II material should form a regular lattice. The arrangement with the lowest free energy turns out to be a triangular lattice, confirmed experimentally by Essmann & Trauble (1967), who observed the flux lines in an electron microscope.

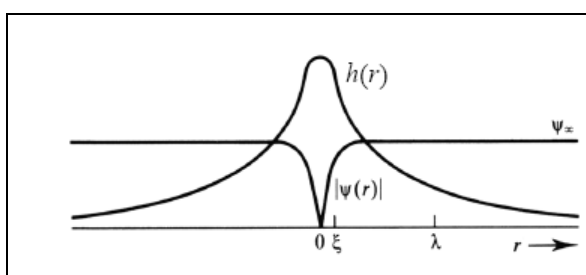


Figure 2.12 Variation of order parameter and local flux density for a single flux vortex (Tinkham, 1996).

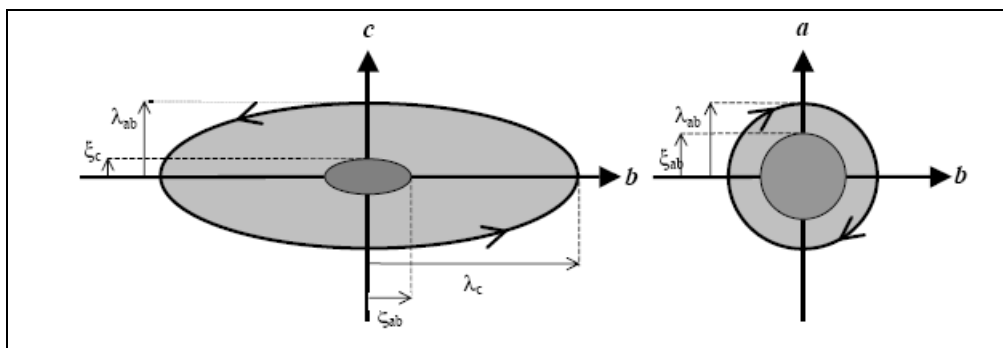


Figure 2.13 Schematic of vortices along the a axis and c axis of a uniaxially anisotropic type II superconductor. The inner shaded region represents the vortex core and the outer perimeter is a line of constant field (Tinkham, 1996).

The large anisotropy of HTS materials causes changes to the structure of flux vortices. The difference in values of the coherence length and penetration depth in the a-b and c directions means that the form of a vortex depends on its direction relative to the crystallographic axes. The vortex core will have radius ξ_{ab} in the a and b directions and radius ξ_c in the c direction, as shown in Figure 2.13. The

approximate ratios of the dimensions in Figure 2.13 for YBCO are $\xi_{ab} \approx 5\xi_c$, $\lambda_c \approx 5\lambda_{ab}$ and $\lambda_{ab} \approx 100\xi_c$ (Zheng et al., 1994).

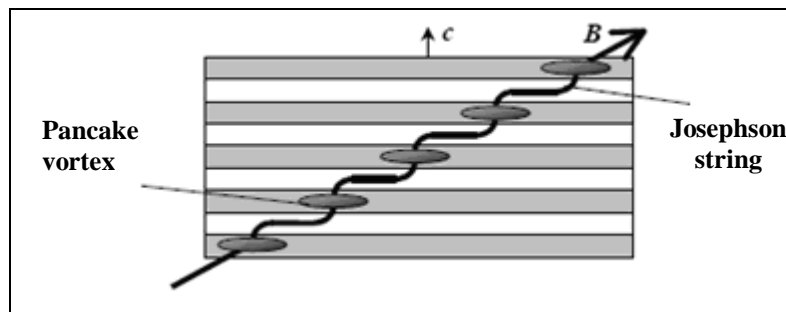


Figure 2.14 A flux vortex in an anisotropic layered superconductor (Hogg, 1999).

In addition to this anisotropy, the layered nature of the high temperature superconductors is also important to the vortex structure. If the coherence length is significantly larger than the interplanar lattice spacing, the homogeneous 3-dimensional description holds. This is the case close to T_c (as ξ diverges at $T=T_c$), but as the temperature is lowered, ξ_c becomes smaller than the plane spacing. In this situation, the copper-oxygen planes are no longer well coupled and the best description of the material is as a stack of superconducting planes. The description of the flux vortices must be modified to take into account the fact that they are localized within the planes. Thus the result is an array of ‘pancakes’ (Clem, 1991), confined to the CuO_2 planes and only weakly coupled to their neighbours. If the magnetic field is in the c direction, the flux pancakes form a simple stack, but for field parallel to the a - b plane, vortices may form between the superconducting planes. These vortices, known as Josephson vortices, have no normal core and thus do not strongly suppress the order parameter in the adjacent superconducting planes. For fields at intermediate angles, the vortex can be described as a combination of pancake vortices in the c -direction (confined within CuO_2 planes) connected by Josephson vortices in the a - b plane as shown in Figure 2.14.

2.4.2 Flux Flow

In the presence of a macroscopic transport current \mathbf{J} , a flux vortex is subject to a Lorentz force per unit length $\mathbf{f}_L = \Phi_0 \mathbf{J} \times \mathbf{n}$, where \mathbf{J} is the current density, \mathbf{n} is a unit vector along the flux line and Φ_0 is the flux quantum. Averaging over a number of vortices gives the Lorentz force density,

$$\mathbf{F}_L = \mathbf{J} \times \mathbf{B} \quad (2.11)$$

This force tends to move flux lines in a direction perpendicular to that of the current flow, inducing an electric field normal to both the movement and the field direction. The value of the electric field is given by;

$$\mathbf{E} = \mathbf{B} \times \mathbf{v} \quad (2.12)$$

where \mathbf{v} is the velocity of the moving flux line.

A simple model of flux flow considers a viscous drag coefficient η , such that the viscous force per unit length on a vortex moving with velocity \mathbf{v} is $-\eta \mathbf{v}$. Then a simple force balance equation is:

$$\Phi_0 \mathbf{J} = -\eta \mathbf{v} \quad (2.13)$$

and the flux flow resistivity, ρ_f , defined by $\mathbf{E} = \rho_f \mathbf{J}$ is given by

$$\rho_f = \frac{\mathbf{E}}{\mathbf{J}} = \frac{\mathbf{B} \Phi_0}{\eta} \quad (2.14)$$

This flux flow resistivity is related approximately to the normal state resistivity, ρ_n , and the upper critical field, \mathbf{B}_{c2} , by

$$\rho_f \approx \rho_n \frac{\mathbf{B}}{\mathbf{B}_{c2}} \quad (2.15)$$

2.4.3 Flux Pinning

In order that dissipation by flux flow does not begin as soon as vortices enter a type II material, it is necessary that there is a force opposing the Lorentz force to ‘pin’ the vortices in place. Such vortex pinning sites are provided by defects in the superconductor which act as energetically favorable sites at which a flux line can reside. Pinning centers may be point defects such as vacancies, line defects such as dislocations or plane defects such as grain boundaries. The presence of such favorable sites for pinning creates an average pinning force for the flux line lattice, F_p , which opposes the Lorentz force. Hence there is a finite critical current density, J_c , as sketched in Figure 2.15.

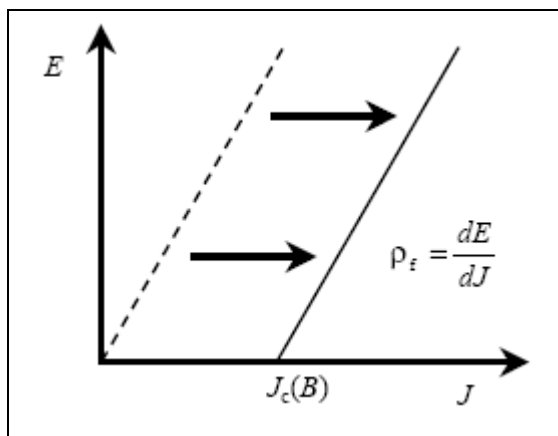


Figure 2.15 Schematic E-J characteristic for linear flux flow (Rutters, 2001).

The degree of pinning varies dramatically amongst high T_c materials. In Bismuth Strontium Calcium Copper Oxide (BSCCO) and Thallium Barium Calcium Copper Oxide (TBCCO), there are very few effective pinning sites and hence critical current values tend to be low. Bulk YBCO is slightly better, but J_c is still limited to around 10^4 - 10^5 Acm^{-2} at 77 K. By far the best pinning is achieved in thin films, where J_c may be increased above 10^6 A cm^{-2} by the incorporation of a high density of defects on a length scale of around 1 nm. An alternative method of increasing the pinning is to introduce artificial pinning sites, which may be achieved by irradiating a sample with fast neutrons.

2.4.4 Flux Creep

Even whilst the average pinning force remains stronger than the Lorentz force and flux flow is prevented, there may still be dissipation caused by thermal fluctuations. One or more flux lines may jump from one pinned configuration to another, overcoming the energy barrier by thermal activation. In the absence of a current, the net movement of flux will be zero, but when a small current flows, it becomes more probable that any fluctuation will cause a flux line to move in the direction of the Lorentz force, and hence there is a net flux motion in that direction. As the current increases, the number of ‘forward’ jumps increases and the number of ‘backward’ jumps decreases, increasing the net movement of flux.

2.4.5 Sources of Pinning

It is possible to divide pinning centers into two groups depending on whether they arise from interactions with the core (ξ dependent) or the screening currents (λ dependent). In both cases the flux line lattice (FLL) is distorted so as to accommodate pinning sites, in order to minimize the overall free energy of the system. Pinning where the order parameter falls to zero over defects of a size similar to ξ is termed core pinning. An example of this would be a cylinder defect of radius ξ . Magnetic pinning arises from interactions between the screening currents and defects with lengths of the order of λ . An example of magnetic pinning would be that due to variations in the thickness of a thin film. In HTS materials, except for $\mathbf{B}_a \sim \mathbf{B}_{c1}$, the screening currents and associated fields overlap leading to a relatively uniform local magnetic field compared to the isolated vortex case. Magnetic pinning is therefore less important than core pinning. In oxide superconductors it is possible to produce high quality single crystals where the pinning is weak compared to that found in thin films. In such crystals the pinning is predominately due to randomly distributed point defects. Thin film samples, as a consequence of the growth technique, have a high density of strong pinning centers and thus much larger critical current values. There are several types of strong pinning in thin films such as anti-phase boundaries, twin planes, dislocations and surface features. In the case of the

HTS material YBCO, Dam et al. (1999) have recently provided convincing evidence that dislocations are the dominant form of pinning centers in YBCO thin films. In vicinal YBCO films containing a high density of anti-phase boundaries an enhancement of J_c of almost an order of magnitude is observed (Jooss, et al. 1999; Jooss, Warthmann. & Kronmuller. 2000).

2.5 YBCO Thin Films

The anisotropic and layered nature of YBCO coupled with its short coherence length indicates that, to make these materials useful for applications, thin films consisting of a well-aligned network of grains are necessary. Presently, two general categories of deposition methods for YBCO thin films exist as physical and chemical methods. Physical deposition methods (Pulsed Laser Deposition (PLD), Ion Beam Assisted Deposition (IBAD), sputtering, and evaporation) involve the kinetic transfer of material (Y, Ba, Cu and O atoms) to a crystallographic template surface conducive to the growth of the desired YBCO orientation. These methods thus represent a "building block" approach to YBCO growth where YBCO nucleates at the substrate and grows in the direction of the film normal.

The major advantage of the physical deposition process is that, due to the building block nature of their growth, control over the process is maintained to a large extent throughout the deposition procedure. This makes this technique highly useful in a research environment where control over external variables is critical. The downside to this process is that this unit-cell by unit-cell approach tends to be slow from the perspective of mass production. Furthermore, it requires the use of a high vacuum chamber that represents a large capital investment as well as high operating and maintenance costs. Thus, from the perspective of the industry, this approach is undesirable. In contrast to physical deposition methods, the chemical deposition route distinguishes itself as having the potential for reducing overall costs in the industrial process. Chemical deposition methods take after the sol-gel process in which a precursor solution containing the desired atomic species (in this case, Y, Ba, and Cu organic bonds) is coated over a crystallographic template. Unlike physical

deposition processes, the energy for nucleation during the coating process is not met but rather comes from a subsequent heat treatment under a flowing gas environment. The chemical potential of the system is controlled by the gas transport and the kinetic energy for nucleation is supplied from the heat. This deposition technique therefore exhibits a much more three dimensional growth compared to physical processes in that the desired crystallographic phase may nucleate and grow as layers or islands. Since this type of processes involve less specialized equipment, it represents a lower capital investment and operating costs for industry. Also, this process tends to be faster than physical deposition methods for the same film volume. It thus has a large potential for mass production through the use of a batch coating and subsequent heat treatment process. For industry, then, the most critical issue with this process is knowledge of and control over the processing parameters and their subsequent effect on film quality. Chemical deposition methods especially Chemical Solution Deposition Technique including Trifluoroacetic Acid Metal Organic Deposition (TFA-MOD) will be in detail explained in Chapter 3.

2.5.1 Artificial Pinning Centers in YBCO Thin Films

Due to the fact that effective pinning centers require spatial dimensions on the order of the YBCO coherence length, controlling the size and distribution of these defects is a challenge well suited for materials science. Through careful materials processing, Artificial Pinning Centers (APCs) can be introduced in a controlled manner, subsequently influencing the macroscopic properties of YBCO (Roas, Schultz, & Endres, 1988). The introduction of APCs to thin films of YBCO is the topic of this part and a brief history of work on this topic will be summarized.

With the fabrication of YBCO thin films by PLD method, the effectiveness of APCs could be investigated in a controlled manner (Inam et al., 1988). In one of the first experiments, the YBCO crystal structure was bombarded with ion radiation, forming significant directional pinning-active defects (Roas, Hensel, Endres, Schultz, & Saemann-Ischenko, 1989). Work on using secondary phases for APCs accelerated in 2004 with a report that multilayers of YBCO and YBa_2CuO_5 result in a high

density of pinning-active defects in thin films (Haugan, Barnes, Wheeler, Meisenkothen, & Sumption, 2004). Multilayers are certainly not the only way to introduce pinning centers into YBCO thin films. Rare-earth substitutions can also significantly enhance J_c (Cai, Holzapfel, Hanisch, Fernandez, & Schultz, 2004). This method works by substituting Y with another rare-earth element such as Gd or Sm. The change in ion radii introduces strain effects and dislocations that act as effective pinning centers. However, controlling the size and organization of such defects is quite challenging.

A highly effective method for countering this is through the controlled introduction of a perovskite secondary phase such as BZO into the YBCO matrix. This phase can be introduced as nano-sized particles that can be heteroepitaxially incorporated into the surrounding YBCO matrix during the PLD process, producing strain effects that act as effective pinning centers (MacManus-Driscoll, Foltyn, Jia, Wang, Serquis, & Civale, 2004). To date, an enormous number of investigations have looked into the possibility of enhancing flux pinning through the introduction of similar secondary phases as $BaIrO_3$, $BaZrO_3$, $BaTiO_3$, $BaSnO_3$ and $BaHfO_3$ (Mele et al., 2008). Other perovskites such as the so-called “2411” phase $Y_2Ba_4CuMO_y$ ($M = Nb, Zr$) (Yamada et al., 2008; Reich, Thersleff, Hühne, Iida, Schultz, & Holzapfel, 2009) or $BaNb_2O_6$ (Yamada et al., 2007) can also be introduced and show enhanced pinning effects. Finally, rare earth tantalate pyrochlore nanoparticles were also shown to have a significant effect on pinning (Harrington et al., 2009).

APCs introduced through physical deposition methods like PLD are easy to study and fabricate but physical deposition processes are not necessarily the most ideal for industrial development as discussed before. Moreover, the defect structures formed through the addition of APCs introduced in this manner show highly anisotropic properties, necessitating complex deposition techniques to produce pinning-active defects oriented in multiple directions (Maiorow et al., 2009). For these reasons, the introduction of APCs into films deposited by a chemical process known first successful attempt was reported by Gutierrez et al. (Gutierrez et al., 2007) for BZO particles. Surprisingly, the introduction of these particles by chemical methods leads

to a drastic reduction in anisotropy of the YBCO superconductor. This gave these films an exceptionally high pinning force and J_c values. Whilst BZO is an effective pinning center, any perovskite crystal structure with a lattice parameter equal to approximately 1/3 of the c-axis length of YBCO should also work.

2.6 Applications of Superconductors

A number of commercial superconductivity applications were available such as magnets, radiation detectors and magnetometers. Since the discovery of the phenomenon, innumerable ideas have been proposed for using superconductivity in all types of devices. Some have actually been built for research purposes and prototypes of others have been constructed. Most of these have not come to commercial fruition owing to technological or economic factors. The need to cool the devices to liquid helium temperatures has made most of these applications too expensive in practice. One of the exciting aspects of the availability of liquid nitrogen temperature superconductors is the possibility that some of these proposals may now become feasible (Owens & Poole, 1996).

The recent achievement of critical currents exceeding $1.000.000 \text{ Amps/cm}^2$ at 77 K in YBCO deposited on suitable textured substrate has stimulated interest in the potential application of coated conductors in high temperatures and high magnetic fields. Superconducting films have opened up new possibilities for passive and active microwave and optical components, namely, filters, delay lines, micro strip patch antennas, power combining circuits, solid-state devices, kinetic induction phase shifters, MRI sensors, SQUID devices, A/D converters, optical detectors, generators, motors, and especially in wire industry. Nonetheless, the technical difficulties originated from the grain boundaries and commercialization consideration of the scale-up and high fabrication cost have been challenging the research and development of HTSs (Xu, 2003).

Magnetic levitation is an application where superconductors perform extremely well. Transport vehicles such as trains can be made to float on superconducting

magnets, virtually eliminating friction between the train and its tracks. Not only would conventional electromagnets waste much of the electrical energy as heat, they would have to be physically much larger than superconducting magnets.

Superconducting Quantum Interference Devices (SQUIDs) are capable of sensing a change in a magnetic field over a billion times weaker than the force that moves the needle on a compass. With this technology, the body can be probed to certain depths without the need for the strong magnetic fields associated with MRI's.

Electric generators made with superconducting wire are far more efficient than conventional generators wound with copper wire. In fact, their efficiency is above 99% and their size about half that of conventional generators. These facts make them very lucrative ventures for power utilities. Other commercial power projects in the works that employ superconductor technology include energy storage to enhance power stability (Hott, 2003).

As the demand for electrical power is increasing, one of the challenges for the utility industry is to find new ways to transport large amount of power from the generation plant to consumers. The market in electrical transmission and distribution is large especially in urban areas where the demand of electricity is increasing while there is limited clearance for overhead cables. Thus, using underground HTS cables capable of carrying three to five times more power than copper cables of the same size, and thus using existing rights of way is an attractive solution. Furthermore, significant portions of the existing cables are aging and need replacement in the near future. Not only that HTS cables can transmit electricity with minimal resistive losses, in addition, the liquid nitrogen used to cool underground HTS cables is less expensive and presents less environmental risk than the dielectric oil used in copper cables (Hott, 2003).

Another application of superconductors in electrical transmission is the fault current limiter (FCL) that uses the superconducting-normal (S-N) transition of a superconductor to reduce the fault current in an electric circuit. In the event of a fault

current, the J_c of the superconductor is exceeded whereby the material turns into its normal state that limits the large fault current. The FCL is capable of reducing a fault current nearly instantaneously and is highly sought since the increasing power consumption and demand make it useable where the short-circuit capacity of power system would exceed the capacity of a conventional circuit breaker. HTS materials connected in series are very effective in controlling rising fault currents within milliseconds since the SN transition can occur in less than 1 ms (Hott, 2003).

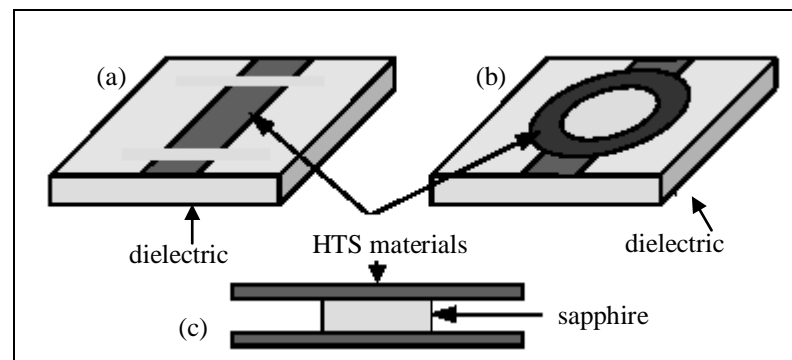


Figure 2.16 HTS resonator structure layout, (a) Micro strip, (b) Ring resonator and (c) Parallel plate shunted by a dielectric resonator (Xu, 2003).

A newly designed RF element shown in Figure 2.16 is an electronic application of HTS film. Low surface resistance, R_s , is a key property of conductors used in RF device applications. For a normal conductor such as copper, the surface resistance is on the order of 0.01 at the frequency of 2 GHz. The surface resistance is many orders of magnitude below this at the same frequency range in a well-textured YBCO, making this HTS material an attractive candidate for RF components (Xu, 2003).

CHAPTER THREE

CHEMICAL SOLUTION DEPOSITION

Epitaxial thin films can be grown on single-crystal substrates with a variety of different methods. These are pulsed laser deposition (PLD), ion beam assisted deposition (IBAD), physical vapour deposition (PVD), electron beam evaporation, magnetron sputtering, liquid phase epitaxy, chemical vapor deposition (CVD) and chemical solution deposition (CSD). The current development of solution-deposition methods appears to have promise to compete with vapor phase methods for superconductor electrical properties, with potential advantages for large scale deposition and low cost. This chapter reviews chemical solution deposition, in which a solution is used to deposit a layer of precursor molecules that decompose to low-density, polycrystalline films during heat treatment. Solution preparation, coating, nucleation and growth properties are discussed in detailed to better understand the method.

3.1 Deposition Methods for Superconducting Thin Films

Several techniques with a characteristic morphology and associated physical properties exist to grown superconducting films. These growth techniques could be classified into two categories as physical and chemical methods:

3.1.1 Physical Deposition Methods

Pulse laser deposition (PLD), sputtering, molecular beam epitaxy and BaF_2 processes are examples of physical methods. Generally, all these techniques require expensive high-vacuum systems to grow superconducting thin films. Another disadvantage is the relatively slow growth rate of thin films. Therefore, long growth times are required to get films with high current carrying capacity.

3.1.2 Chemical Deposition Methods

Chemical solution deposition (CSD), metal organic chemical vapor deposition (MOCVD) and liquid phase epitaxy are examples of chemical methods. These methods have high potential to scale-up and still under development. The most important advantage of these methods is that they do not require expensive high-vacuum systems to grow superconducting thin films. Of these techniques; solution based deposition routes for complex oxides have been developed over the past decades due to their ease of incorporating multiple elements, good control of local stoichiometry and feasibility for large area deposition.

Chemical solution deposition technique has many advantages as;

- High purity,
- No need of vacuum technology,
- High degree of homogeneity, because reagents are mixed at molecular level,
- Porosity control by using appropriate CSD system and heat treatment,
- Possibility to obtain fully-dense crystalline ceramics which can not be prepared by conventional powder processing and
- The capability of obtaining fully-dense amorphous solids at temperatures lower by hundreds of degrees than those required for conventional compaction/densification or for melting.

A range of requirements must be fulfilled by the solution chemistry, substrates, and processing conditions for successful implementation of the CSD technique. These include:

- Sufficient solubility of the precursors in the solvent to form a stable coating solution,
- Synthesis of precursors that decompose or may be pyrolysed without undesirable residues during thermal processing; i.e., all of the elements except

the cations (and oxygen ions) must be released into the gas phase during thermal treatment for perovskite formation,

- No macroscopic phase separation of precursor components during drying or pyrolysis; i.e., crystallization of the individual components upon solvent evaporation should be avoided and homogeneity at an ‘atomic’ level should be retained,
- Acceptable wetting of the substrate,
- Solution rheology adjusted to the deposition approach and the deposition parameters employed to avoid thickness variations,
- No crack formation or compositional nonuniformities during pyrolysis or crystallization,
- Minimal interdiffusion of film and substrate constituents; minimal degradation of substrate properties during film processing,
- Sufficient long-term stability of the solution to avoid non-reproducible film properties those are dependent on solution aging.

If these requirements are fulfilled and if processing conditions are optimized, the CSD technique represents a rapid and cost-effective method for synthesizing high-quality electronic oxide thin films.

Depending on the procedures utilized during coating solution preparation, the gelation behavior of the deposited film, and the reactions that take place during thermal annealing, the various chemical routes utilized as chemical solution deposition for electronic oxide film fabrication can be grouped into three principal categories: aqueous-based deposition, sol-gel chemistry approach and metal-organic decomposition. Certainly, these categories are too imprecise to classify all conceivable CSD routes exactly, and in many cases, the route under study comprises aspects of more than one of these categories. However, to understand the underlying chemistry of a particular CSD route, it is beneficial to discuss the various approaches that have been utilized from this standpoint (Schwartz, Schneller & Waser, 2004).

3.1.2.1 Aqueous Deposition

Aqueous deposition of materials may be conducted by hydrothermal synthesis or evaporation of the solvent from dissolved salts, followed by appropriate processing of the residual dissolved material. While the latter may be especially effective for depositing salts, it has not been widely used for processing of superconductors, since aqueous solubility of the elements of interest are low, and superconducting oxide stoichiometry control within a few percentages is critical.

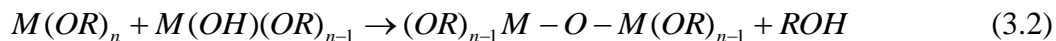
3.1.2.2 Sol-gel Process

Sol-gel process commonly starts from metal alkoxides undergoing hydrolysis and condensation reactions, leading to a three-dimensional gel network. That is generally designed to enable metal-oxide-metal chain formation through use of polycondensation reactions. Precursors for chemical sol-gel approaches generally are metal salts or metal alkoxides dissolved in an alcohol-based solvent system. The general principles of sol-gel processes are formation of a stable chemical dispersion or sol, and subsequent reaction of the sol to form continuous gel network through hydrolysis and polycondensation reactions as described in Equations 3.1 and 3.2. In these equations R represents an organic group such as an alkyl or a salt group and ROH could then represent a free alcohol or other liberated organic group. Through progression of the polycondensation reactions, a further more cross-linked M-O-M metal oxide gel network is formed, which possesses a high degree of local chemical homogeneity and will display a decreased change in volume on solvent removal compared to MOD and aqueous CSD processes. This change in volume is particularly important for minimizing film tensile stresses.

Hydrolysis reaction of a metal organic $M(OR)_n$



Polycondensation reaction of a metal organic $M(OR)_n$



Sol-gel deposition of thin films holds great potential as a fast and efficient method of producing large-scale, biaxially-textured superconducting films at a lower cost than physical and chemical vapor deposition techniques (Schwartz, 1997).

3.1.2.3 Metalorganic Decomposition

Metal organic decomposition (MOD) is generally based on metalorganic precursors insensitive to hydrolysis, such as carboxylates (e.g. acetates, ethyl hexanoates) or b-diketonates (e.g. pentanedionates), that are decomposed during pyrolysis after evaporating the solvents of the as-deposited layer. This approach is often straightforward and robust, as the chemistry in solution is very stable. On decomposition of metalorganic deposit, a large volume change occurs due to burnout or pyrolysis of the organic materials into CO₂ and H₂O, so this step may need to be closely controlled to avoid extremely exothermic process conditions, or formation of large biaxial tensile stresses in the film that could lead to cracking. One example of MOD is the well established trifluoroacetate process, where metal acetates dissolved in distilled water are converted into metal trifluoroacetates by reacting with trifluoroacetic acid (Pinol & Castano, 2006). This alternative solution process based on trifluoroacetic acid was first developed by Gupta et al. called TFA-MOD process and since then, this method is routinely used for high quality YBCO thin film production. This method has many advantages as a precise control of the metal cations, a broad flexibility to coat large area surfaces and does not require any expensive vacuum apparatus at any time during the whole process. Thus, TFA-MOD is regarded as one of the most suitable candidates for fabricating YBCO long tapes for many high power applications at low cost.

3.2 Steps of Chemical Solution Deposition Method

The chemical solution deposition method for the preparation of superconducting thin films can be divided into three main stages:

1. The precursor solution synthesis from precursors according to the designated layer composition and the chemical process to be used.
2. The coating procedure to obtain homogeneous precursor layers of controlled thickness.
3. The thermal treatment of the precursor layer converting the as-deposited layer into a crystallized final oxide layer via an amorphous state as summarized in Figure 3.1. The overall thermal treatment is composed of pyrolysis, nucleation and crystal growth processes.

1. Precursor solution synthesis

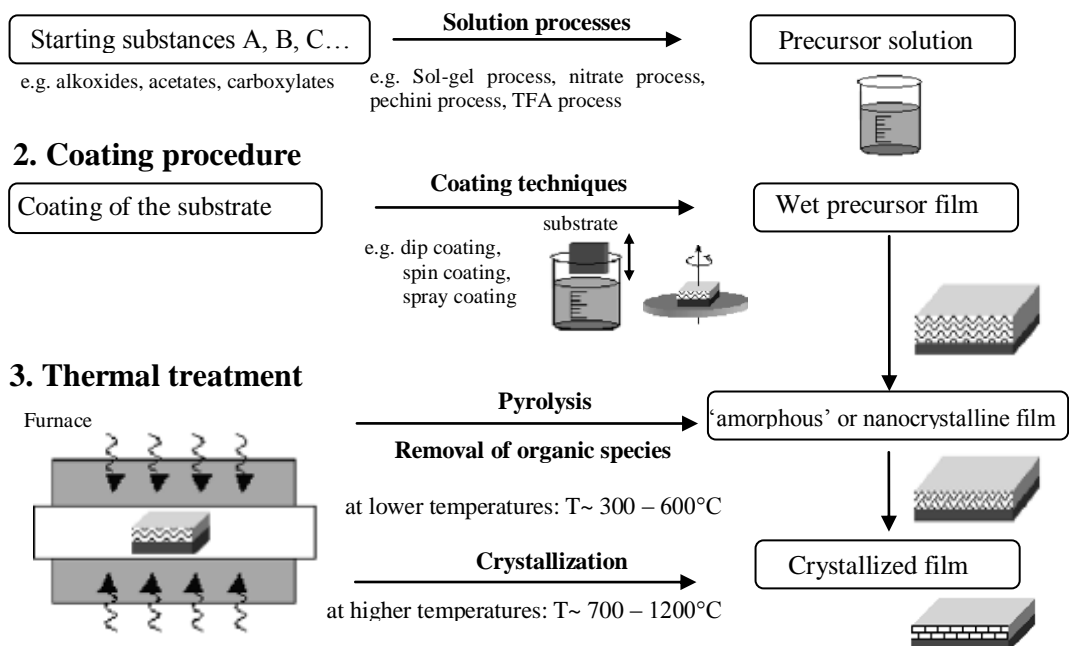


Figure 3.1 Overview of the chemical solution deposition process (Knoth et al., 2006).

Although they are all separate processes, each step is dependent on the preceding steps in order to successfully fabricate a high- J_c superconducting film. The three major process steps and their adaptation to low cost manufacturing are summarized in the following sections.

3.2.1 The Precursor Solution Synthesis

The general principle involved in the solution deposition of perovskite films is to prepare a ‘homogeneous’ solution of the necessary cation species that may later be applied to a substrate. The requirements of appropriate solubility combined with pyrolysis that leaves solely the cations (and oxygen) as a residue, represent an especially significant limitation regarding the choice of precursors. Usually, metal-organic compounds are suitable, due to the fact that their solubility in polar or non-polar solvents can be tuned by modifying the organic part of the molecule, and because the organic part pyrolyzes in oxidizing ambient atmosphere without residue.

The most commonly used classes of precursor compounds are carboxylates, alkoxides, β -diketonates, etc. Metal carboxylates are the most common type of precursor which is frequently used for MOD. They are salts of carboxylic acids, R-COOH, where R represents an alkyl group such as methyl, CH₃ (acetic acid; salt: acetate), ethyl, C₂H₅ (propionic acid; salt: propionate), etc. Carboxylates can normally be dissolved in their own (parent) carboxylic acids, and for short alkyl chain salts, some solubility of the carboxylate (i.e., acetate, R = CH₃) in water and other highly polar solvents is typically observed due to the polar nature of the salt. Regarding the water stability of short chain carboxylates, it should be noted, that solubility typically implies that these materials are not stable in water. However in case of CSD processing stability against water means that it does not lead to a gel formation upon addition of water in contrast to the metal alkoxides.

The coating solution is prepared by mixing, and possibly reacting the individual precursors or precursor solutions. The chemical interactions that occur between the starting reagents during solution synthesis depend on the reactivity of the compounds and the solution preparation conditions, such as reflux temperature.

Two main routes have been used for the solution preparation of high quality YBCO thin films as fluorinated and non-fluorinated. Non-fluorinated films in many cases form intermediate barium carbonate phases due to decomposition of

metal-organics, which liberates CO_2 and water as byproducts. Fluorinated routes have been shown by using trifluoroacetic acid to avoid formation of such carbonates by forming a more thermodynamically stable BaF_2 phase instead of BaCO_3 , and later decomposing this BaF_2 phase through reaction with water vapor. The presence of barium carbonate during the processing of metal-organic derived YBCO has been reported by many authors as a potential hindrance to high quality films, as long anneal times and temperatures are often required to decompose this phase. Thermodynamic calculations of BaCO_3 stability in the YBCO system suggest stability of the carbonate phase (positive ΔG) until very high temperatures, and BaCO_3 has been observed experimentally to decompose gradually up to $1000\text{ }^\circ\text{C}$.

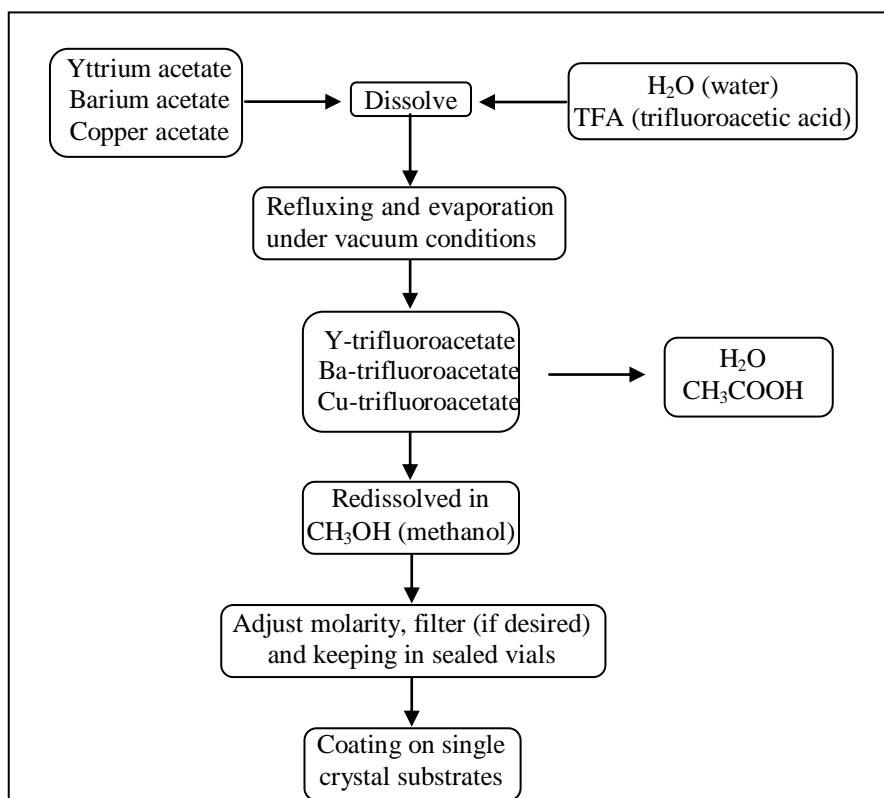


Figure 3.2 Process for preparing coating solution in TFA-MOD. Metal trifluoroacetates are synthesized with metal acetates and trifluoroacetic acid in water (Araki, & Hirabayashi, 2003).

The earliest research using fluorinated sol-gel precursors was reported by Gupta et al. (1988), who showed for the first time the implementation of trifluoroacetic acid as

both a fluorine source, and as a solution stabilizer. In the synthesis of YBCO precursor solutions, three issues are often difficult: solubility of copper and barium precursors, solution stability, and avoiding carbonate degradation of oriented films. Trifluoroacetic acid (CF₃COOH) is a strong chelating or stabilizing agent, which aids in the solubility and stability of dissolved metal salts for these precursor solutions.

Generally, the TFA process uses a mixture of metal (Y, Ba and Cu) acetates with a stoichiometric amount of trifluoroacetic acid in an aqueous solution as a precursor. Related chemical reaction is described in Equation 3.3:



The precursor solution is submitted to a reflux in order to improve homogeneity of the solution. The resulting viscous solution is then redissolved in methanol to make a solution of low viscosity and hence suitable for deposition on single crystal or metallic substrates. The steps of this process are briefly shown in Figure 3.2.

3.2.2 Precursor Solution Coating

Deposition of the precursor solution onto single crystal substrates can be carried out by a variety of coating techniques as spin, dip, spray, slot-die coating and ink-jet printing as illustrated in Figure 3.3. For all coating methods, the precursor layer thickness is governed by solution properties like molarity and viscosity as well as by the deposition speed and coating time. Furthermore, the thickness is influenced by factors such as surface tension and gravitational forces. Depending on the precursor solution and deposition method, the most common single layer thicknesses achieved are between 50 and 300 nm. A higher thickness can be realized by multiple coatings.

Among the continuous coating, dip coating seems to be a simple and suitable method for coated conductors. The general steps of dip coating include immersion of the substrate into the dip coating solution, start-up, where withdrawal of the substrate from the solution begins, film deposition, solvent evaporation and continued

drainage as the substrate is completely removed from the liquid bath. The film thickness formed in dip coating is mainly governed by the viscous drag, gravitational forces and surface tension. The final thickness of the dip-coated superconducting film depends on the concentration of the coating solution and the substrate withdrawal speed during the coating process. For coating long length conductors or large area films at industrial scale, dip coating technique is very suitable to minimize the use of solution and both faces can be coated simultaneously (Araki et al., 2003).

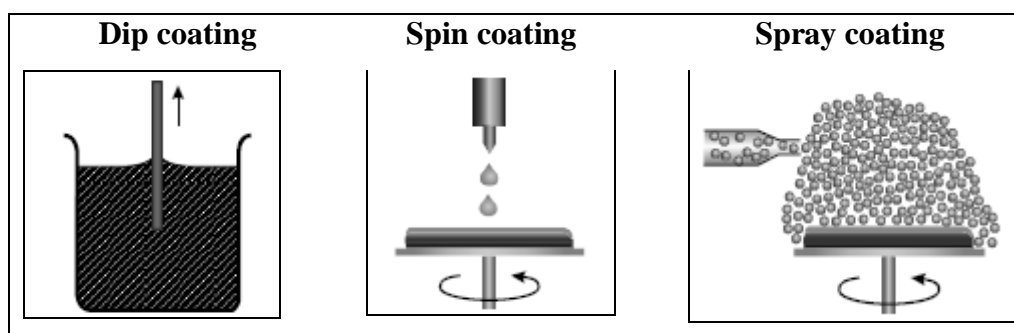


Figure 3.3 Schematic illustrations of the commonly used coating techniques (Schwartz, 2004).

In spin coating process, the substrate is held in place on the spinner by applying a vacuum to the back side of the wafer through a chuck that is attached at the end of the spinner motor shaft. The wafer is typically flooded with solution during a “static dispense” using a syringe. The wafer is then accelerated rapidly to 1000-6000 rpm and the spinning time can vary from seconds to few minutes. Spin coating is a very convenient technique for the laboratory scale production of TFA-MOD superconducting films because a very small volume of solution is used and an accurate control of the film thickness can be achieved by controlling the precursor viscosity, spinning rate and time. Higher speed and longer spin time results in thinner film, but at very high spin speed and long spin time, the film thickness becomes constant.

In spray coating process, the substrate surface is completely sprayed with fine disperse solutions. It is a completely industrial system and substrate rate and solution characteristics are strictly correlated with the deposited film thickness. There are

different methods about how to spray the precursor solution in fine dispersed particles. One very promising seems to be an ultrasound that is able to produce a very homogeneous dispersion of the precursor solution. The spray coating is not useful for all kinds of precursor solutions because the interactions between micro drops after deposition have to be strong enough to obtain a homogeneous film on the substrate.

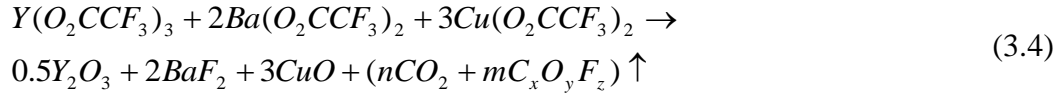
With respect to cost-efficient production, slot-die coating and ink-jet printing techniques as well as spraying may be of further interest due to the nearly 100% utilization of the precursor solution.

3.2.3 Pyrolysis

The thermal treatment applied to transform the as-deposited precursor layer into the desired crystalline phase can be subdivided into two stages. At lower temperatures, typically between 300 °C and 600 °C, the as-deposited precursor layer is pyrolysed, leading to a removal of the organic species associated with a high-volume shrinkage of the layer. Due to this shrinkage, stress and microcracks can be easily introduced, depending on the chemical process chosen. The result is an amorphous or nanocrystalline metastable and porous layer as an intermediate state. The formation of this intermediate state is dependent on the chemical route used. Its transformation to the final oxide is controlled by the chemical composition of this oxide, as different cations have different tendencies to form stable intermediate compounds such as carbonates. During annealing at higher temperatures between 600 °C and 1200 °C, the crystallization of the amorphous intermediate layer takes place based on the thermodynamic principles valid for nucleation and growth processes well known for classical melts.

Generally, precursor pyrolysis involves the thermal decomposition of the metal organic salts and removal of the organic constituents of the precursor, leaving behind a mixture of copper oxide, yttrium oxide and barium fluoride. Even though the

complete decomposition reaction is still not well understood, it is possible to summarize it as follows:



The process is generally carried out in a humid and oxidizing atmosphere at temperatures below 400 °C. Water vapour is added to the system to suppress sublimation of $Cu(O_2CCF_3)_2$ from the film, which means water molecules seem to stabilize $Cu(TFA)_2$. The water humidified gas is obtained by passing oxygen through deionized water containing flasks accordingly prior to enter of the furnace.

The thermal decomposition of TFA precursor films results in a reduction of film thickness in the order of 50% and is accompanied by an increase of stress within the film. The standard TFA-based precursors are very susceptible to cracking at decomposition temperatures and in order to reduce cracking in the precursor film very slow heating rates are required during pyrolysis. By optimizing the heating rate conditions it is possible to reduce the time required for pyrolysis process.

3.2.4 Nucleation and Crystal Growth

The CuO , BaF_2 and Y_2O_3 nanocrystallites that result from decomposition of the metal trifluoroacetates subsequently have to be converted to the $YBa_2Cu_3O_{7-x}$ phase by annealing in humid nitrogen/oxygen gas mixtures at temperatures ~750-800 °C. The reaction process occurs according to the following Equation 3.5:



The conversion of the decomposed precursor film to the YBCO phase is illustrated in Figure 3.3. The initial step is the reaction of BaF_2 in the precursor film with H_2O , which requires the transport of H_2O vapour into the film and removal of the resulting HF product. As the BaF_2 reacts, the YBCO phase nucleates at the substrate interface and continues to grow through the film thickness as illustrated.

Precise control of the reaction rate is required to promote the epitaxial nucleation of YBCO on the substrate surface and subsequent growth of the highly textured YBCO through the thickness of the film. Depending on the experimental conditions such as total pressure, $P(\text{H}_2\text{O})$, $P(\text{O}_2)$, flow rate (V_g) and temperature; the growth rate, R , can be varied in a very extend range. The YBCO continues to grow through the thickness of the precursor as the film is held at the growth temperature. Finally, the film is slowly cooled down into a dry oxidizing atmosphere to carry out the film oxygenation ad thus transform the insulating tetragonal $\text{YBa}_2\text{Cu}_3\text{O}_{6.5}$ to the superconducting orthorhombic $\text{YBa}_2\text{Cu}_3\text{O}_{7-x}$ phase.

A theoretical analysis of YBCO growth proposed by Honjo et al. to estimate the growth rate of the YBCO phase in order to optimize the annealing time under various conditions was used to study the relation between the gas flow vector of water pressure and the HF gas (Honja et al., 2003). Figure 3.4 shows the image of their model. They consider a one dimensional analysis for the mass transfer of H_2O and HF gases. It can be imagined that the precursor film is surrounded by a stagnant gas boundary layer through which H_2O diffuses and arrives at the precursor surface (H_2O mass transfer through porous layer). They assume that the conversion reaction only occurs at the YBCO growing interface and the produced HF diffuses back out through the precursor film and gas boundary layer to the main gas stream (HF mass transfer through a gas). They have an expression for the local rate of conversion from H_2O to HF, given by:

$$R = K \frac{\sqrt{V_g} \sqrt{P(\text{H}_2\text{O})}}{P_{\text{Total}}^{1/6}} \exp[-(a/T)] \quad (3.6)$$

where K is a constant, T is the temperature, V_g is the gas flow rate, P_{Total} is the total pressure and $P(\text{H}_2\text{O})$ is the water pressure.

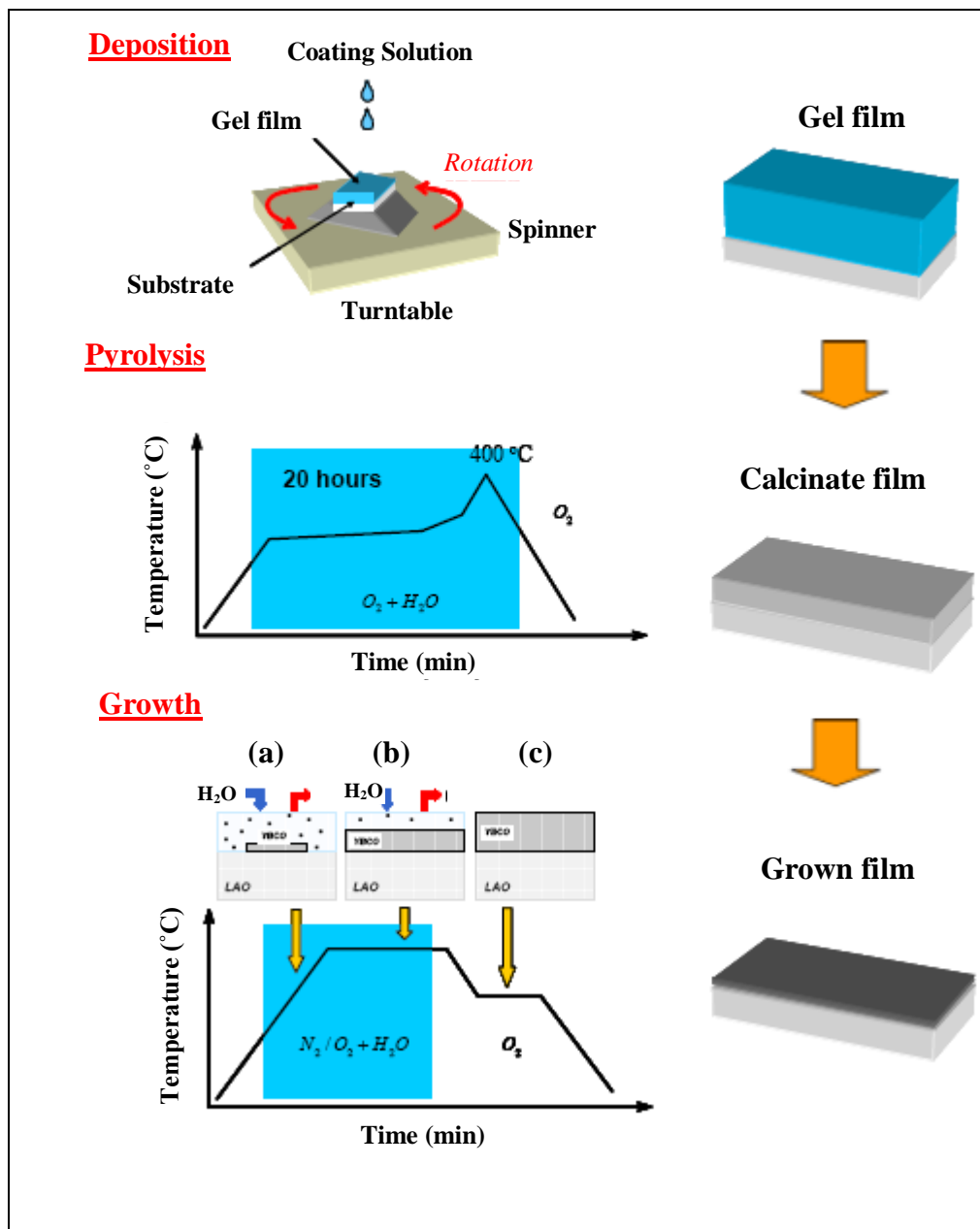


Figure 3.3 Schematic illustration of metalorganic deposition using trifluoroacetates for fabricating YBCO superconductors. Coating solution is deposited to give a gel film on the substrate by spin coating. The gel is pyrolysed for the decomposition of trifluoroacetate-based precursor films and then become a precursor film. The precursor is converted to YBCO superconductor. Illustration of the (a) nucleation, (b) growth and (c) oxygenation of the YBCO phase from trifluoroacetates precursor film as a function of processing temperature and atmospheres. All these processes may be achieved in ambient pressure (Gonzales, 2005).

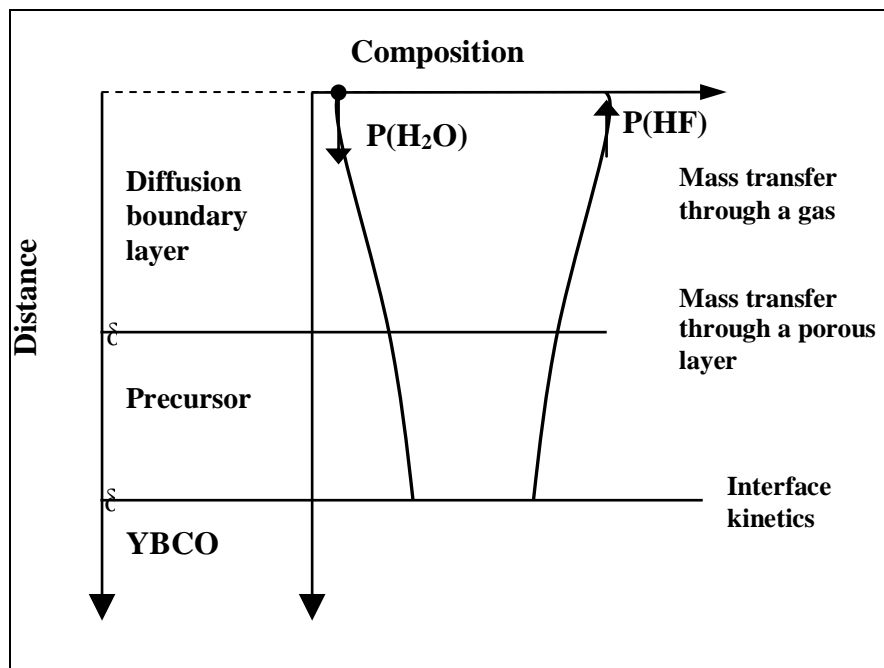


Figure 3.4 YBCO growth model, where δ_p is the effective precursor film thickness, δ_g is the gas boundary layer thickness. H_2O gas diffuses and arrives at the precursor surface (Honjo et al., 2003).

Two main kinetic processes of phase transformations were described by Gibbs. The first one is nucleation and growth which involves large change in composition inside a very small volume extent in a preliminary stage. The second one is spinodal decomposition which involves composition waves with small change in composition inside a large volume extent. The formation of solid particles from a precursor solution essentially involves the nucleation and growth process. Their total free energy ΔG_r to form a spherical particle with a radius r comprises a contribution G_s to create the surface of the particle and of a contribution ΔG_{int} which is due to the phase transformation inside the particle:

$$\Delta G_r = G_s + \Delta G_{int} \quad (3.7)$$

The contribution which is due to the surface is a positive one and it depends on the surface energy γ of the particles.

$$\Delta G_s = 4\pi r^2 \gamma > 0 \quad (3.8)$$

The contribution due to phase transformation inside a particle is negative and it depends on the difference ΔG_v between the free energies per unit volume of the new β phase and of the old one α .

$$\Delta G_{\text{int}} = 4/3 \pi r^3 (G_{\beta} - G_{\alpha}) = 4/3 \pi r^3 \Delta G_v < 0 \quad (3.9)$$

The change in the free energy ΔG_r to form a particle depends on r as illustrated in Figure 3.5. At the beginning when r is very small, the surface contribution dominates, so that the free energy change is $\Delta G_r > 0$. Therefore, this is not a stage which is thermodynamically favorable. However, after a critical value $r = r_c$ is passed, the internal contribution starts to dominate so that the evolution becomes thermodynamically favorable. The value of r_c for which ΔG_r reaches a maximum is given by;

$$\delta \Delta G_r / \delta r = 0.$$

That is to say $r_c = -2\gamma / \Delta G_v$. The final ΔG_v corresponds to the transformation of;

Initial solution \rightarrow Final solution + particles

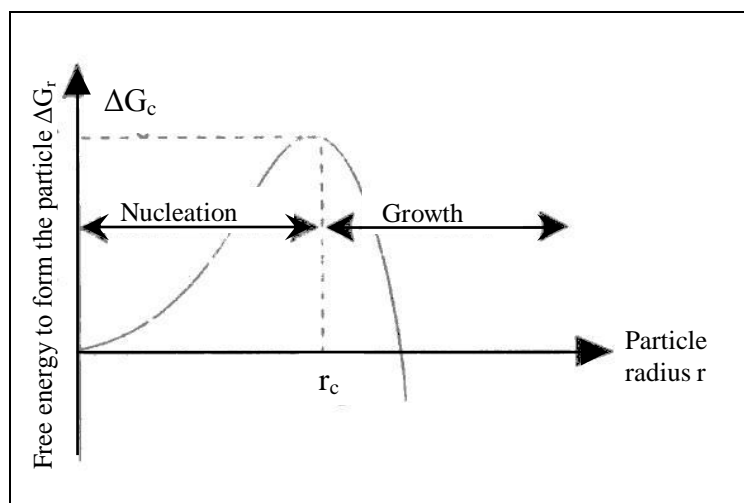


Figure 3.5 Nucleation and growth of a spherical particle (Pierre, 1998).

When a sol or solution transforms to a gel, gelation occurs. It consists of establishing links between the sol particles or the solution molecules so as to form 3-dimensional solid network. Gelation occurs when the extent of polymerization reactions ξ reaches a critical value ξ_c . This precise critical stage, when for the first time a polymer of infinite size is formed by comparison with the molecular scale, defines the gel point. In a practical manner, at this point the product resulting from polymeric condensations transforms suddenly from a viscous liquid to a material with elastic properties.

Drying is irreversible transformation of the gel which is composed of a solid network and liquid matrix. The capillary mechanism explains well the reproducible adsorption hysteresis curves of water in silica gels. This mechanism can be summarized as follows:

- Evaporation creates a liquid vapor meniscus at the exit of pores in the gel.
- This induces a hydrostatic tension in the liquid, which is balanced by an axial compression on the solid.
- The latter compression makes the gel shrink.
- As a result of shrinkage, more liquid is fed to the menisci at the exit of the gel pores, where it is evaporated and so on.

Two approaches are commonly used to complete the transformation of the as-deposited film into the crystalline ceramic: the *one-step* and the *two-step* processes.

In the *one-step* process, the film is heated directly to the crystallization temperature, which results in both organic removal and crystallization. Due to the 'single-step' nature of this approach and the use of relatively high temperatures (700-1200 °C), a number of complex and potentially overlapping processes may occur during this one-step processing. A further complication in understanding these processes is the rapid heating rates ($>100 \text{ Ks}^{-1}$), which are frequently employed in the *one-step* process. These heating rates are typically achieved through the use of

either rapid thermal annealing furnaces or by directly inserting the film into a furnace preheated to the crystallization temperature. Even though rapid heating rates are used, cracking in the films is typically not observed. This is believed to be due to the delay of condensation reactions between the precursors species and since the network is more compliant the film is freer to densify without cracking. Both precursor chemistry (reactivity and decomposition temperature) and heating rate can be used to control the densification behavior of the film. Substrate, solution and material chemistry, transformation pathway, and thermal processing conditions all can have a significant effect on thin film microstructure and orientation.

In the *two-step* method, the as-deposited film is subjected to pyrolysis to separate organic species prior to crystallization at high temperatures. During the first step of the process, the film is typically placed on a hot plate held at 200–400 °C for burnout of the organic species. While it might be expected that this type of rapid heat treatment would cause cracking, it appears that this is often the best approach. It has been proposed that this approach allows for the removal of the organic constituents prior to the collapse of the amorphous network, thus minimizing cracking and blistering. The film shrinkage that takes place during the pyrolysis step is strongly related to the nature of the precursor species and can generate stresses in the films well in excess of 100 MPa. The magnitude of the stress and whether film cracking occurs will depend, in part, on the reactivity of the precursors. Films prepared from less reactive precursors retain their viscoelastic character longer during processing, and hence the solvent can be removed without producing significant stress. During pyrolysis, the film may shrink in the thickness direction by 50–70%. Now that films with thicknesses ranging from 0.5 to 2.0 μm are required for many applications, they are typically fabricated by a multi-layering approach, wherein deposition is immediately followed by pyrolysis and then each layer is crystallized before the next deposition. Alternatively, multiple layers are deposited and pyrolysed prior to crystallization anneal (Bhuiyan, 2006).

Since pyrolysed films are typically amorphous, film crystallization occurs by a nucleation and growth process. The theoretical description of nucleation and growth

in solution-derived films is analogous to that used to describe crystallization in traditional glasses. The characteristics of the nucleation and growth process serve to define the resulting microstructure. For example, films that display microstructures where only interface nucleation of the final crystalline phase takes place are frequently columnar in nature, whereas those in which nucleation occur throughout the film are typically polycrystalline with equiaxed grains.

From a thermodynamic perspective, it has been demonstrated that the driving forces that govern the transformation from the amorphous film into the crystalline ceramic can play a significant role in defining the active nucleation events, and thereby film microstructure. The diagram shown in Figure 3.6 demonstrates the differences in free energy between the solution-derived amorphous film and the crystalline ceramic phase. While this diagram does not necessarily provide insight into the transformation pathway the film undergoes, it is useful in understanding the role that the driving force (ΔG_v , the energy difference between the amorphous and crystalline states) can have on the transformation process and thus the final microstructure of the ceramic film.

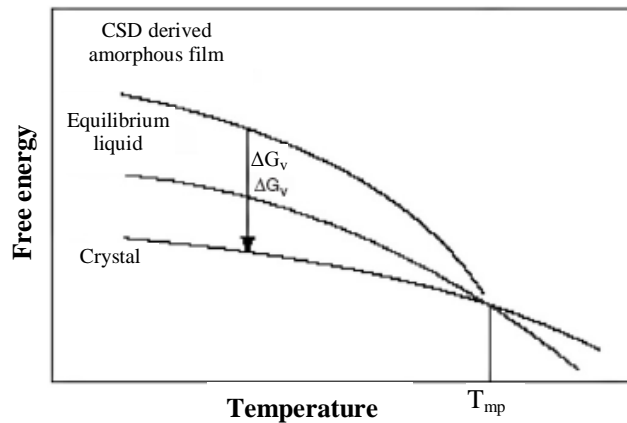


Figure 3.6 Free energies of a CSD derived film (Bhuiyan, 2006).

Examination of the figure indicates that the crystallization driving force is determined by the free energy of the two material states and the temperature at which crystallization occurs. The free energy of the amorphous phase is greater than the

supercooled equilibrium liquid due to surface area, residual hydroxyl, and excess free volume contributions to the free energy. From standard nucleation and growth theory, the homogenous nucleation of a spherical crystallite in an amorphous film, the Gibbs free energy change is given by:

$$\Delta G_{\text{homo}} = V(\Delta G_v + \Delta G_e) + A\gamma \quad (3.10)$$

where V , A , ΔG_v , ΔG_e , and γ are, respectively, the nuclei volume, the interfacial area between the nuclei and the parent amorphous phase, the difference in volume free energy, the elastic strain energy, and the interfacial energy of the newly formed interface. By differentiation of Equation 3.10, the energy barrier for a stable homogenous nucleation event can be derived as:

$$\Delta G_{\text{homo}}^* = \frac{16\pi\gamma^3}{3(\Delta G_v + \Delta G_e)^2} \quad (3.11)$$

Inhomogeneities, such as internal or external surfaces or other defects, can significantly reduce the energy barrier to nucleation. A nucleus formed in the shape of a spherical cap results in less of an increase in surface energy than homogeneous nucleation of a sphere of equivalent volume. The shape of the cap, and thus the energy barrier to nucleation, depends upon the associated surface tension forces. The relationship among these forces is given by

$$\gamma_{\text{sa}} = \gamma_{\text{ca}} \cos \theta + \gamma_{\text{sc}} \quad (3.12)$$

where the subscript s stands for substrate, c indicates the crystalline nucleus, and a represents the amorphous matrix. The initial surface energy of the heterogeneous nucleation site is γ_{sa} , and γ_{ca} and γ_{sc} are the newly created surface energies between the nucleus and the matrix and the nucleus and the substrate, respectively. The contact angle between γ_{ca} and γ_{sc} is θ . The energy barrier to nucleation is reduced in proportion to θ , and the nucleation is said to be heterogeneous. Strain energy effects can alter interfacial energies but because these alternations cannot be verified by

experiment, they are neglected in this simplified model. For $\theta \neq 0$, the heterogeneous nucleation barrier can be described by

$$\Delta G^*_{\text{hetero}} = \Delta G^*_{\text{homo}} f(\theta) = \frac{16\pi\gamma^3}{3(\Delta G_v + \Delta G_e)^2} f(\theta) \quad (3.13)$$

where $f(\theta)$ is defined as;

$$f(\theta) = \frac{(2 + \cos \theta)(1 - \cos \theta)^2}{4} \quad (3.14)$$

From Equation 3.14, it can be seen that the term $f(\theta)$, and therefore the nucleation barrier would disappear as the contact angle θ approaches zero. However, crystallization under these conditions for standard solution processing routes is not observed due to the ‘kinetic barrier’ to crystallization. Although more detailed analyses are possible, only a few concepts are required to use the diagram in Figure 3.5 and the basic nucleation and growth equations to interpret film crystallization behavior. These are listed below;

1. As the crystallization driving force is increased, bulk nucleation becomes as probable as interface nucleation. Even though the $f(\theta)$ term results in a lower energy barrier for interface nucleation, when the crystallization driving force is high (i.e., in a typical heat treatment scenarios) there is more than sufficient energy to surmount the energy barriers for all (including less energetically favorable) nucleation events.

2. For films that transform with smaller driving forces, the energy barrier heights for different nucleation events are separated to a greater extent. This makes interface nucleation in some films much more preferred than bulk nucleation, and increases the importance of the substrate in influencing the thin film microstructure.

3. The effects of crystallization temperature on driving force and nucleation must be considered. When using high heating rates, the physical processes leading to

densification and crystallization of the film are delayed to higher temperatures. This causes nucleation to occur at a higher temperature than with conventional heating. Under these conditions, crystallization occurs with lower driving forces and due to the $f(\theta)$ term, lower energy heterogeneous nucleation events become more important.

4. Unless rapid thermal processing techniques are used, film crystallization usually begins during heating to the annealing temperature. Therefore, as the temperature of the sample is increased more thermal energy becomes available to surmount the barriers for nucleation events that are not necessarily the most favorable energetically. This can lead to film microstructures controlled by nucleation and growth processes associated with more than one nucleation event.

CHAPTER FOUR

EXPERIMENTAL STUDIES

4.1 Substrate Materials

Substrate material or high temperature superconducting thin films must fulfill the following fundamental requirements:

- It must be thermally and chemically stable at the elevated temperatures which superconductor deposition is carried out. Also, there should not be any chemical interaction at the interface between coating and substrate.
- Differential thermal expansion of the substrate and superconductor film must be similar. If the substrate has a higher thermal expansion coefficient than the superconductor, it will contract more upon cooling from the deposition temperature, causing a compressive stress in the superconducting layer. For substrates with a lower thermal expansivity, the superconductor will be in tension. Any stress may lead to a degradation of the superconducting properties. Hence a substrate should ideally have a thermal expansivity which is matched to, or slightly higher than superconducting film.

Table 4.1 CrysTec GmbH Company technical specifications for STO and LAO single crystal substrates.

	SrTiO₃ (STO)	LaAlO₃ (LAO)
Growth method	Verneuil	Czochralski
Crystal structure	cubic	pseudocubic
Lattice constant	a= 0.3905	a=0.3821
Melting point	2353 K	2380 K
Hardness	6.0-6.5 (Mohs)	6.0 (Mohs)
Orientation	(100)	(100)
Size	10x10 mm ²	10x10 mm ²
Thickness	1 mm	1 mm
Surface	one side epipolished	one side epipolished
Thermal conductivity	12 W/m K (100°C)	10 W/m K (100°C)
Thermal expansion	$9 \times 10^{-6} \text{ K}^{-1}$	$10 \times 10^{-6} \text{ K}^{-1}$

- The surface of the substrate must be suitably polished, stable and reasonably robust. If the substrate surface is very rough, the superconductor will not be able to form a smooth, continuous well oriented film.

(100) oriented commercial SrTiO₃ (STO) and LaAlO₃ (LAO) single crystal oxides from CrysTec GmbH Company with dimensions of 10mm x10mm x1mm were used as substrates in order to prepare superconducting thin films. The physical properties of these substrates are given in Table 4.1. Before deposition, the substrates were cleaned in an ultrasonic bath using acetone in order to eliminate impurities from the sample surface. Afterwards, substrate surfaces were dried under argon gas atmosphere.

4.2 Production Procedure

4.2.1 Solution Preparation

One of the most important issues in the MOD processing of coated conductor is the synthesis of MOD precursor solution. Four different types of solutions were prepared in this study. First solution (SolA) was prepared by dissolving commercially available YBCO powder in propionic acid and trifluoroacetic acid (TFA). The flow chart of the solution preparation is illustrated in Figure 4.1. Precursor powder was weighted out in a flask, propionic acid and TFA with a molar ratio of 8:1 was added to dissolve powder. This mixture was stirred on a magnetic stirrer at 120 °C with low rpm until the solution completely dissolves. This solution was refined under vacuum atmosphere with evaporator in order to remove the solvent and to yield a glassy dark blue residue. After the formation of a dark blue, highly viscous state due to the evaporation, the TFA precursor was dissolved in acetone and propionic acid, which was added in a molar ratio of 3:1 and the final concentration was adjusted to a concentration of 0.25 M.

Second type solution (SolB) was prepared by dissolving Y, Ba and Cu acetates into distilled water in a 1:2:3 cation ratio with arbitrary quantity of (~ 20 ml TFA for

50 ml final solution) TFA at room temperature. This aqueous solution was refined under vacuum atmosphere with evaporator in order to remove the solvent and to yield a glassy blue residue containing impurities of water and acetic acid. Later, the residue was dissolved in sufficient methanol and refined again to expel the impurities to yield a glassy blue residue containing methanol. This method is called “solvent into gel method (SIG)”. Sticky materials of metal trifluoroacetates inherently confine the other materials with hydrogen bonds during the refining process. In the SIG method, highly purified coating solution was obtained by replacing the other materials with the resulting solvent. After two cycles of refining processes, the resultant blue residue was dissolved in methanol to give a solution with a metallic ion concentration of 0.25 M. The solution preparation process was illustrated in Figure 4.2. All solution preparation process took place under Ar atmosphere after evaporation of water from the system completely.

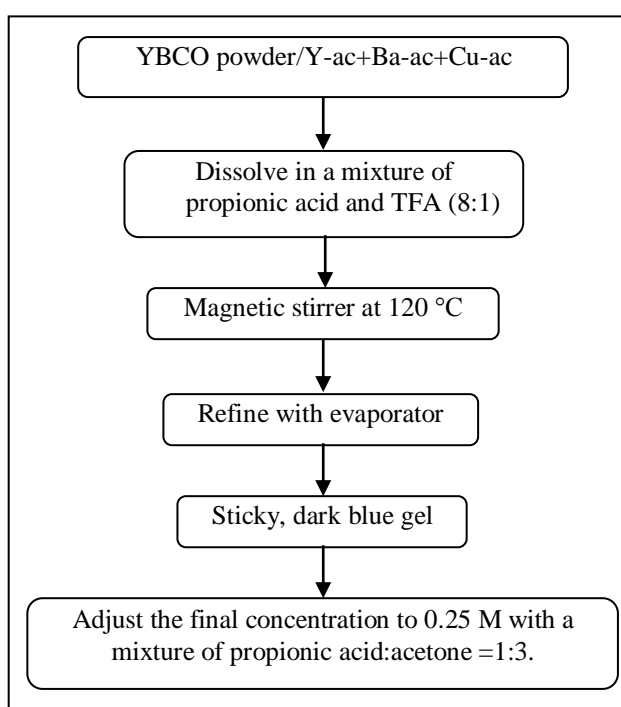


Figure 4.1 Schematic illustration of SolA and SolD preparation.

Preparation of the third type solution SolC is quite similar to the SolB. The only difference is, instead of methanol, ethanol was used as a solvent.

During SolD preparation, acetates of Y, Ba and Cu were used instead of commercial YBCO powder. All acetates were weight out in a flask and all procedures which were applied for SolA repeated for SolD too. Finally, Gadolinium acetate was used instead of Yttrium acetate and a new solution was prepared.

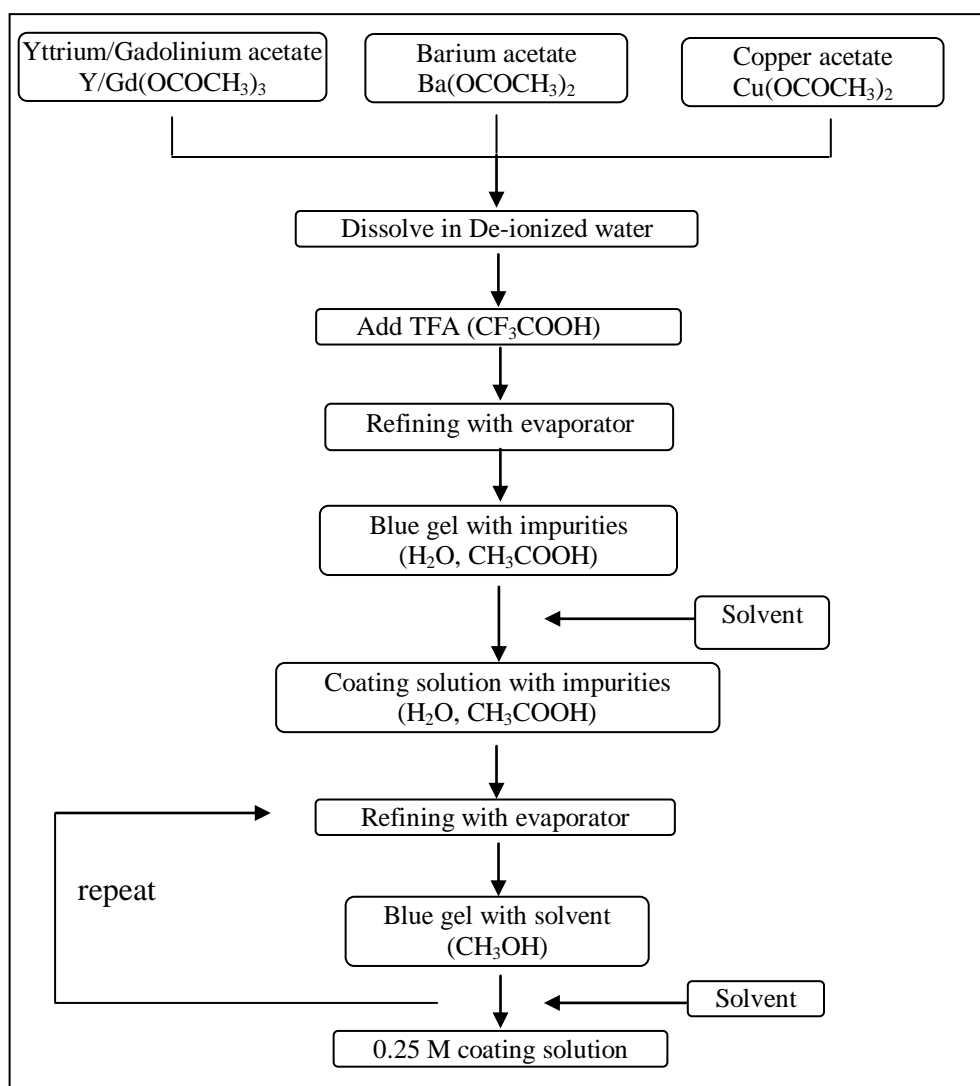


Figure 4.2 Schematic illustration of SolB, SolC and SolE preparation.

All solutions were prepared 0.25 M and 50 ml. Then, they were all divided into four parts each 10 ml, and different amounts of zirconium were added to each part by dissolving Zr(IV)-2.4-pentanedionate in the solutions. The Zr concentrations were adjusted to 0, 6, 12 and 18 mol% Zr regarding to stoichiometric precursors. For convenience, Table 4.2 summarizes the abbreviated names of precursor solutions and

films prepared from these solutions. In the solution abbreviations, “Sol” represents the name of solution. Different types of films abbreviated as “Film (type of substrate- from which solution film has prepared).”

Table 4.2 A brief summary which describes name of solutions, type of precursors and solvents used for preparing these solutions and name of the films prepared from this solutions.

Name of solution	Type of precursors	Type of solvents	Doped-BZO concentration (mol%)	Name of film	
				STO substrate	LAO substrate
SolA0	YBCO powder	Propionic acid, TFA, Acetone	0	F(S-A0)	-
SolA1	YBCO powder	Propionic acid, TFA, Acetone	6	F(S-A1)	-
SolA2	YBCO powder	Propionic acid, TFA, Acetone	12	F(S-A2)	-
SolA3	YBCO powder	Propionic acid, TFA, Acetone	18	F(S-A3)	-
SolB0	Y-ac, Ba-ac, Cu-ac	Distilled water, TFA, Methanol	0	F(S-B0)	F(L-B0)
SolB1	Y-ac, Ba-ac, Cu-ac	Distilled water, TFA, Methanol	6	F(S-B1)	F(L-B1)
SolB2	Y-ac, Ba-ac, Cu-ac	Distilled water, TFA, Methanol	12	F(S-B2)	F(L-B2)
SolB3	Y-ac, Ba-ac, Cu-ac	Distilled water, TFA, Methanol	18	F(S-B3)	F(L-B3)
SolC0	Y-ac, Ba-ac, Cu-ac	Distilled water, TFA, Ethanol	0	F(S-C0)	F(L-C0)
SolC1	Y-ac, Ba-ac, Cu-ac	Distilled water, TFA, Ethanol	6	F(S-C1)	F(L-C1)
SolC2	Y-ac, Ba-ac, Cu-ac	Distilled water, TFA, Ethanol	12	F(S-C2)	F(L-C2)
SolC3	Y-ac, Ba-ac, Cu-ac	Distilled water, TFA, Ethanol	18	F(S-C3)	F(L-C3)
SolD0	Y-ac, Ba-ac, Cu-ac	Propionic acid, TFA, Acetone	0	F(S-D0)	F(L-D0)
SolD1	Y-ac, Ba-ac, Cu-ac	Propionic acid, TFA, Acetone	6	F(S-D1)	F(L-D1)
SolD2	Y-ac, Ba-ac, Cu-ac	Propionic acid, TFA, Acetone	12	F(S-D2)	F(L-D2)
SolD3	Y-ac, Ba-ac, Cu-ac	Propionic acid, TFA, Acetone	18	F(S-D3)	F(L-D3)
SolE0	Gd-ac, Ba-ac, Cu-ac	Distilled water, TFA, Ethanol	0	F(S-E0)	F(L-E0)
SolE1	Gd-ac, Ba-ac, Cu-ac	Distilled water, TFA, Ethanol	6	F(S-E1)	F(L-E1)
SolE2	Gd-ac, Ba-ac, Cu-ac	Distilled water, TFA, Ethanol	12	F(S-E2)	F(L-E2)
SolE3	Gd-ac, Ba-ac, Cu-ac	Distilled water, TFA, Ethanol	18	F(S-E3)	F(L-E3)

4.2.2 Coating Procedure

Film deposition on single crystal substrates was performed by spin coating technique. This is a compatible and precise technique for uniform deposition of metal oxide thin films, polymer coatings and metal organic thin films. A typical spin coating process involves deposition of a small drop ($\approx 0.1-1$ cc) of precursor solution onto the center of a substrate and then spinning the substrate at high speeds. Centripetal acceleration causes the excess amount of liquid to spread around leaving a thin film of precursor solution on the substrate surface. Schematically description of this process is depicted in Figure 4.3. Final film thickness depends on the nature of the precursor solution as viscosity, drying rate and surface tension in addition to the parameters chosen for the spin coating process.

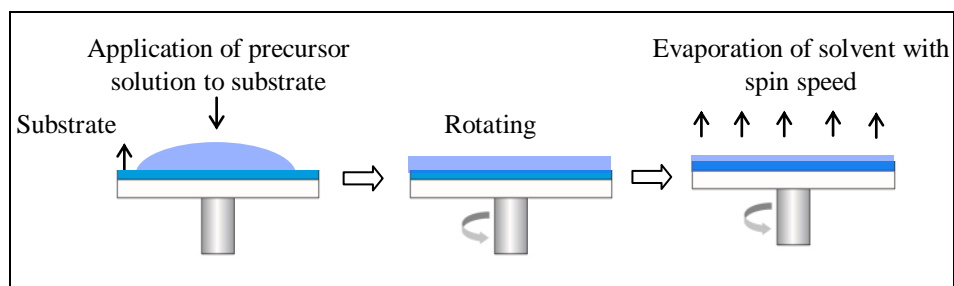
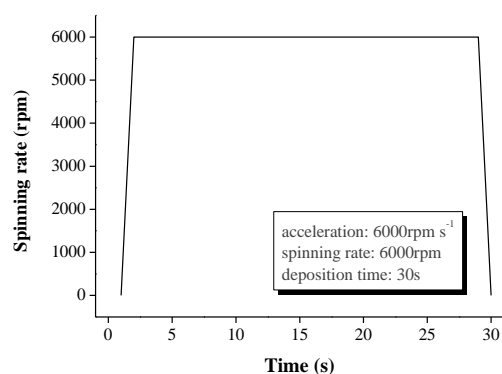


Figure 4.3 Schematic description of spin coating process.

G3P-8 Model Cookson Electronics spin coater (Figure 4.4 (a)) was used to produce superconducting thin films on single crystal substrates at a rotation speed of 6000 rpm and acceleration speed of 6000 rpm s^{-1} for 30 seconds as illustrated in Figure 4.4 (b). It is believed that the precursor film can easily absorb water from the circumstance with a high relative humidity during the spin coating step. Therefore, all coating process took place in a dry nitrogen atmosphere at $-25 \text{ }^\circ\text{C}$ dew point in order to prevent film to absorb humidity from the air.



(a)



(b)

Figure 4.4 (a) Image of spin coater, (b) Spin coating program which is used for thin film production process.

4.2.3 Heat Treatment

Coated samples were heat treated according to the heat treatment profile shown in Figure 4.5. During the heat treatment process, dry gas treatment up to $60 \text{ }^\circ\text{C}$ prevents the gel film from absorbing humidity that would deteriorate film integrity. Above $60 \text{ }^\circ\text{C}$, humidified O_2 is introduced to suppress the sublimation of Cu trifluoroacetate.

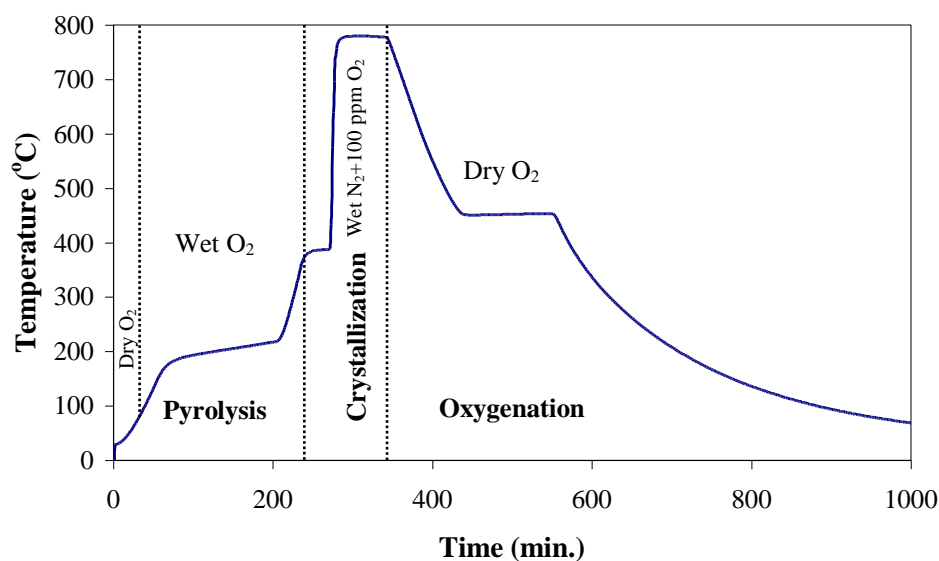


Figure 4.5 Heat treatment profile for the production of undoped and BZO doped YBCO films. All films are crystallized at 780 °C and oxygenated at 450 °C.

Metal trifluoroacetates decompose and harmful gaseous residues are removed during the pyrolysis to give a precursor film. After that, the fluoride containing precursor film is fired at a maximum temperature of 780 °C under humidified N₂ mixed with 100 ppm O₂ and then oxygenated at 450 °C to obtain the final superconducting film. Humid atmospheres mentioned above in the furnace were produced by bubbling the inlet gas through an attached reservoir of distilled water at room temperature.

4.3 Solution Characterization

4.3.1 Viscosity Measurement

Rheology is the science of flow and deformation behavior caused by external forces. Molecular structure, temperature, pressure, time and shear rate predominantly influences viscosity of the precursor solution. The rheological measurements were conducted using a Bohlin Instruments CVO 100 Rheometer with 2° conic plate geometry 60 mm in diameter and 70 μm gap sizes between plates. The viscosity values of precursor solutions were determined at constantly increasing 1-1200 Hertz frequency and 25 °C at single shear mode. Additionally, viscosity values under

increasing temperature conditions were determined at constant 400 Hertz frequency between 20-60 °C for all solutions. The rheological properties of all solutions were comparatively studied to characterize their gelation behaviours.

4.3.2 Contact Angle Measurement

The wetting behavior of the solutions on STO and LAO substrates can be characterized by the contact angle γ , which is determined by the balance of the energies of the three interfaces: solid–liquid γ_{SL} , liquid–vapor γ_{LV} and solid–vapor γ_{SV} . The contact angle is given by Young’s Equation 4.1, which is valid for the case of incomplete wetting:

$$\gamma_{SV} + \gamma_{SL} = \gamma_{LV} \cos \gamma \quad (4.1)$$

In order to obtain a complete homogenous coverage of the STO and LAO single crystal substrates leading to homogenous layer properties, a very small wetting angle close to 0° was required.

Contact angle measurements of the solutions were performed with Contact Angle Meter-CAM 100 (KSV Instruments Ltd., Finland). It is a compact CCD camera based instrument for measurement of contact angles (CA) of liquids on solids. Goniometry involves the observation of a sessile drop of test liquid on a solid substrate. The basic elements of a goniometer include a light source, sample stage, lens and image capture. Contact angle can be assessed directly by measuring the angle formed between the solid and the tangent to the drop surface.

4.4 Material Characterization

4.4.1 Differential Thermal Analysis-Thermogravimetry (DTA-TG)

Thermal methods are based upon the measurement of the dynamic relationship between temperature and some property of the system such as mass and heat

absorbed by or evolved from it. Differential Thermal Analysis (DTA) and Thermogravimetry (TG) are the most important thermal methods used in characterization of materials. In DTA the heat absorbed or emitted by a system is observed by measuring the temperature difference ΔT between the sample and an inert reference material (generally alumina powder), as the temperature of both is increased at a constant rate. TG analysis is concerned with the change in weight of a material as its temperatures changes. Many series of thermal analysis techniques can be combined with other non-thermal technique for valuable multiple-parameter information as in our DTA/TGA system.

The decomposition of the gel was also studied under N_2 flowing by using Shimadzu DTG-60H Model Differential Thermal Analysis/ Thermal Gravimetric Analysis (DTA-TGA) in order to obtain information about the decomposition behavior of the gels to adjust the thermal treatment accordingly. Thermal data were analyzed using TA60 software program supplied with the instruments.

4.4.2 Fourier Transform Infrared Spectroscopy (FTIR)

Fourier Transform Infrared Spectroscopy (FTIR) is a powerful tool for identifying types of chemical bonds in a molecule by producing an infrared absorption spectrum that is like a molecular "fingerprint". Each different material is a unique combination of atoms, so two different compounds never produce the exact same infrared spectrum. Therefore, infrared spectroscopy can result in qualitative analysis of every different kind of material. By interpreting the infrared absorption spectrum, the chemical bonds in a molecule can be determined. In principle, molecular bonds vibrate at various frequencies depending on the elements and the type of bonds. For any given bond, there are several specific frequencies at which it can vibrate. According to quantum mechanics, these frequencies correspond to the ground state (lowest frequency) and several excited states (higher frequencies). One way to cause the frequency of a molecular vibration to increase is to excite the bond by having it absorb light energy. For any given transition between two states the light energy (determined by the wavelength) must exactly equal the difference in the energy

between the two states. The energy corresponding to these transitions between molecular vibrational states is generally 1-10 kilocalories/mole which corresponds to the infrared portion of the electromagnetic spectrum. The results are generally plotted as a function transmittance or absorbance versus wavelength. The conversion between transmittance to absorbance data is:

$$A = \log\left(\frac{1}{T}\right) \quad (4.2)$$

where A is absorbance and T is transmittance.

In addition to qualitative analysis, the size of the peaks in the spectrum is a direct indication of the amount of material present. With suitable software algorithms, infrared is also an excellent tool for quantitative analysis.

The technique of Attenuated Total Reflectance (ATR) has in recent years revolutionized solid and liquid sample analyses because it combats the most challenging aspects of infrared analyses namely sample preparation and spectral reproducibility. An ATR accessory operates by measuring the changes that occur in a totally internally reflected infrared beam when the beam comes into contact with a sample as indicate in Figure 4.6.

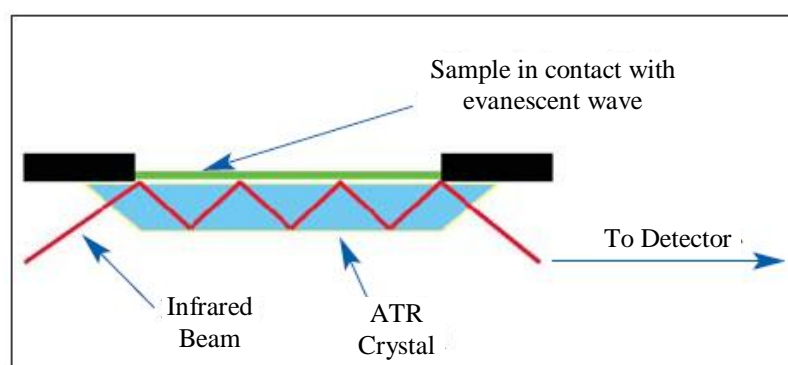


Figure 4.6 Schematic representation of an ATR system.

An infrared beam is directed onto an optically dense diamond crystal with a high refractive index at a certain angle. This internal reflectance creates an evanescent

wave that extends beyond the surface of the crystal into the sample held in contact with the crystal. It can be easier to think of this evanescent wave as a bubble of infrared that sits on the surface of the crystal. This evanescent wave protrudes only a few microns (0.5-5 μm) beyond the crystal surface and into the sample. Consequently, there must be good contact between the sample and the crystal surface. In regions of the infrared spectrum where the sample absorbs energy, the evanescent wave will be attenuated or altered. The attenuated energy from each evanescent wave is passed back to the IR beam, which then exits the opposite end of the crystal and is passed to the detector in the IR spectrometer. The system then generates an infrared spectrum.

The infrared spectra of all liquid and coated samples were recorded with a Perkin Elmer Spectrum BX instrument equipped with ATR apparatus in the spectra range between 4000 and 650 cm^{-1} with a resolution of 4 cm^{-1} .

4.4.3 X-Ray Diffraction (XRD)

X-ray diffraction (XRD) is a versatile technique used for identifying the crystalline phases present in films and analyzes structural properties such as stress, grain size, phase composition and crystal orientation. Generally, it is possible to perform three types of measurements with XRD. These are θ -2 θ scan, ω -scan and ϕ -scan. A scheme of these three angles is illustrated in Figure 4.7.

A θ -2 θ scan XRD uses a beam of X-rays bombarding a specimen from various angles, θ . The X-rays are diffracted according to the as they are reflected from successive planes formed by the crystal lattice of the material. This diffraction can be expressed by Bragg's Law of diffraction:

$$n\lambda = 2d \sin \theta \quad (4.3)$$

in which, n = integer, λ = wavelength, θ =diffraction angle and d = spacing between crystallographic planes.

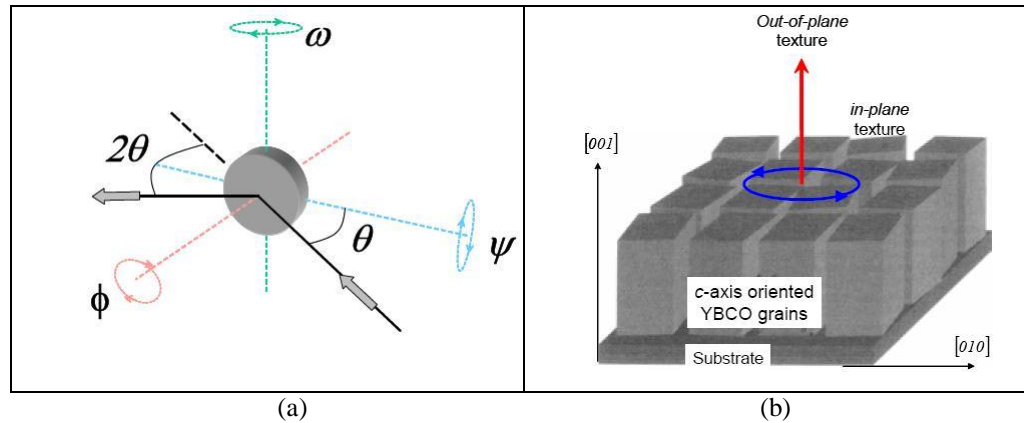


Figure 4.7 Scheme of (a) θ , ω , ϕ and ψ angles in XRD and (b) out-of plane and in-plane texture in a YBCO film with large c-axis oriented grains perpendicular to substrate surface.

By varying the angle of incidence, a diffraction pattern emerges that is characteristic of sample. The pattern is identified by comparing it with an internationally recognized data base powder diffraction file (PDF) reference patterns. In YBCO and GdBCO epitaxial films with the grains aligned in preferred orientation along (001) lattice planes, the intensity relationship described inside of the PDF files are not valid, because they change according to the degree orientation of the grains respect to substrate surface. For example, the presence of (103) YBCO reflection, which has the maximum intensity according to the PDF file, denotes grains aligned randomly respect to the substrate surface. This means it is a non-textured film, while (001) reflections denote YBCO grains aligned with c-axis perpendicular to the substrate surface and (h00) reflections denote YBCO grains aligned with a-axis perpendicular to substrate surface. XRD was carried out using a Philips Diffractometer with Co K_{α} $\lambda = 0.17902$ nm radiation, at a step size of 0.001, 1 second time/step and 0.001 scan speed to ascertain the phase purity of the films.

On the other hand, the ω -scan XRD measurements (rocking curve) characterize the out-of-plane texture of films. It measures a single Bragg peak, for example (005) YBCO peak ($2\theta \sim 35^\circ$), as the sample is tilted ω degree like in Figure 4.7 within the diffraction plane. It is possible to obtain information about the degree of uniaxial epitaxy by determining the FWHM value of the profile $\Delta\omega$.

As a third measurement, the pole figure and ϕ -scan XRD measurements characterize the in-plane texture of films. Figure 4.8 illustrates two possible cases of in-plane texture. Both random and textured orientations are observable with this scan. Also, the FWHM value provides the degree of in-plane texture. The in-plane texture analyses including ϕ -scan were carried out using a Philips diffractometer delivering a pure Cu K_α radiation with a wavelength of $\lambda = 0.15406$ nm.

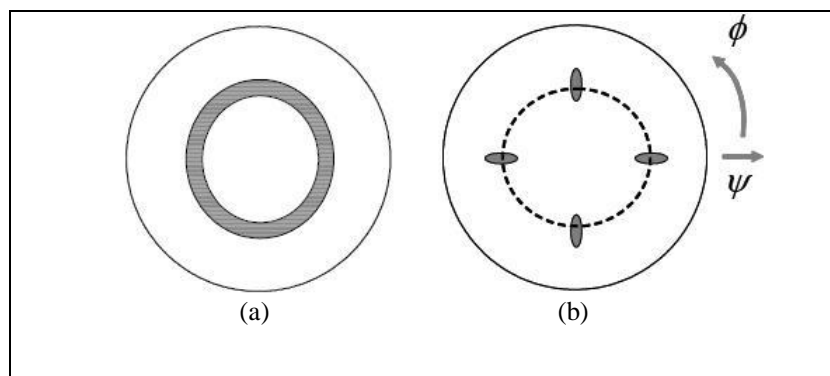


Figure 4.8 Pole figures of films with (a) random and (b) textured orientation.

4.4.4 Scanning Electron Microscopy (SEM)

The Scanning Electron Microscope (SEM) is a versatile electron microscope that images a sample by scanning it with a high-energy beam of electrons in a raster scan pattern. In Typical SEM configuration, electrons are thermoionically emitted from a tungsten or LaB₆ cathode filament towards an anode. The electron beam, with a typical energy ranging from a few KeV to 30 KeV, is focused by successive lenses in a beam with a very fine spot size. When the beam impact with the surface, different kind of electrons can be detected. The types of signals produced by an SEM include secondary electrons (SE), back-scattered electrons (BSE) and characteristic X-rays.

Secondary electron signals result from interactions of the electron beam with atoms at or near the surface of the sample. SEM can produce very high-resolution images of a sample surface with a secondary electron imaging (SEI). Due to the very narrow electron beam, SEM micrographs have a large depth of field yielding a characteristic three-dimensional appearance useful for understanding the

surface structure of a sample. A wide range of magnifications is possible till 300 000 times theoretically.

Back-scattered electrons (BSE) are beam electrons that are reflected from the sample by elastic scattering. BSE are often used in analytical SEM along with the spectra made from the characteristic X-rays. Because the intensity of the BSE signal is strongly related to the atomic number (Z) of the specimen, BSE images can provide information about the distribution of different elements in the sample.

Characteristic X-rays are emitted when the electron beam removes an inner shell electron from the sample, causing a higher energy electron to fill the shell and release energy. These characteristic X-rays are used to identify the composition and measure the abundance of elements in the sample.

The surface morphologies of thin films were observed by Philips XL20 Scanning Electron Microscopy and JEOL-JSM 6060 Scanning Electron Microscopy with an Energy Dispersive X-ray spectroscopy (IXRF System EDS) system attachment. Accelerating voltage of 20 kV was used for the SEM imaging.

4.4.5 Atomic Force Microscopy (AFM)

Atomic Force Microscopy (AFM) is an useful tool for assessing the morphological quality of films. A Digital Instruments Nanoscope III was used in tapping mode to obtain AFM images of at least one film in each batch measured. In 'Tapping Mode' technique the probe is oscillated at a constant frequency as the AFM head scans across the surface. The amplitude of oscillation of the tip varies as it moves nearer to the surface of the film, this change is used as feedback to control the sample-tip distance and deduce the surface height of the film. In general AFM measurements revealed that it was difficult to obtain vicinal films with as high a quality as the best c -axis films. Even the best films exhibited pin-hole defects or outgrowths. The AFM employed was well calibrated in the z -axis, a maximum error of +/- 2 nm was observed imaging 180 nm deep pits on a calibration sample. The

AFM could therefore be used to obtain film thickness by measuring the height of chemically etched steps. Additionally, areal surface roughness (S_a) values were determined for investigated samples. All measurements were performed at a 20 μm imaging area, 1 second time/line speed and 1024 points/line resolution. Film thickness values of films were also measured via AFM by etching half of the coating and removing it from substrate surface. The step height from substrate to the coating is a representative value for film thickness.

4.5 Electrical Characterization

4.5.1 Inductive T_c Measurement

The transition of the conductor material sample from the normal state to the superconducting state is accompanied with a sharp change of several physical quantity values as T_c and J_c . The transition temperature of a superconductor is defined as the temperature below which a superconductor exhibits zero resistance and perfect diamagnetism in the limit of zero applied magnetic field and without any transport current.

The standard method of determination of the superconductor critical temperature T_c comprises a conventional four point technique of measurement of R vs. T dependency, where R is the electrical resistivity and T is the temperature of the sample. This method requires making of electrical contacts on the sample surface by soldering, vacuum deposition, pressuring etc. Generally, contacting is a large disadvantage of this technique. In some cases, the electrical contacting can cause a change of the chemical properties of the samples, mainly in the vicinity of the electrodes. It is significant particularly for the thin film superconducting samples. Several contactless measuring methods using the change of the self inductance, of a coil located in the vicinity of measured sample or the change of mutual inductance of two coils separated by the sample have been developed.

The inductive transition temperature measurement system generally uses mutual inductance method based on the Meissner-Ochsenfeld effect, expelling the magnetic field from the interior of the bulk superconductor in the superconducting state, even if the magnetic field was already within the sample before cooling.

The cryogenic probe design with sample, coils and temperature sensor is in Figure 4.9. The sample is sandwiched between the coils. The phosphorus-bronze spiral presses the coils and sample together to provide a good mutual magnetic coupling. The temperature sensor is inserted into a hole in the coil holder. The sample's temperature control is made with the help of the power control of heating spiral. The probe with the primary and secondary coils, the sample, the temperature sensor and the heating wire are closed in thermally isolated and placed in the inner atmosphere housing. The probe is immersed in the liquid nitrogen.

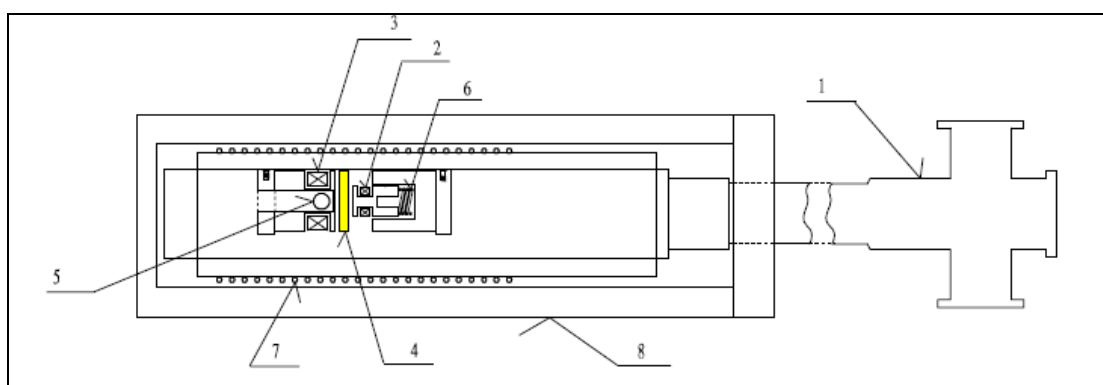


Figure 4.9 Schematic view of cryogenic probe design. (1) stainless cryogenic hinge with cable connectors; (2) primary coil, (3) secondary coil, (4) the sample, (5) temperature sensor, (6) phosphorus-bronze spiral for pressing the coils to the sample, (7) heating wire spiral and (8) housing (Konakovsky, 2001).

Different methods to determine T_c exist, e.g., onset, mid-point, $1 \mu\text{V}/\text{cm}$, tangent criterion and zero resistivity. The onset is suitable for obtaining the maximum T_c of non-homogeneous or multi-phase materials. The first point which deviates from the normal state curve, where particles with the highest T_c become superconducting, defines T_c (Figure 4.10 (a)). This point is hard to determine because of the noise of the signal and depends strongly on individual interpretation.

Zero-resistance is usually needed for applications and is, therefore important to know. The temperature, where the transition curve first reaches zero resistance, defines T_c . This point is also hard to determine because the 'zero-level' is not fixed and depends on the accuracy of the equipment. Onset and the zero-point are shown in Figure 4.10 (a). The transition width is obtained as the temperature difference between onset and zeropoint. A better and more commonly used method is the tangent criterion. A tangent is fitted to the slope of the transition and the intersection point with the extension of the normal state resistance defines T_c .

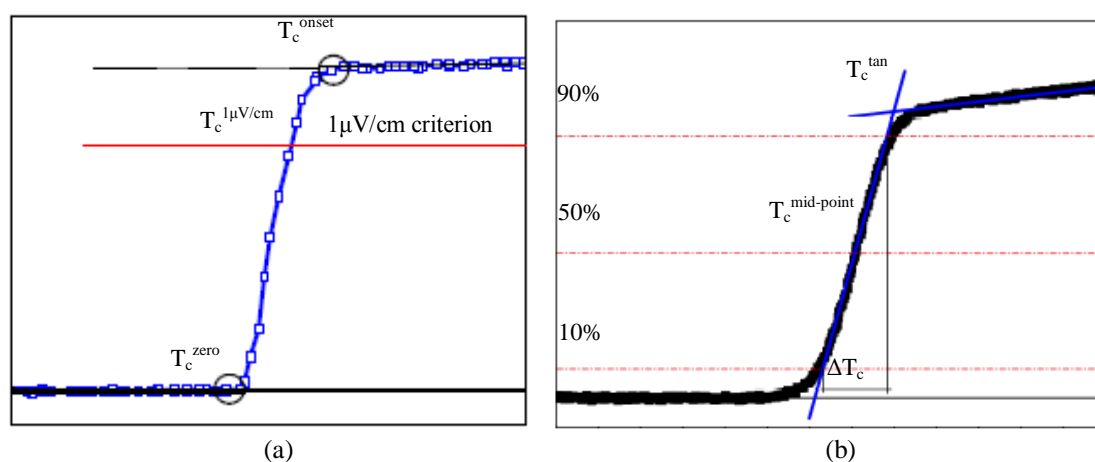


Figure 4.10 Determination of T_c by (a) onset, $1\mu V/cm$ and zero point, and (b) different criteria.

The transition temperature can also be determined from the mid-point of the transition from the normal to the superconducting state. Figure 4.10 (b) schematically shows a transition curve for a composite superconductor. A tangent to the curve in the normal state indicates 100 % resistance. Another straight line is fitted to the curve in the transition region. T_c is defined as the intersection point with the normal state fit line. Two other values at the intersections of the transition curve with 10% (T_{c10}) and 90 % (T_{c90}) of the normal state value can be used. The transition width ΔT_c is defined by $T_{c10} - T_{c90}$. The width and the shape of the transition give information about the purity, composition and strain dependence of the superconductor. In the case of transition width (ΔT_c), the higher ΔT_c is, the worst superconducting properties are. In general, the T_c value and the criterion always have to be specified. In our case, all measurements were performed by a home made apparatus as in Figure 4.9. T_{c90} values were recorded for all samples.

4.5.2 Inductive J_c Measurement

The critical current density (J_c) was measured inductively with a Theva Cryoscan. The instrument performs non-destructive mapping of the critical current density on HTS samples using an inductive technique. It offers accurate and fast measurements of the overall film quality as well as two-dimensional, high-resolution maps of the critical current distribution. This desktop instrument operates with liquid nitrogen as coolant and is very versatile with respect to sample size and shape, and practically accommodates any number of substrates that fit into the 10" x 8" scanning area. Inductive critical current density (J_c) measurements of samples were performed at 77 K and ambient pressure in self-field conditions.

4.5.3 Transport Measurement

Recognising that magnetic measurements are inadequate for HTSCs, it becomes necessary to measure the actual current moving down the sample, known as the transport current. In the basic transport measurement, current enters one end of the sample and leaves via the other end. At two points a known distance apart, the voltage difference is measured. For small currents, that voltage is zero, but when $J = J_c$ the sample becomes normal and the voltage suddenly rises. Accordingly, increasing J steadily until the voltage jumps is the easy way to determine J_c . HTSCs are generally so small that the total current flowing in a test is only milliamps in a thin film. Meanwhile, voltage probes may be only a millimeter apart, so that one must measure nanovolts accurately to determine the voltage in microvolts per meter. The National Institute of Standards and Technology lists seven parameters that must be specified with regard to voltage. These are; placement of contacts, separation of contacts, noise level, detection criterion (usually 1 μV), inductive voltage, thermoelectric voltage and meter response.

In our experiments, the critical current densities of superconducting films under magnetic field conditions were measured by using a Physical Properties Measurement System of Quantum Design Company with a magnet which is able to

generate magnetic field up to 9 T. The Quantum Design PPMS is an open architecture, variable temperature-field system, designed to perform a variety of automated measurements like magnetic, thermal and electrical measurements. It is schematically configured in Figure 4.11.

A programmable current source generates the excitation current and a nanovoltmeter (from Keithley Company) is used to measure the voltage developed across the sample while the temperature controller (from Lakeshore Company) reads the temperature for each value of voltage.

Samples are mounted on specially designed platforms named as pucks and held in place by either an adhesive or grease. The puck in Figure 4.12 (b) is one used to measure, leads from the sample would be soldered to the gold contacts and the sample attached to the puck frame by either a grease film or double-sided tape.

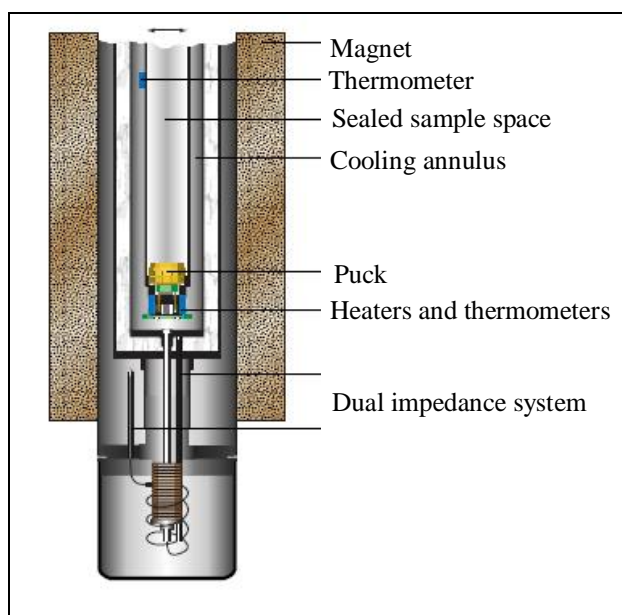
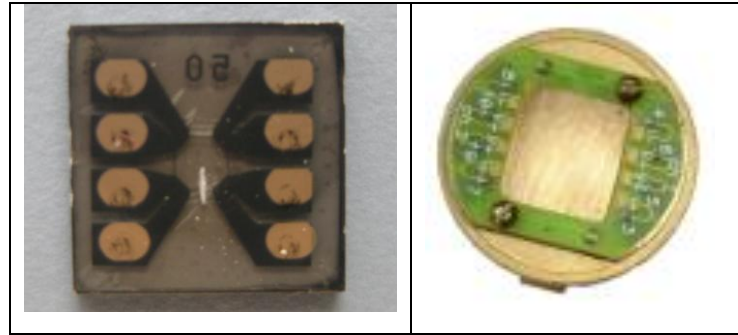


Figure 4.11 Schematic configuration of PPMS.

Transport measurements of our samples were carried out with a physical properties measurement system (PPMS) up to 6 T at 77 K on bridges of 0.8 mm length and 50 μm widths. For an estimation of the critical current, a criterion of $1 \mu\text{Vcm}^{-1}$ was used.



(a)

(b)

Figure 4.12 (a) Sample with gold contacts prepared for transport measurement and (b) Sample puck for transport measurement.

CHAPTER FIVE

RESULTS AND DISCUSSION

5.1 YBCO Thin Film Production from Commercially Available Oxide Powder

TFA-MOD process using metal acetates as starting materials is more cost effective than vacuum techniques, but highly purified metal acetates are rather expensive and thus it is desirable to find more economic route. Recently, several attempts to use oxide powders such as commercially available REBCO powder as starting materials have been reported which showed comparable J_c for the YBCO films (Shin et al., 2005).

In conventional TFA-MOD method, the acetates of Y, Ba and Cu dissolved in TFA are used as the precursor materials. As Lim et al. (2005) indicates, it is difficult to depress the formation of the BaF_2 phase, unless the processing conditions are precisely controlled. Due to the non-equilibrium chemical reactions based on the decomposition of the precursors, this method may have low reproducibility. Additionally, in so far as acetates are expensive, it is desirable to develop a new synthetic method of more reproducible and cost effective by selecting other precursors.

As a first step of experimental processes, commercially available YBCO powder precursor (Alfa Aesar 39534), which could be opened up the possibility of practical applications, was used for coating solution preparation.

5.1.1 Preparation and Characterization of Precursor Solution from YBCO Powder

Precursor powder was weighted out in a flask, propionic acid and TFA with a molar ratio of 8:1 was added to dissolve powder, as systematically indicated in Figure 5.1. This mixture was stirred on a magnetic stirrer at 120 °C with low rpm until the solution completely dissolves. This solution was refined under vacuum atmosphere with evaporator in order to remove the solvent and to yield a glassy dark

blue residue. After the formation of a dark blue, highly viscous state in terms of the evaporation, the TFA precursor was dissolved in acetone and propionic acid, which was added in a molar ratio of 3:1, and the final concentration was adjusted to a concentration of 0.25 M. The solution preparation process was adapted from the study performed by Engel, Thersleff, Hühne, Schultz, & Holzapfel, (2007) with BaHfO₃ particles in the YBCO film structure. All solutions were prepared as 0.25 M and 50 ml, before they were all divided into four parts whose each of them has 10 ml of solution, and different amounts of zirconium were added to each part by dissolving Zr(IV)-2.4-pentanedionate in the solutions. After this procedure, the Zr concentrations were adjusted to 0, 6, 12 and 18 mol% Zr regarding to stoichiometric precursors in order to tailor transport properties of YBCO based superconducting films.

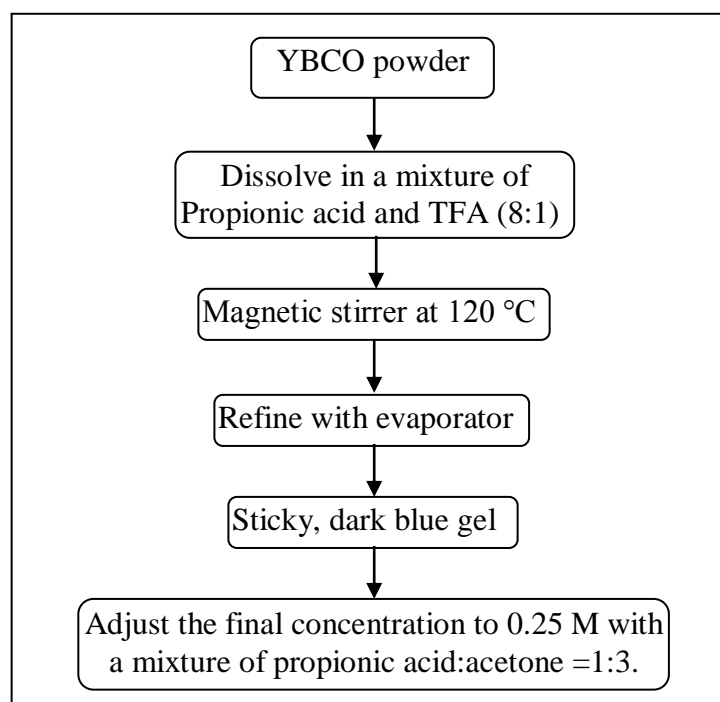


Figure 5.1 Schematic illustration of SolA preparation.

After solution preparation, first contact angle value of the solution on STO substrate was measured as 22.26°, which is good value for wettability in a thin film production. Afterwards a detailed rheological characterization was performed to determine shear profile and scrutinize effect of temperature on viscosity. The focus of attention here is mainly on the rheological properties in film production.

To appreciate properly how YBCO films function, it is first necessary to consider the rheology science of solution flow. Rheology is the science of flow and deformation behavior caused by external forces and measurements are under controlled testing conditions. Exclusively a few liquids come close to ideal liquids in their behavior. The vast majority of liquids show a rheological behavior that classifies them to a region somewhere between the liquids and the solids. They are in varying extents both elastic and viscous and may therefore be named viscoelastic. Instruments, which measure the viscoelastic properties of solids, semi-solids and fluids, are called as Rheometer. The main difference between the viscometer and rheometer is that the rheometer measures viscosity over a wide range of shear rates and viscoelasticity of fluids, semi-solids and solids. It is recognized that a rheometer is a highly sensitive device used to quantify viscoelastic properties of molecular structure of materials. The determined apparent properties can be used as a finger print or benchmark of the material (Somwangthanaroj, 2010).

The measurement of the viscosity of liquids by rheometer first requires the definition of the parameters that are involved in flow. Isaac Newton was the first to express the basic law of viscometry describing the flow behavior of an ideal liquid :

$$\tau = \eta \cdot \dot{\gamma} \quad (5.1)$$

in which, τ is shear stress, η is viscosity and $\dot{\gamma}$ is shear rate. The parallel plate model in Figure 5.2 assists to define both shear stress and shear rate.

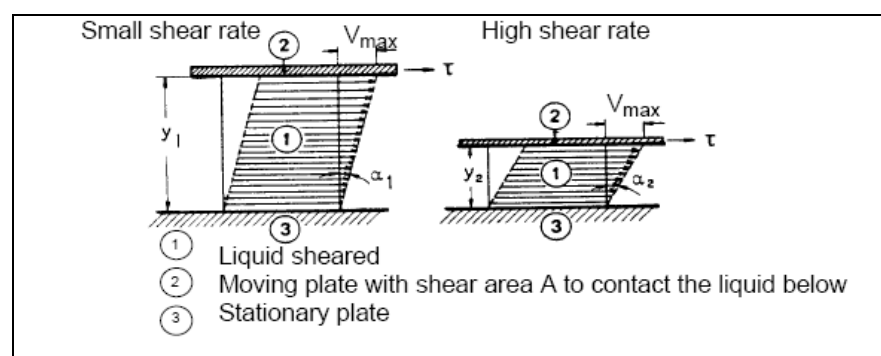


Figure 5.2 Flow between two parallel plates (Schramm, 2000).

A force F applied tangentially to an area A being the interface between the upper plate and the liquid underneath, leads to a flow in the liquid layer. The velocity of flow that can be maintained for a given force is controlled by the internal resistance of the liquid, by its viscosity.

$$\tau = \frac{F}{A} (N/m^2) \quad (5.2)$$

The shear stress τ causes the liquid to flow in a special pattern. The speed drop across the gap size is named shear rate (1/s).

Solving Equation 5.1 for the dynamic viscosity η gives:

$$\eta = \frac{\tau}{\dot{\gamma}} = \frac{N}{m^2} \cdot s = Pa \cdot s$$

where, Pa.s is the unit for dynamic viscosity. It also has a correlation with centipoises as; $1 \text{ mPa} \cdot \text{s} = 1 \text{ cP}$ (Schramm, 2000).

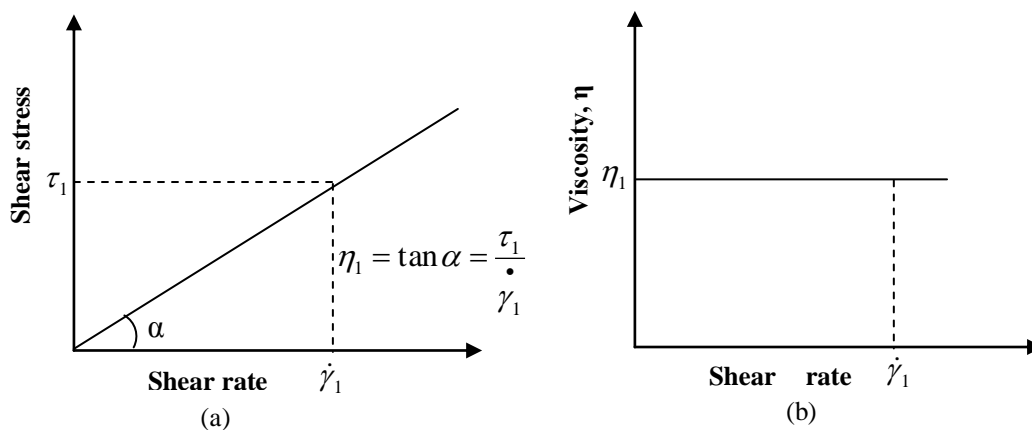


Figure. 5.3 (a) Flow curve and (b) viscosity curve of “Newtonian liquid” (Schramm, 2000).

Newton assumed that the graphical equipment of Equation 5.1 for an ideal liquid would be a straight line starting in Figure 5.3 flow curve and viscosity curve of “Newtonian liquid”. Origin of the flow curve would climb with a slope of an angle α as illustrated in Figure 5.3. Any point at this line defines pairs of values for τ and $\dot{\gamma}$.

Due to the fact that the flow curve for an ideal liquid is straight, the ratio of all pairs of τ and $\dot{\gamma}$ values belonging to this line is constant. This means that η is not affected by changes in shear rate. All liquids for which this statement is true are called “Newtonian liquids”. All other liquids not exhibiting this ideal flow behavior are called “non-Newtonian liquids” (Barnes, Hutton & Walters, 1989).

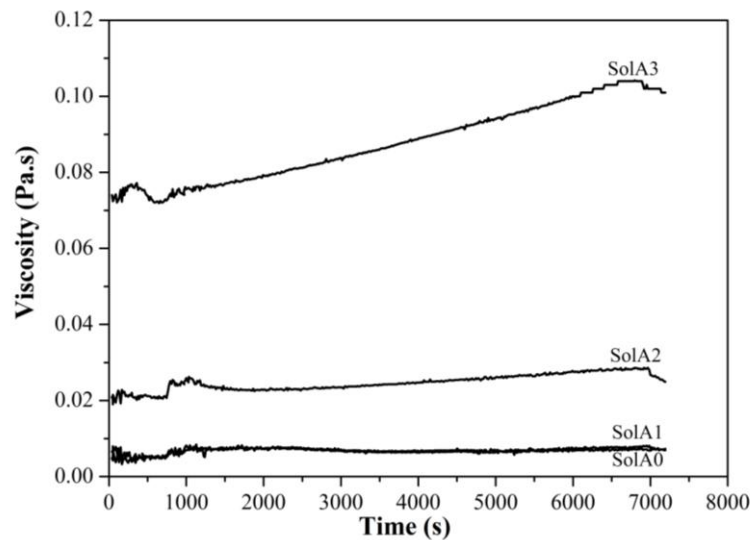
Shear profile of the prepared solutions was determined with rheological measurements under standard conditions of 25 °C, 2 hours with constantly increasing shear rates (1-1200 s⁻¹). Figure 5.4 (a) demonstrates viscosity of the solutions under increasing shear rate conditions. Generally for all solutions, viscosity value is low at slow shear rates but it increases and stays nearly constant with increasing shear rate. As seen in Figure 5.4 (a) viscosity values of SolA0 and SolA1 are roughly close to each other. Generally speaking, mean viscosity values of the solutions increase with increasing BZO concentration in the solution at room temperature. It was noted that the mean viscosity values are 7.8, 6.99, 24.72 and 87.49 mPa.s for solutions SolA0, SolA1, SolA2 and SolA3, respectively.

In order to determine the effect of temperature on viscosity characteristics of solution, measurements were performed at constant shear rate of 400 s⁻¹ and at increasing temperature from room temperature to 60 °C. As expressed by Barnes et al., the viscosity of Newtonian liquids decreases with increase in temperature, approximately according to the Arrhenius relationship:

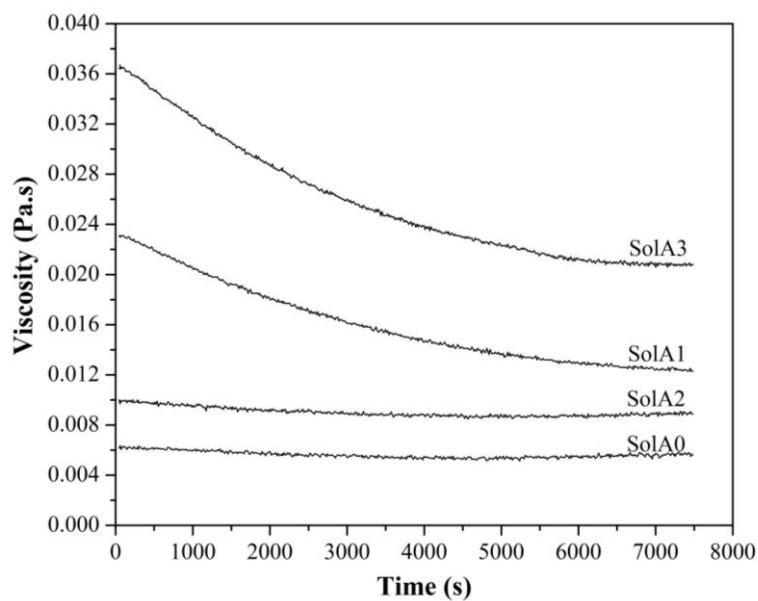
$$\eta = A \cdot e^{B/T} \quad (5.3)$$

where T is the absolute temperature and A and B are constants of the liquid. In general, for Newtonian liquids, the greater the viscosity, the stronger is the temperature dependence (Barnes et al., 1989). For the measurements performed under increasing temperature conditions, it is recognized that there is not an important variation at the viscosity values of SolA0 and SolA2, even though it decreases with increasing temperature for the SolA1 and SolA3. According to these

results, it is possible to say that viscosity is independent from the shear rate and stays constant with increasing values.



(a)



(b)

Figure 5.4 (a) Viscosity measurement of undoped and BZO doped solutions (a) at room temperature and increasing shear rate ($1-1200 \text{ s}^{-1}$) and (b) at increasing temperature and constant shear rate.

5.1.2 Preparation and Structural Characterization of YBCO Thin Films

All precursor solutions were dried at 100 °C for several hours until gelification occurred and xerogels formed, and subsequently DTA/TG analysis were performed under N₂ flow, as shown in Figure 5.5. Both the DTA and TG curves of doped samples are different from the undoped samples. The endothermic peak until 200 °C which represent the evaporation and release of acetic acid and water from gel network are deeper for undoped sample. Additionally, mass loss diagram of the undoped sample is composed of two steps whereas it is streight line for doped samples. Additional to DTA/TG analysis, FTIR analyses were performed to get insights into the chemical structure of solutions as shown in Figure 5.6. All samples exhibit similar spectra, stretching bands at 1650 cm⁻¹ is due to the COO⁻¹ group of TFA-YBCO samples. The small vibrations at wave number lower than 900 cm⁻¹ are due to the formation of M-O bonds.

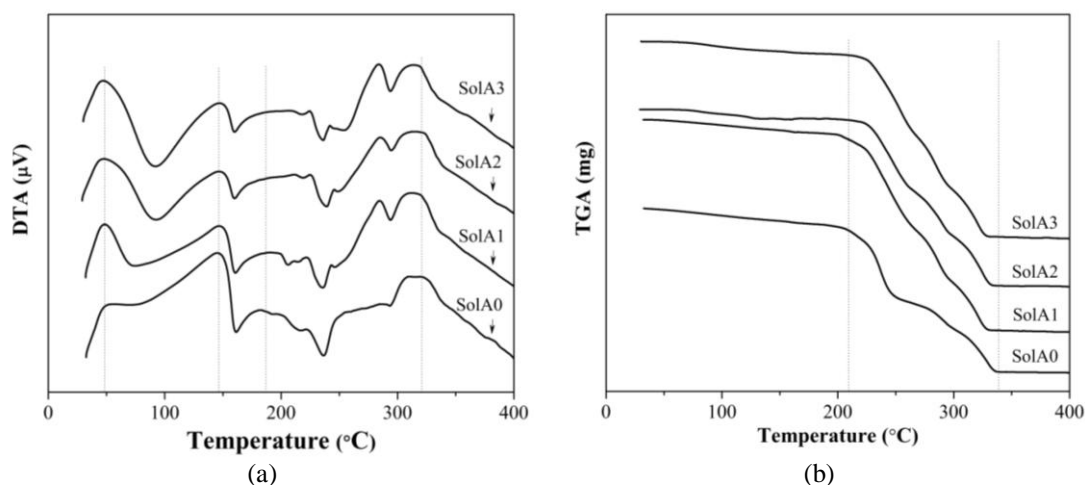


Figure 5.5 (a) DTA and (b) TGA curves of xerogels from YBCO precursor solution with 6, 12 and 18 mol % BZO concentration.

The (100) oriented SrTiO₃ (STO) single crystal materials with dimensions of 10x10x1 mm³ were used as substrates to prepare YBCO films by means of spin coating process. Film deposition on single crystal substrate was performed by spin coating technique at a rotation speed of 6000 rpm and acceleration speed of 6000 rpm s⁻¹ for 30 s.

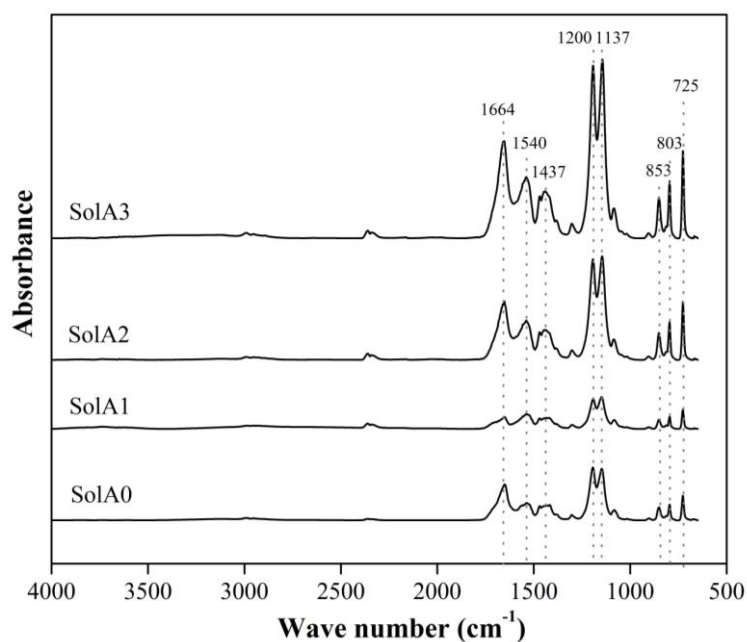


Figure 5.6 FTIR spectra of samples SolA0, SolA1, SolA2 and SolA3 samples.

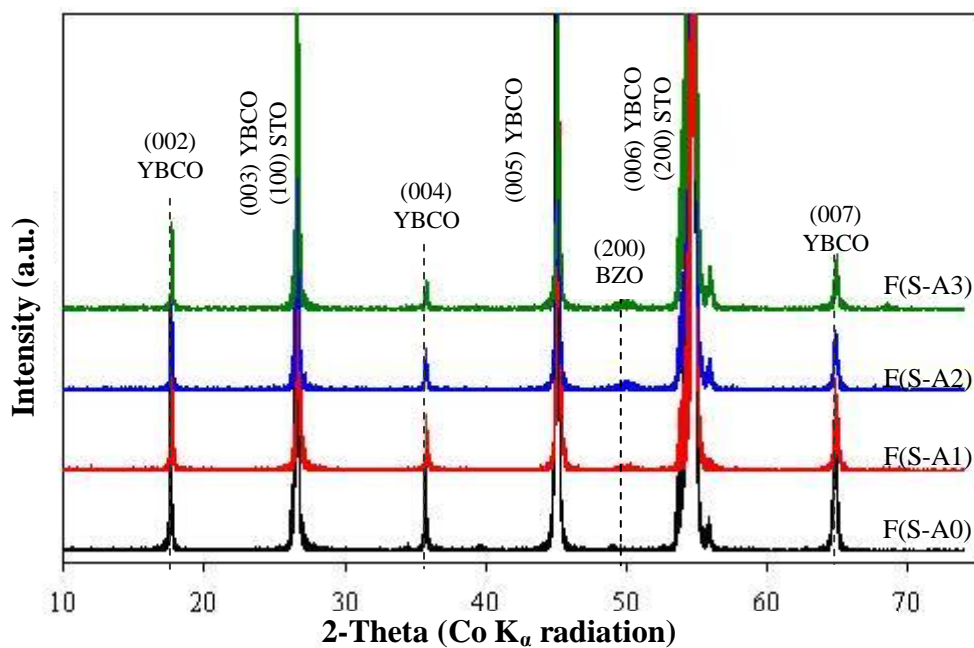


Figure 5.7 X-ray θ - 2θ scans of YBCO samples including F(S-A0), FS-A1), F(S-A2) and F(S-A3) with a $\text{Co K}\alpha$ radiation. (YBCO JCPDS card no: 040-0159, STO JCPDS card no: 035-0734).

In order to determine the structure and growth orientation of the films, X-ray diffraction (XRD) was performed on the YBCO films. Figure 5.7 presents the θ - 2θ

diffraction pattern of undoped and BZO doped YBCO films. Generally in these patterns, the major peaks correspond to the (00l) reflections of the YBCO phase and (100) STO substrate which indicates that the YBCO film has a strong c-axis texture. The structural integrity of the YBCO film can be easily affected by the doping process. Reduction in the (008) YBCO peak intensity with increasing BZO amount is evidence for this structural deterioration. A similar effect was found by Hänisch et al. (2006) with nanoscale precipitates of Hf, Zr and Ir dopants in YBCO films they reported that doping with the present elements affects the structural integrity of YBCO film strongly. Note that the peak intensities of (004) and (007) orientations of YBCO which have diffractions at 2θ of 35.8° and 65.10° respectively are lower than expected as a textured film structure. In addition, contrary to expectations, there is not a significant increase at the BZO peak intensity for different amounts of dopant concentration.

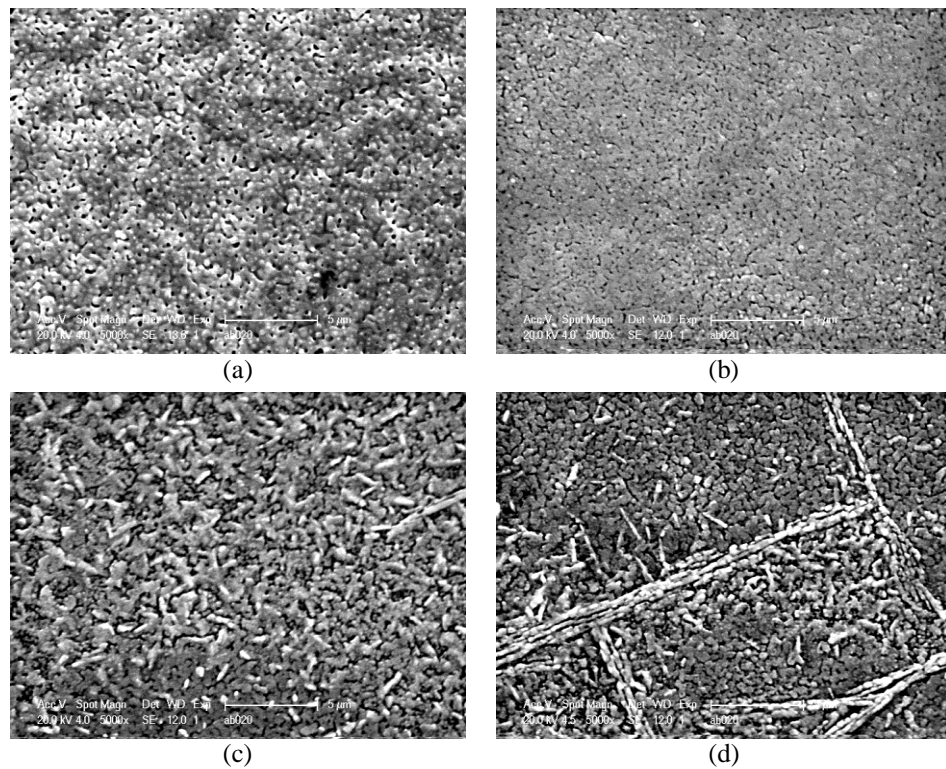


Figure 5.8 Surface morphologies of (a) F(S-A0), (b) F(S-A1), (c) F(S-A2) and (d) F(S-A3) films.

Figure 5.8 depicts surface morphologies of undoped and doped samples. These images clearly show that all films have a smooth, crack free surface and all of them are generally formed by c-axis oriented grains. It can be seen that, all surfaces are quite dense, but some of them have quite different micro-morphologies. Note that BZO doped YBCO films present a denser surface structure with decreasing porosity compared with the undoped YBCO films. On the other hand, 18 mol% BZO doped sample surface possesses bigger sized grains in comparison to the fine grains of 6 and 12 mol% BZO doped sample surfaces. Lots of needle-shaped a-axis growth exists on the surface of films. It can be noticed that some a-axis grains are easily identified due to their platelet-like shape.

5.1.3 Electrical Characterization of YBCO Thin Films

The dependence of inductively measured critical transition temperature (T_c) and transition width (ΔT_c) on the amount of BZO in the structure are plotted in Figures 5.9 and 5.10 (a). Generally speaking, sharp voltage-temperature and narrow phase shift-temperature curves represent high superconducting quality. It can be stated that, for the films prepared from SolA on STO substrates, the T_c value slightly decreases from 87.6 K to 86.5 K for F(S-A0), F(S-A1) and F(S-A2) but there is a sudden decrease for the F(S-A3) to 81 K.

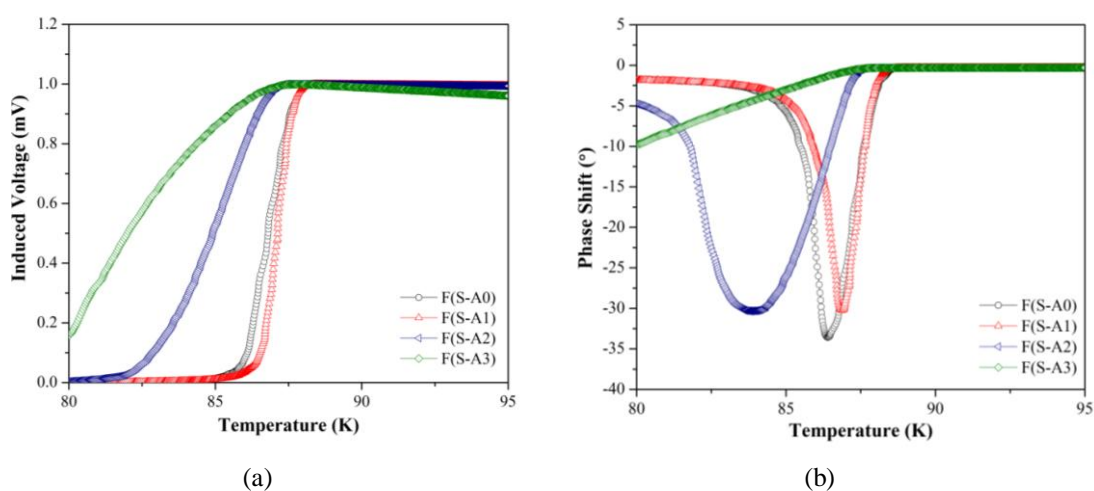


Figure 5.9 (a) Resistivity vs. temperature, (b) phase shift vs. temperature graphs of F(S-A0), F(S-A1), F(S-A2) and F(S-A3) films.

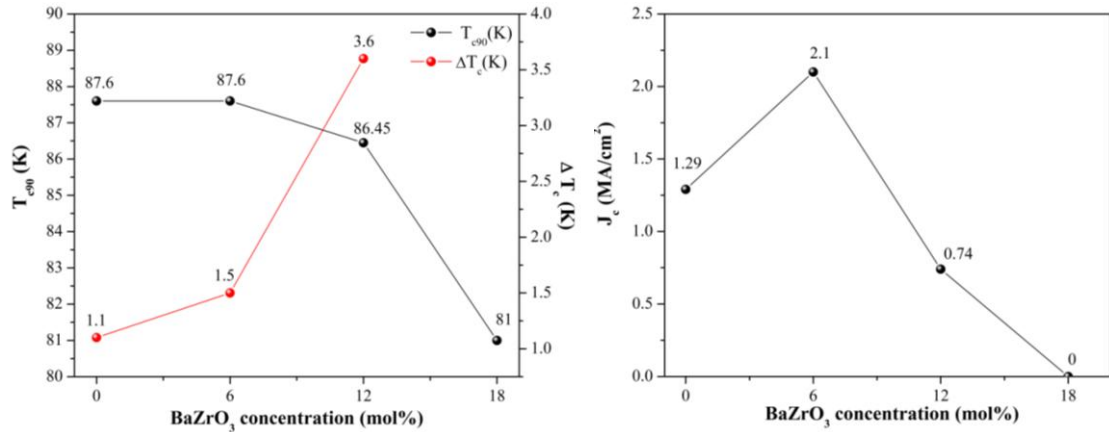


Figure 5.10 (a) Dependence of critical temperature T_c and transition width ΔT_c and (b) dependence of inductively measured critical current density J_c on the amount of BZO concentration.

Inductive measurements of the critical current density (J_c) at 77 K in self-field was performed for all samples and the results are given in Figure 5.10 (b). It is shown that the highest J_c for films prepared from SolA on STO substrates is 2.1 MA/cm² for 6% mol BZO doped YBCO film. The film with the highest BZO concentration does not have a superconducting characteristic anymore.

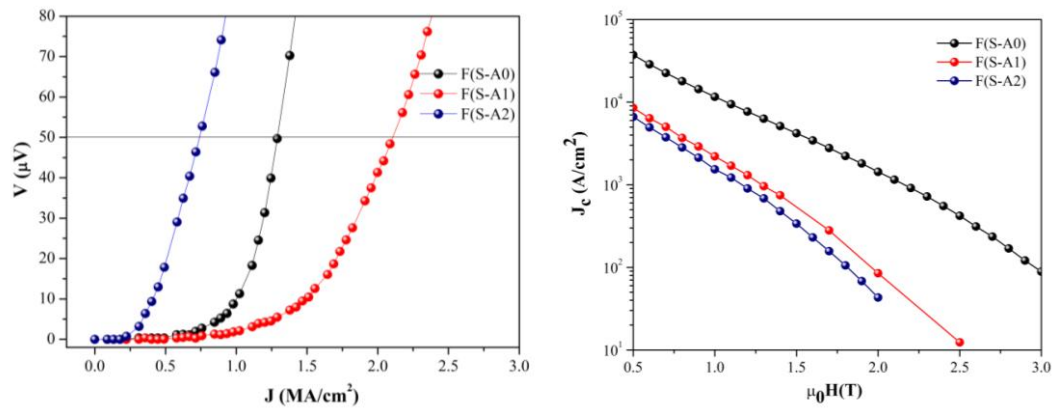


Figure 5.11 (a) Inductive critical current density (J_c) measurements of undoped and BZO doped YBCO films at 77 K in self-field and (b) field dependence of the critical current density at 77 K, up to 6 T.

As reported by Campbell, & Evetts (1972), the most accurate quantitative measurements of flux pinning are those of J_c as a function of field and temperature. Therefore, transport measurements were performed up to 6 T at 77 K in order to determine the magnetic field dependence of the critical current density as shown in

Figure 5.11. It can be seen that any of the BZO dopant concentration has not shown pinning effect in the structure. Besides, sample F(S-A3) does not exhibit superconducting behavior under any magnetic field condition.

5.2 YBCO Thin Film Production from Acetate Based Precursors

One of the most important issues in the MOD processing of YBCO coated conductor is the synthesis of MOD precursor solution. Growth mechanism and influence of processing parameters for TFA-MOD method have been widely investigated by many groups. Nevertheless, little attention has been paid to the effect of solvent used for precursor solution preparation. Generally methanol (CH_3OH) is used as a solvent in TFA-MOD process that may cause serious health risk during manufacturing process. It is a toxic material that may cause death or blindness. Wang et al. (2010) suggested ethanol ($\text{C}_2\text{H}_5\text{OH}$) as an alternative solvent for TFA-MOD method to reduce this health risks. They reported that the thin films prepared from ethanol-based precursor solution possess considerably high superconducting properties. However, a detailed comparison between methanol-based and ethanol-based precursor solutions is still required to understand solvent effect on the precursor film structure. Therefore, acetate-based precursor solutions were prepared with methanol and ethanol solvents separately and named as SolB and SolC.

As in detail explained in Part 5.1, the oxide powder of YBCO could not display good performance in the field of superconducting properties. In order to investigate the effect of propionic acid in the structure and properties of produced films, a third kind of solution was also prepared from acetate-based precursors with propionic acid. All solutions were compared according to their physical properties and tried to determine most compatible solution for thin film production with most rewarding superconducting properties.

5.2.1 Preparation and Characterization of Acetate-based Precursor Solutions

Three different kinds of precursor solutions were prepared from acetate-based precursors. The chemical components of all solutions are listed in Chapter 4 (see Table 4.2 for details). The flow chart of the solution preparation for SolB is illustrated in Figure 5.12. It was prepared by dissolving Y, Ba and Cu acetates into distilled water in a 1:2:3 cation ratio with arbitrary quantity of (~ 20 ml TFA for 50 ml final solution) TFA at room temperature. This aqueous solution was refined under vacuum atmosphere with evaporator in order to remove the solvent and to yield a glassy blue residue containing impurities of water and acetic acid. Later, the residue was dissolved in sufficient methanol and refined again to expel the impurities to yield a glassy blue residue containing methanol. After two cycles of refining processes, the resultant blue residue was dissolved in methanol to give a solution with a metallic ion concentration of 0.25 M. it can be pointed out that preparation of the SolC is quite similar to the SolB. The only difference is, instead of methanol, ethanol was used as a solvent.

The solution preparation process for SolD was illustrated with the help of the flow chart in Figure 5.13. Precursor powders of Y-ac, Ba-ac and Cu-ac were weighted out in a flask, propionic acid and TFA with a molar ration of 8:1 was added to dissolve powder. This mixture was stirred on a magnetic stirrer at 120 °C with low rpm until the solution completely dissolves. This solution was refined under vacuum atmosphere with evaporator in order to remove the solvent and to yield a glassy dark blue residue. After the formation of a dark blue, highly viscous state due to the evaporation, the TFA precursor was dissolved in acetone and propionic acid, which was added in a molar ratio of 3:1, and the final concentration was adjusted to a concentration of 0.25 M.

As a first step of solution characterization, contact angle values of each solution were measured with contact angle goniometer. All measurements were performed on STO and LAO substrates. Table 5.1 summarizes all measurement results. It is noticed that all contact angle values are changing from 19° to 26°.

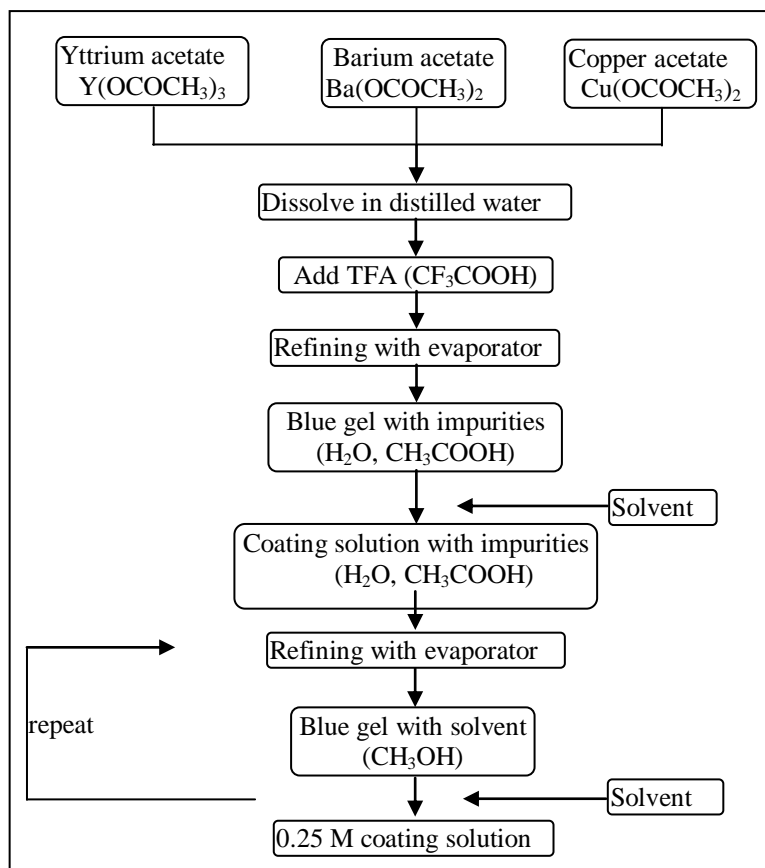


Figure 5.12 Schematic illustration of SolB and SolC preparation.

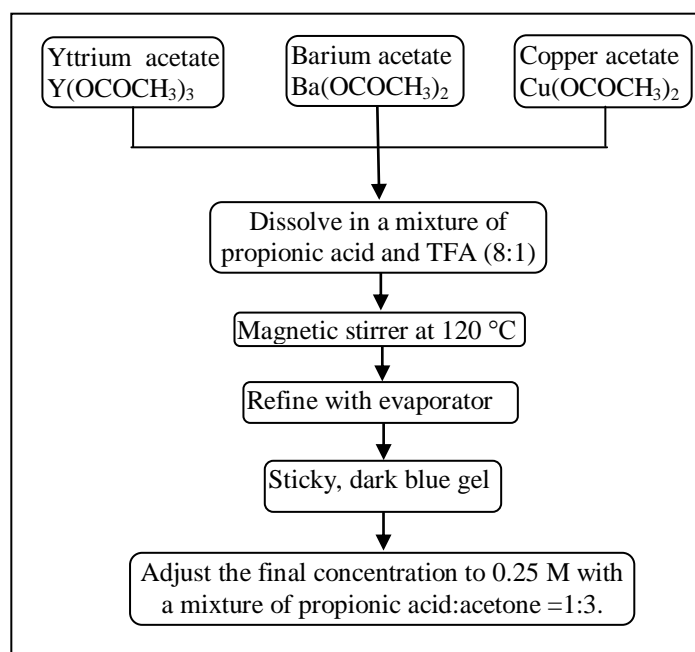


Figure 5.13 Schematic illustration of SolD preparation.

All type of solutions exhibit higher contact angle values on LAO substrates and additionally, SolD0 has the highest contact angle values on both substrates.

Table 5.1 Contact angle values of SolB0, SolC0 and SolD0 on STO and LAO substrates.

Sols	Contact angle value (°) on;	
	STO substrate	LAO substrate
SolB0	21.28	22.05
SolC0	19.24	25.43
SolD0	22.18	26.21

Viscosity measurements of precursor solutions were performed to control their stability. According to Cavallaro, once new chemical bonds forms or some precipitates appear due to aging phenomena in a solution, it is associated to a change of the viscosity of the solution with time. Additionally, control of the viscosity is also a good way to control the thickness of the deposited film; an increase of the viscosity corresponds to an increase in thickness. (Cavallaro, 2005).

We first studied the stability of viscosity with time as shown in Figure 5.13 (a). Rheological measurements were performed under standard conditions of 25 °C, 2 hours with constantly increasing shear rates (1-1200 s⁻¹). It is clear that the mean viscosity values are 4.21, 5.74 and 8.92 mPa.s for SolB0, SolC0 and SolD0, respectively. The viscosity value is correlated to the intrinsic nature of solvent. The viscosity values of methanol, ethanol and propionic acid at 25 °C are 0.59, 1.20 and 1.1 mPa.s, respectively. These data are compatible and have the same trend as viscosity measurement results of solutions. Due to the higher viscosity value of ethanol in comparison to methanol, SolC0 has higher viscosity value at room temperature. The highest viscosity value of SolD0 is due to the higher percentage of propionic acid to the TFA in the solution in comparison to the other solutions. In general, time-dependent variation of solution viscosity is negligible which indicates excellent stability of all precursor solutions.

Additional to the time dependence of viscosity under increasing shear rate conditions, the effect of temperature on viscosity at constant shear rate (400 s⁻¹) is also analyzed in this chapter. Figure 5.13 (b) signifies the dependence of viscosity to

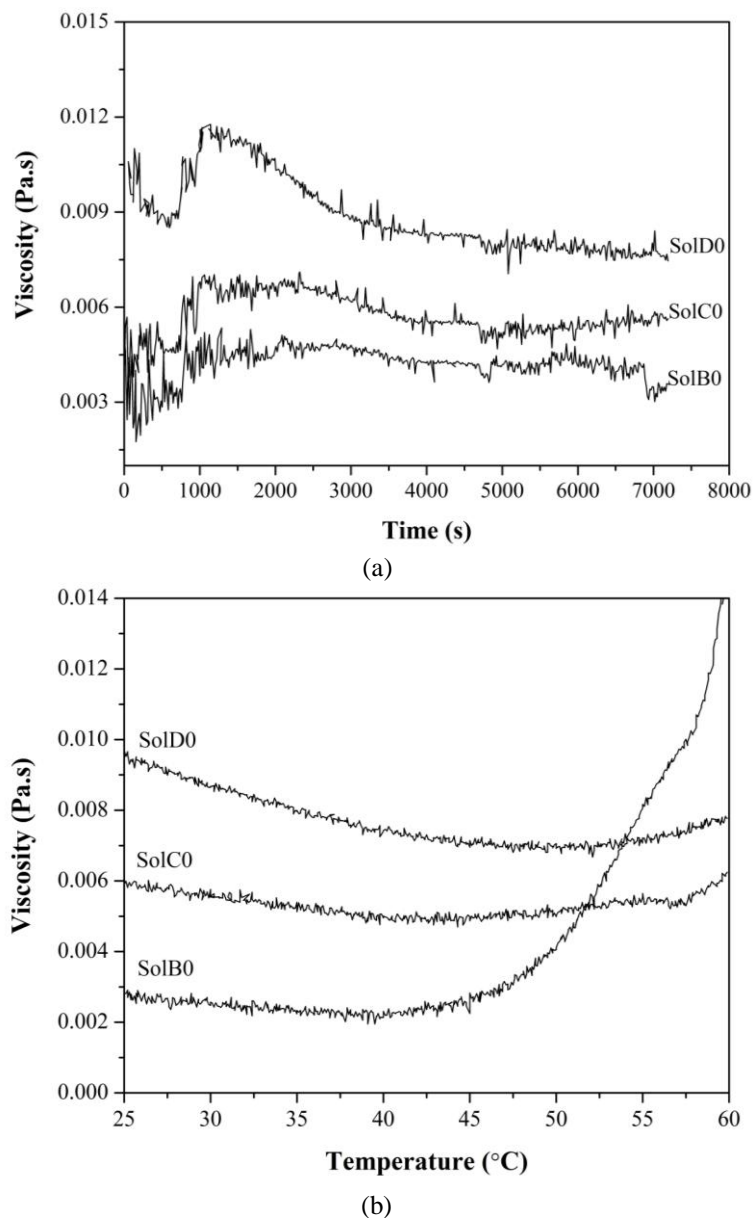


Figure 5.13 Viscosity measurements of methanol-based (SolB0), ethanol-based (SolC0) and propionic acid-based (SolD0) solutions prepared from acetate precursors (a) at 25 °C and (b) at increasing temperature conditions (25 °C-60 °C).

increasing temperature from 25 °C to 60 °C. SolB0 exhibits an abrupt viscosity increase after 45 °C. It is possible to explain this behavior with the lower boiling point of methanol (65 °C) in comparison to the higher boiling points of ethanol (78.3 °C) and propionic acid (141 °C). Evaporation of methanol from the solution causes this increase at the viscosity value. Similar effect was also explained by Jin et

al. they reported that proper selection and addition of a high boiling point solvent can prevent films from roughening during precursor pyrolysis (Jin, 2010).

FTIR analyses were performed to get insights into the chemical structure of solutions as shown in Figure 5.14. Methanol and ethanol-based solutions exhibit similar spectra, band at high frequencies owing to the O-H stretch from water. SolD0 has smoother spectra at that region due to lack of water in the solution. Stretching bands at 1650 cm^{-1} is due to the COO^{-1} group of TFA-YBCO samples. The small vibrations at wave number lower than 900 cm^{-1} are due to the formation of M-O bonds.

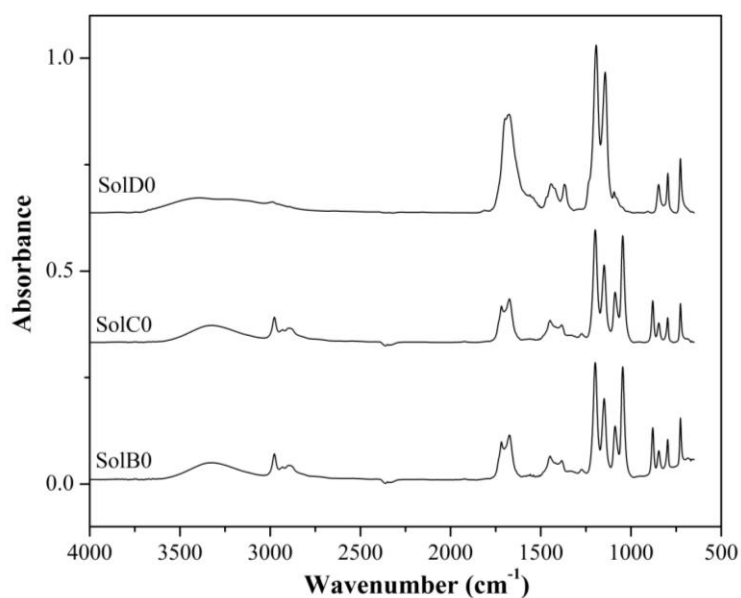


Figure 5.14 FTIR spectra of samples SolB0, SolC0 and SolD0.

All precursor solutions were dried at $100\text{ }^{\circ}\text{C}$ for several hours until gelification occurred and xerogels formed, and subsequently DTA/TG analysis were performed under N_2 flow, as shown in Figure 5.15. The two endothermic peaks until $200\text{ }^{\circ}\text{C}$ represent the evaporation and release of acetic acid and water from gel network. It is evident from the figure that the reactions between $200\text{ }^{\circ}\text{C}$ and $330\text{ }^{\circ}\text{C}$ are coupled to combustion reactions in terms of the presence of acetate groups and loss of TFA. For methanol and ethanol-based samples, these reactions eventuate within a narrow temperature interval, whereas in propionic acid-based sample that takes place in a

broad temperature interval. The same behavior is also observable at the mass loss diagrams. There is a linear mass decrease for dried gel of SolD0.

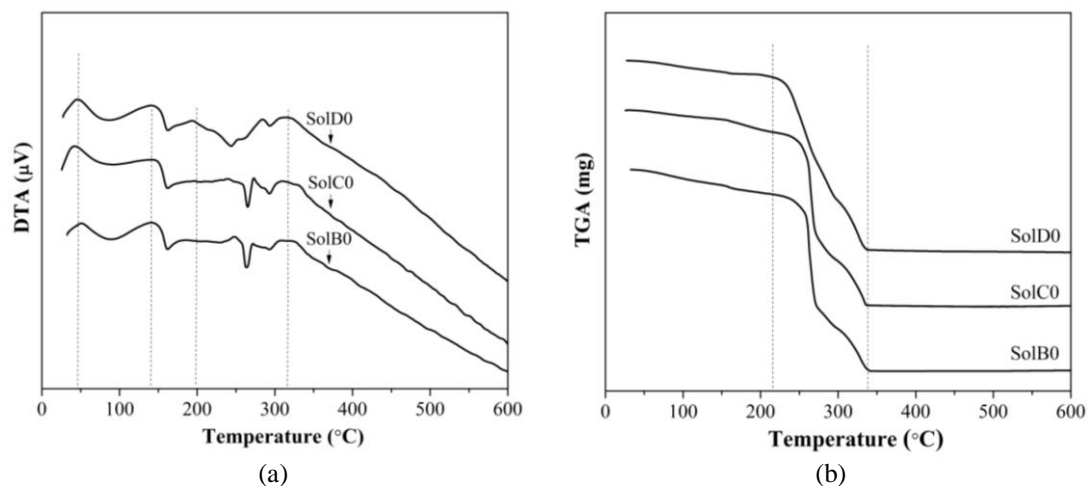


Figure 5.15 (a) DTA and (b) TGA curves of xerogels prepared from SolB0, SolC0 and SolD0.

5.2.2 Detailed Heat Treatment and Process Route Investigation of Superconducting YBCO Thin Film Production

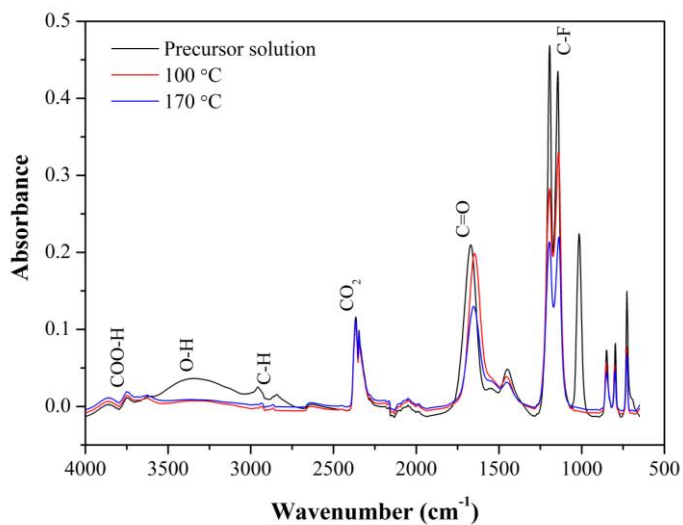
Coated samples were heat treated according to the profile denoted in Figure 4.5. During the heat treatment process, dry gas treatment up to 60 °C prevents the gel film from absorbing humidity that would deteriorate film integrity. Above 60 °C, humidified O₂ is introduced to suppress the sublimation of Cu trifluoroacetate which takes place due to its small molecular weight (298.58 gr/mol), as compared to Ba(TFA)₂ and Y(TFA)₃ (367.37 and 427.95 gr/mol respectively) (Petrisor, & Ciontea, 2006). Metal trifluoroacetates decompose and harmful gaseous residues are removed during the pyrolysis to give a precursor film. The primary interest of the TFA-MOD process is that the pyrolysis process leads to homogeneous mixtures of nanometric oxide and fluoride phases which can be then easily converted to crystallized YBCO films at relatively low temperatures. This is only possible because the TFA precursors form BaF₂ avoiding the formation of BaCO₃ phase which is stable up to 1000 °C and can impurify the YBCO phase, whilst BaF₂ can be decomposed in a humid atmosphere at temperatures as low as 600 °C (Puig et al., 2005). Additionally, the thermal decomposition of TFA precursor films result in a reduction of film thickness of the order of 50% and is accompanied by an increase of

stress within the film. Therefore, precursor film is susceptible to crack formation at decomposition temperatures. In order to mitigate crack formation in the precursor film during pyrolysis step, it is necessary to adjust a slowly increasing heating ramp. After the pyrolysis step, the fluoride containing precursor film is fired at a maximum temperature of 780 °C under humidified N₂ mixed with 100 ppm O₂ and then oxygenated at 450 °C to obtain the YBCO superconducting film.

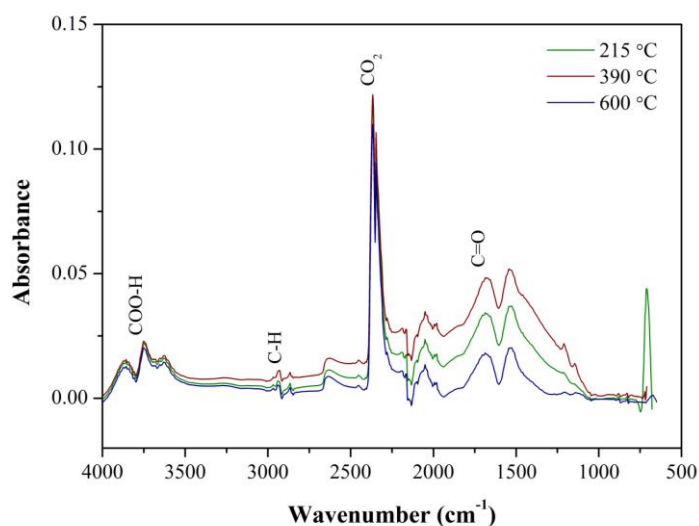
It is necessary to determine the sequence of chemical reactions occurring in the complex chemical solution deposition system to further the development of processing route and optimize critical current of conductor. (Thuy, Hoste, Herman, Buysser, & Driessche, 2009; Finlayson, Mouganie, Cordero-Cabrera, & Glowacki, 2007). This investigation uses FTIR characterization technique to determine the chemical ingredient of samples quenched at different temperatures throughout the heat treatment. The infrared spectra were recorded with ATR apparatus in the spectra range between 4000 and 650 cm⁻¹ with a resolution of 4 cm⁻¹.

Samples were quenched at different points of heat treatment, when the temperature had reached 100, 170, 215, 390 and 800 °C, respectively. All temperatures were selected as critical points of pyrolysis and crystallization steps. The spectra of the precursor solution were also taken to compare with the quenched samples. FTIR spectra of samples during the heat treatment are shown in Figure 5.16. In Figure 5.16 (a), from precursor solution to 215 °C, absorption bands of C=O and C-F vibrations correspond to the trifluoroacetic acid. Note also that the band at high frequency (3340 cm⁻¹) due to the O-H stretch from water became smaller as the temperature increases. Bands at 2365-2345 cm⁻¹ belong to carbon dioxide from atmosphere and decomposition of the gel during heat treatment.

Acetate complexes started to decompose at temperatures higher than 170 °C indicated by a change in intensity and to lower wave numbers. The small vibrations at wave number lower than 1100 cm⁻¹ are by virtue of the formation of M-O bonds. It is obviously clear that the bands due to organic compounds lowered in intensity and disappeared almost completely at 390 °C.



(a)



(b)

Figure 5.16 FTIR spectra of (a) precursor solution and samples quenched at 100 °C, 170 °C (b) 215 °C, 390 °C and 600 °C.

In addition to FTIR characterization, the decomposition of the gel was also studied under N_2 flowing in order to obtain information about the decomposition behavior of the gels to adjust the thermal treatment accordingly.

DTA-TGA analysis allows identifying at which temperatures the endothermic drying process and the exothermic pyrolysis process occur. The decomposition reaction of metal-trifluoroacetates can be summarized according to the equation below (Llordes et al., 2010):



Early works (Araki, & Hirabayashi, 2003) suggested that TFA precursors for YBCO growth decompose within the 200-250 °C range. However, more recent works have shown that the TFA precursors decompose mainly in the range of 250-300 °C. Hence it is necessary to investigate all the solution and film transformation processes occurring from room temperature up to the completion of the pyrolysis to understand the formation of epitaxial YBCO films (Roma et al., 2006).

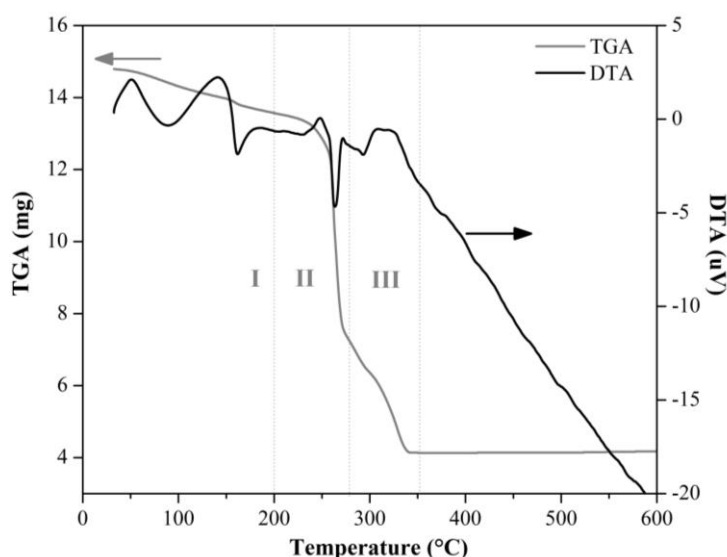


Figure 5.17 DTA-TGA spectrum of YBCO xerogel.

Three main areas can be distinguished in the thermogram, as is evident from Figure 5.17. The first broad endothermic peak can be correlated to the evaporation and release of acetic acid and gel network water just below 200 °C. It can be stated that the exothermic peak at 233 °C coupled to the large loss in mass can be attributed to an auto combustion reaction due to the presence of acetate groups and loss of TFA, in addition to the initial formation of BaF₂ and CuO phases. The other exothermic peak at 275 °C is thought to be associated with the formation of a yttrium intermediate as Y₂O₃. The final combustion of the network mainly involves the release of a relatively large quantity of CO and CO₂. After this reaction the remaining

species consist of yttrium, barium and copper oxides. These metal oxides then convert to the desired YBCO phase at the sintering temperature of ~ 800 °C. There is not anymore weight loss after ~ 350 °C, which is explained by Petrisor et al., (2006) that the stable fluorides are formed from the dried gel and are not converted to oxyfluorides afterwards.

5.2.3 Structural Properties of YBCO Thin Films Prepared from Methanol-, Ethanol- and Propionic acid-Based Solutions with BZO Pinning Centers

All solutions were prepared from Zr concentrations adjusted to 0, 6, 12 and 18 mol% Zr regarding to stoichiometric precursors. (100) oriented STO and LAO single crystal materials with dimensions of $10 \times 10 \times 1$ mm³ were used as substrates and spin coated samples were heat treated according to the previously determined heat treatment profile.

The overall structure of the YBCO thin films were assessed with the help of X-ray diffraction with Co K_α radiation. Data from each sample with different amount of BZO concentration were plotted together for different kinds of solutions and substrates as shown in Figures 5.18-5.23.

Generally, in all XRD patterns of samples, strong (00l) peaks of YBCO indicate that films have a large fraction of c-axis oriented grains with regard to the substrates. It is also possible to observe the (h00) reflections coming from STO or LAO single crystal substrates. Additionally, it can be inferred from the XRD patterns that the BZO (200) peaks are very weak compared with the YBCO (00l) peaks and peak intensities increases slightly with increasing BZO concentration.

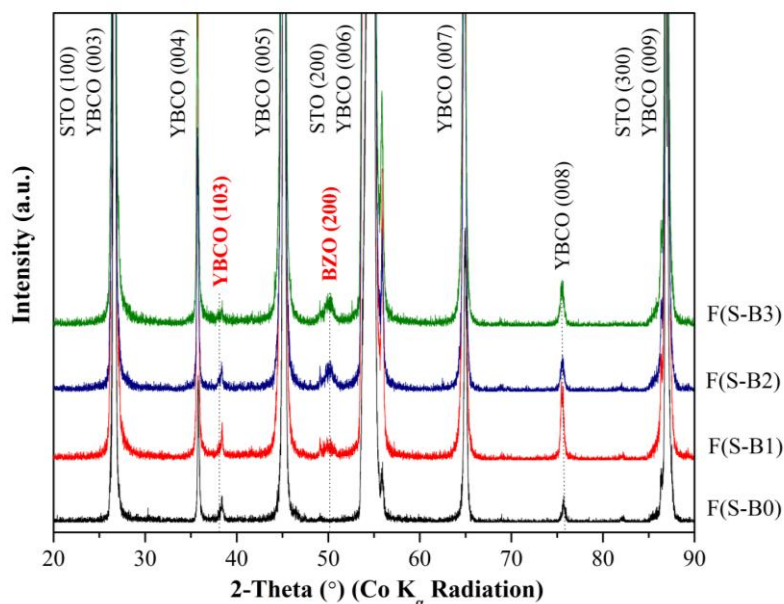


Figure 5.18 X-ray θ - 2θ scans of F(S-B0), F(S-B1), F(S-B2) and F(S-B3) films with a Co K_{α} radiation.

The intensity of YBCO peaks are important factor that presents information about the crystallinity. Gonzales (2005) denoted that increasing values of YBCO (005) reflection is an evidence of crystalline structure enhancement. In our measurements, (008) YBCO peak intensity changes for different samples. In addition, (103) orientation of YBCO phase displays a dopant concentration dependent trend. In the case of films prepared from SolB on STO and LAO substrates (F(S-B) and F(L-B) series), (103) orientation of YBCO is observable for all dopant concentrations as well as undoped samples and decreases with increasing BZO amount. This orientation is not distinguishable in F(S-C) series, whereas in F(L-C) series has weak intensity for all samples. Finally the textured structure of F(S-D0) deteriorates with increasing BZO concentration and (103) YBCO orientation becomes observable. Additional to different orientation of YBCO, there are also some impurity phases as Y_2O_3 and $BaCO_3$ in the structures of F(L-B) and F(L-C) series of samples. These kinds of unwanted phases may affect the textured structure of films.

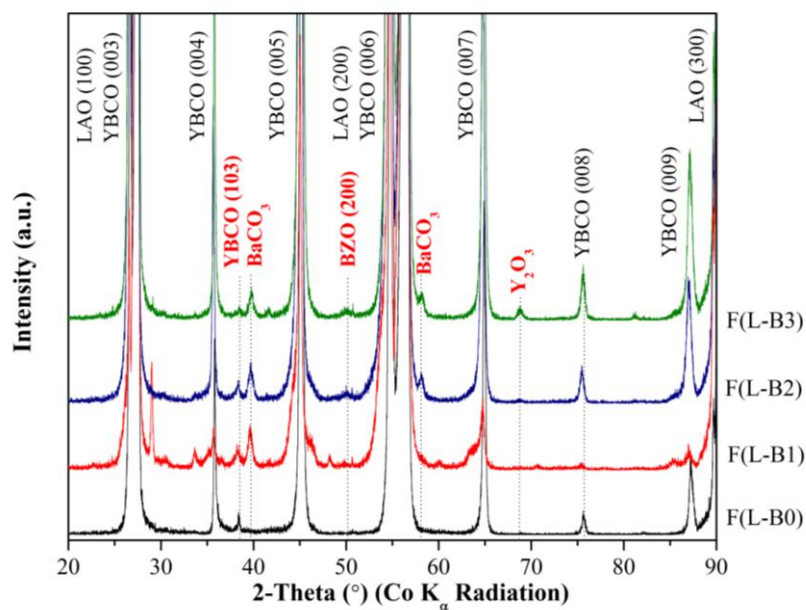


Figure 5.19 X-ray θ - 2θ scans of F(L-B0), F(L-B1), F(L-B2) and F(L-B3) films with a Co K_{α} radiation (LAO JCPDS card no: 031-0022, Y_2O_3 JCPDS card no: 01-074-1828, $BaCO_3$ JCPDS card no: 041-0373).

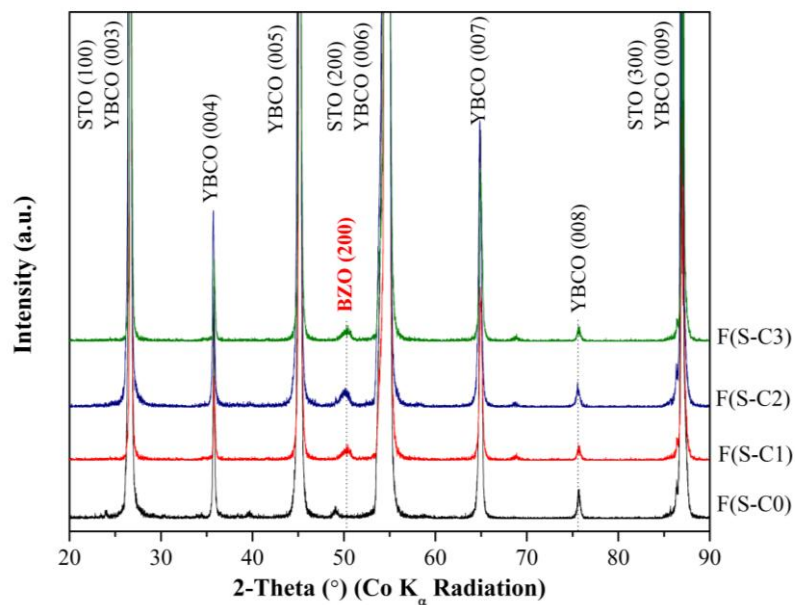


Figure 5.20 X-ray θ - 2θ scans of F(S-C0), F(S-C1), F(S-C2) and F(S-C3) films with a Co K_{α} radiation.

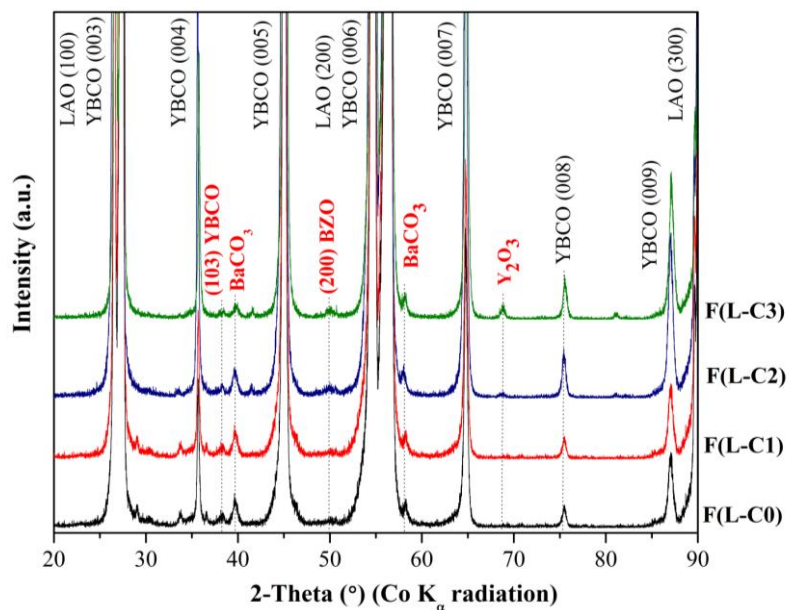


Figure 5.21 X-ray θ - 2θ scans of F(L-C0), F(L-C1), F(L-C2) and F(L-C3) films with a Co K_{α} radiation.

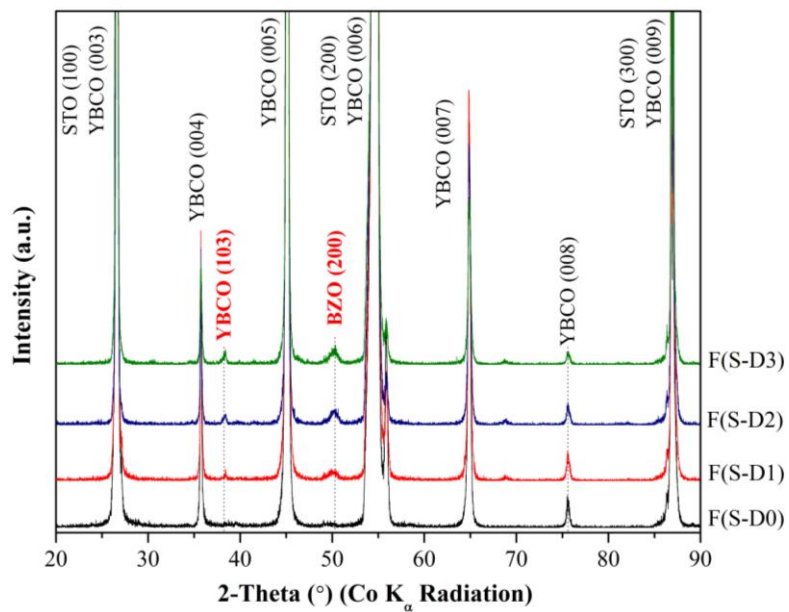


Figure 5.22 X-ray θ - 2θ scans of F(S-D0), F(S-D1), F(S-D2) and F(S-D3) films with a Co K_{α} radiation.

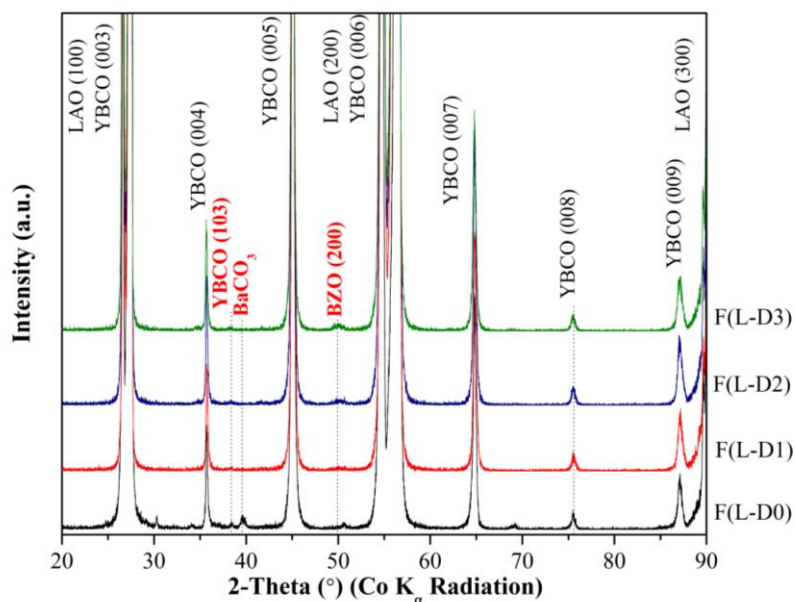


Figure 5.23 X-ray θ - 2θ scans of F(L-D0), F(L-D1), F(L-D2) and F(L-D3) films with a Co K_{α} radiation.

As specified in detail, YBCO ceramic oxide is an anisotropic compound and thus it is very important to obtain completely textured, c-axis oriented grains perpendicular to the substrate surface. Otherwise, a misorientation produces a detrimental of superconducting performances. Hence, texture measurements were also performed parallel to phase analysis as shown in Figures 5.24-5.27. Due to the impurity content of B and C series of samples, texture measurements were only applied to the F(S-D3) and F(L-D3) films which include the highest dopant concentrations.

In the (102) pole figures of both films, the presence of only one sharp peak with fourfold symmetry confirms the epitaxial growth of YBCO films on to the STO and LAO substrates. (110) pole figure reflections of BZO phase on STO and LAO substrates explain us that BZO nanoparticles are randomly oriented and distributed within the YBCO matrix. It is predicted by Gutierrez et al., (2007) that the random crystalline orientation of artificial pinning centers in the matrix is the essential feature distinguishing chemically prepared nanocomposite films from those prepared through vacuum deposition methods.

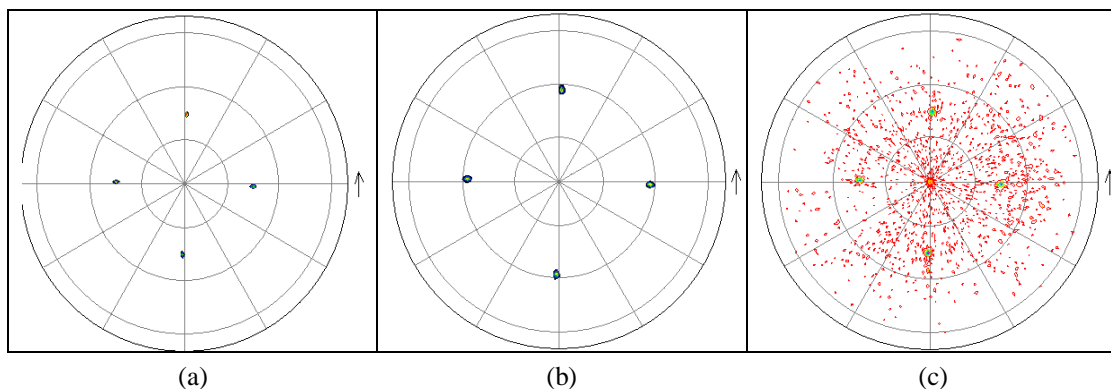


Figure 5.24 X-ray pole figure of (a) (110) reflection of STO, (b) (102) reflection of YBCO and (c) (110) reflection of BZO for F(S-D3) film.

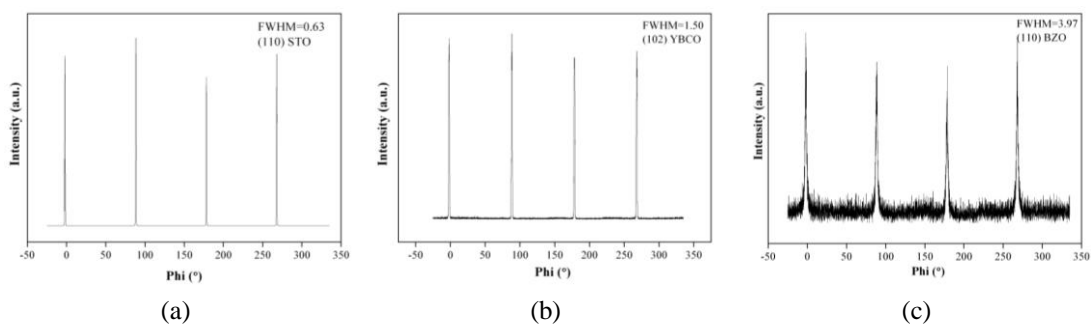


Figure 5.25 Φ -scans of (a) (110) STO, (b) (102) YBCO and (c) (110) BZO for F(S-D3) film.

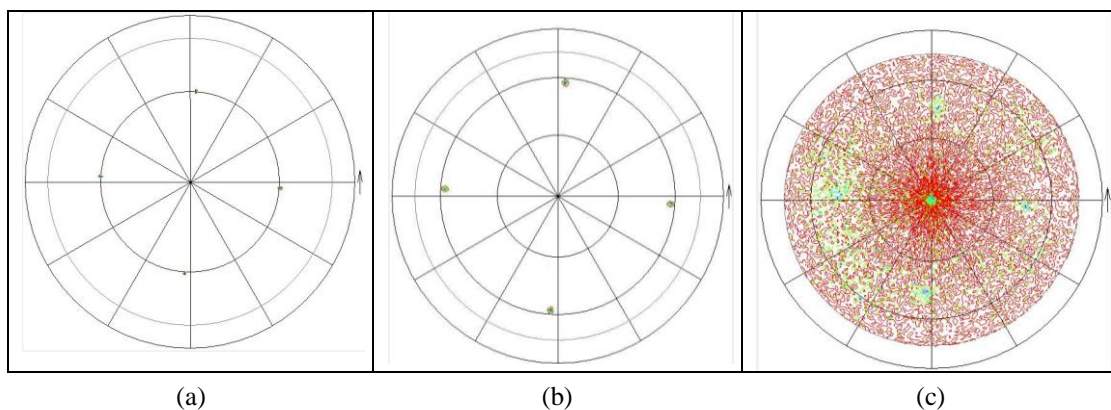


Figure 5.26 X-ray pole figure of (a) (110) reflection of LAO, (b) (102) reflection of YBCO and (c) (110) reflection of BZO.

The FWHM values of phi scans for (102) reflections of YBCO are 1.50 and 1.94 for F(S-D3) and F(L-D3) films, respectively. These values confirm the good degree of epitaxial growth of YBCO films on STO and LAO substrates.

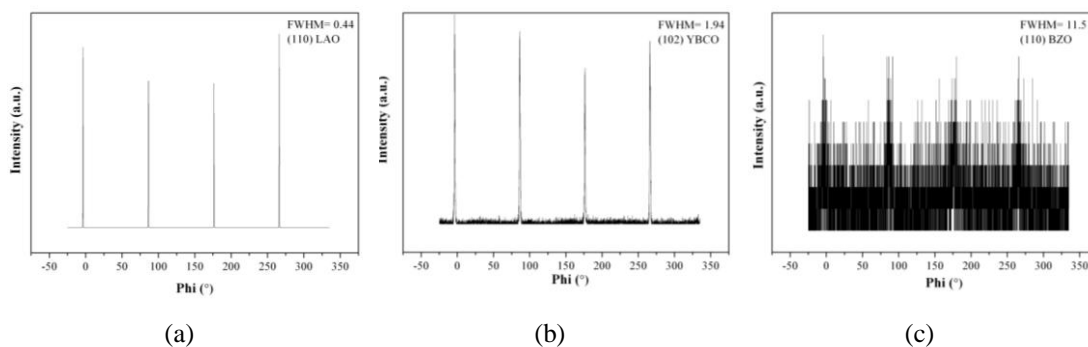


Figure 5.27 Φ -scans of (a) (110) LAO, (b) (102) YBCO and (c) (110) BZO.

The surface morphologies of all samples generally exhibit continuous and flat surfaces with the characteristic porosity and outgrowths of the c-axis growth as depicted in Figures 5.29, 5.30, 5.32, 5.33, 5.36 and 5.37. In addition, the presence of some a-axis oriented grains is denoted by needle-shape grains with average size of 1-2 μm . As can be clearly shown in Figures 5.29 and 5.30, in all samples of F(S-B) series and undoped sample of F(L-B) series, a high percentage of a-axis growth is observable. It can be noticed that the a-axis grain size is increasing with BZO concentration in the structure for F(S-B) series samples. Similar a-axis grown micro morphologies on STO substrates were also observed by Zhao, Lei, Liu, & Chen, (2008).

Feenstra, Lindemer, Bundai, & Galloway (1991) explained that in almost c-axis oriented and dense films, the c-axis growth model is performed by islands. This is a typical growth mode of c-axis grains for MOD process and causes the formation of small pores trapped within c-axis grains. Gonzales (2005) modeled this growth as depicted schematically in Figure 5.28. In this case, the growth rate in the a/b-direction is much faster than along the c-direction. It can be stated that, when an a/b-axis grain nucleates it takes as much material as possible from the surrounding areas in order to increase its length perpendicular to the substrate. As a result there is a lack of material for the neighbouring c-axis grains to fill the gap between a/b-axis nucleation centers and pores are thus formed (Suenaga, 2002).

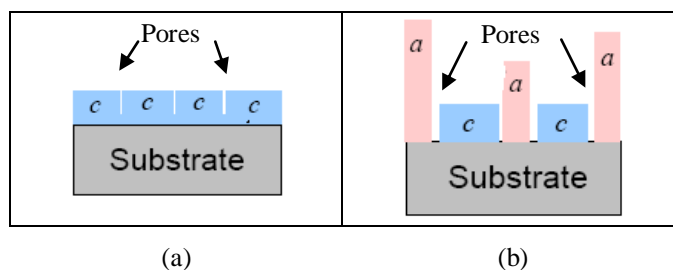


Figure 5.28 Scheme of porous formation in (a) fully c-axis oriented and (b) almost a-axis oriented film (Gonzales, 2005).

Due to the intrinsic nature of chemically deposited compounds there exists a tendency to generate porous films. Nonetheless, non-optimised growth conditions may lead to very porous structure which can strongly degrade the current carrying capability of films (Castano et al., 2003a, 2003b). In our samples, broadly speaking BZO doped YBCO films present a denser surface structure with decreasing porosity compared with the undoped YBCO films. F(L-D3) is the only exception which has a larger grain size with higher porosity concentration. It is possible to detect the influence of through measurements of T_c and J_c . A pore behaves like an obstacle for current transport thus presence of porosity results in poor connectivity of YBCO grains and giving low T_c and J_c values.

The surface morphologies of samples are additionally characterized by AFM in order to determine film thicknesses and roughness values of superconducting thin films. The average surface roughness (S_a) of the films were determined in a scan area of $20\ \mu\text{m} \times 20\ \mu\text{m}$. All S_a values and film thicknesses are listed in Table 5.2. AFM scans of undoped and 18 mol% BZO doped samples for each series are shown in Figures 5.31, 5.34 and 5.37. The a-axis grain oriented grain structure of 18 mol% BZO doped sample on STO substrate is more discernible in the AFM image. Except that, all surfaces are smooth, continuous and homogeneous. All film thickness values are in the range of 220-270 nm and for all series of samples, doped samples have higher film thickness values because of BZO contribution.

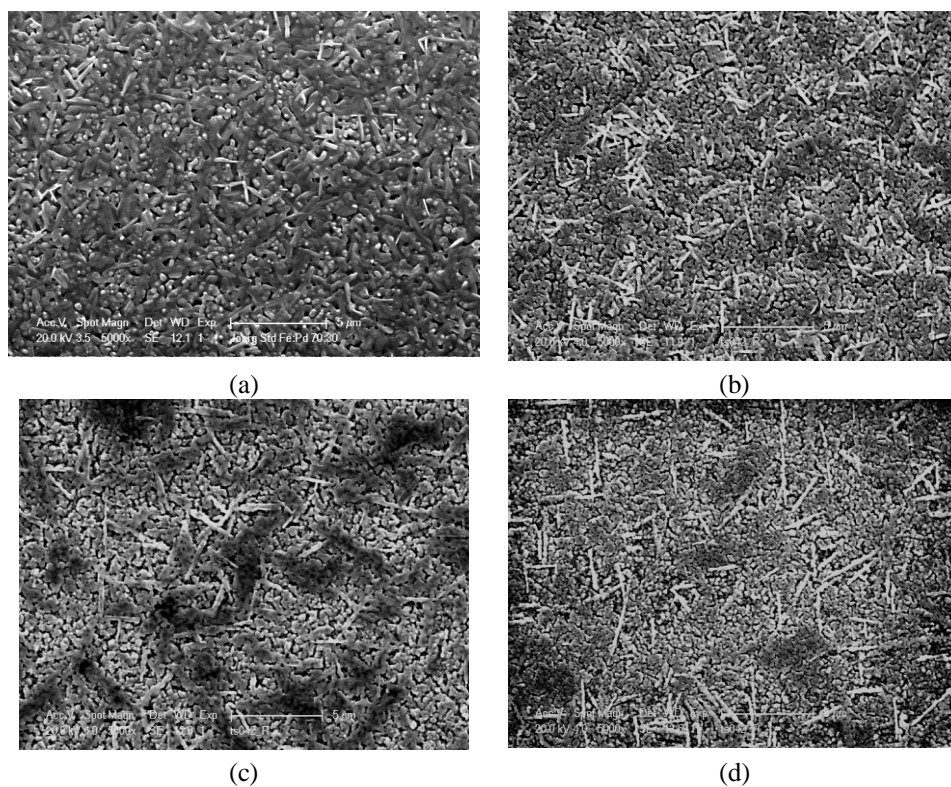


Figure 5.29 Surface morphologies of (a) F(S-B0), (b) F(S-B1), (c) F(S-B2) and (d) F(S-B3) films.

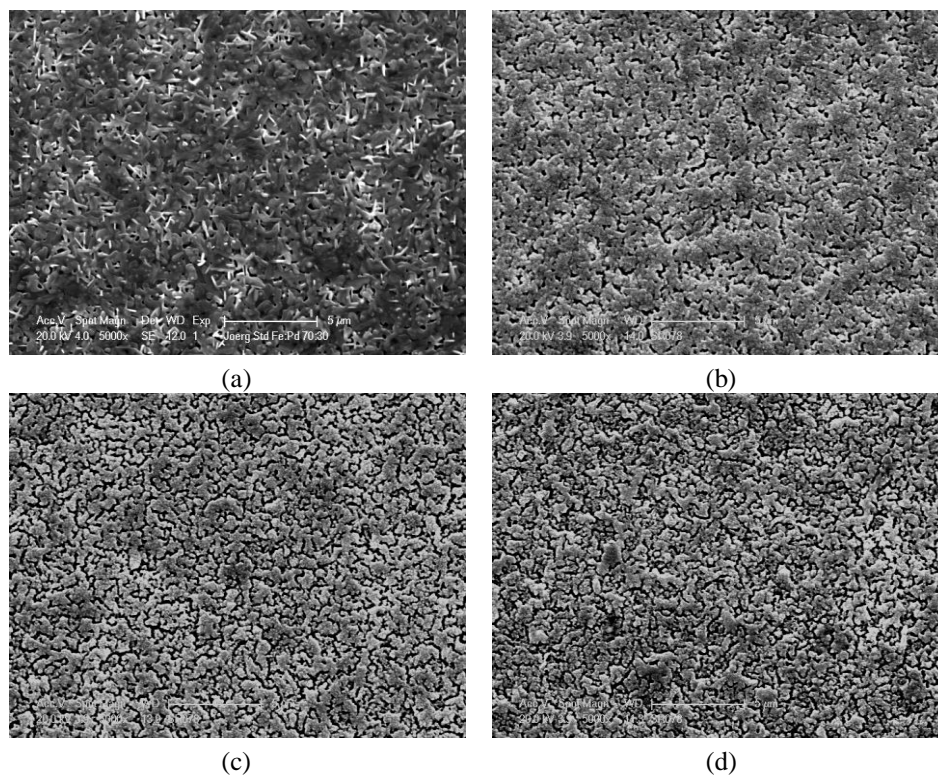


Figure 5.30 Surface morphologies of (a) F(L-B0), (b) F(L-B1), (c) F(L-B2) and (d) F(L-B3) films.

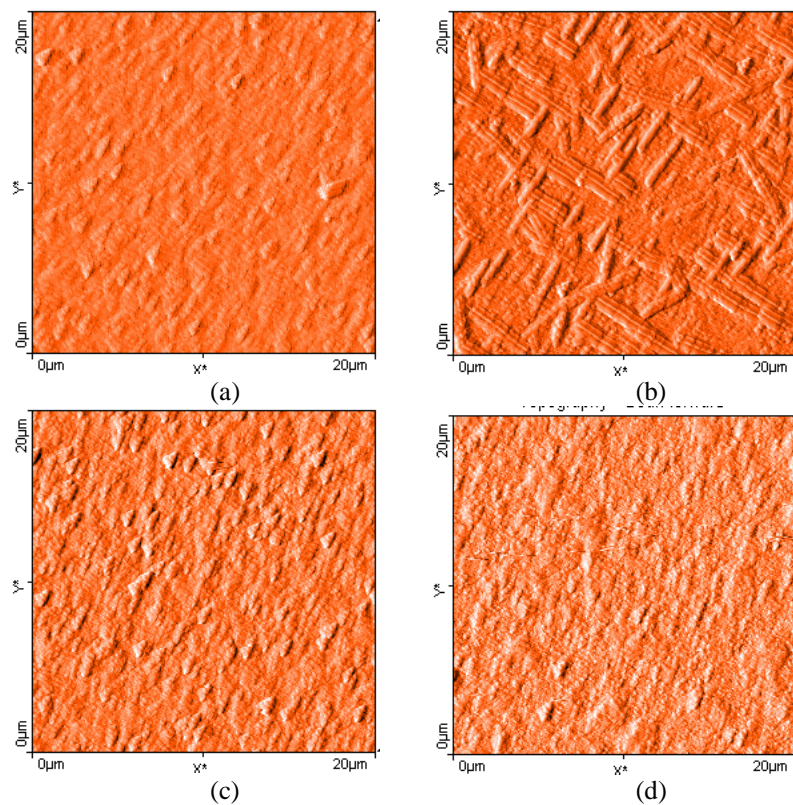


Figure 5.31 AFM images of (a) F(S-B0), (b) F(S-B3), (c) F(L-B0) and (d) F(L-B3) films.

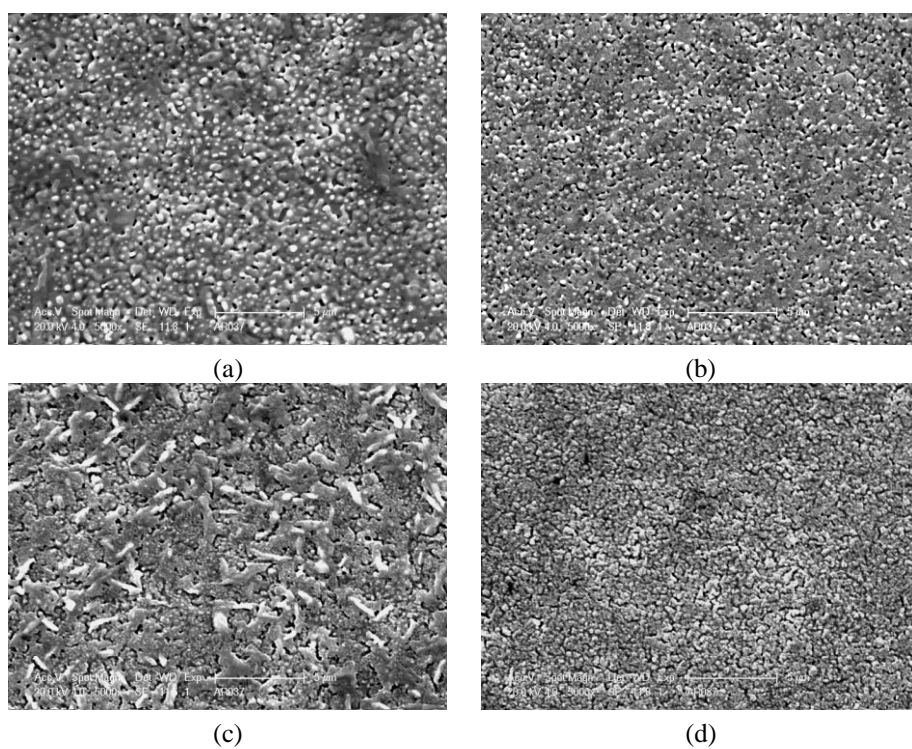


Figure 5.32 Surface morphologies of (a) F(S-C0), (b) F(S-C1), (c) F(S-C2) and (d) F(S-C3) films.

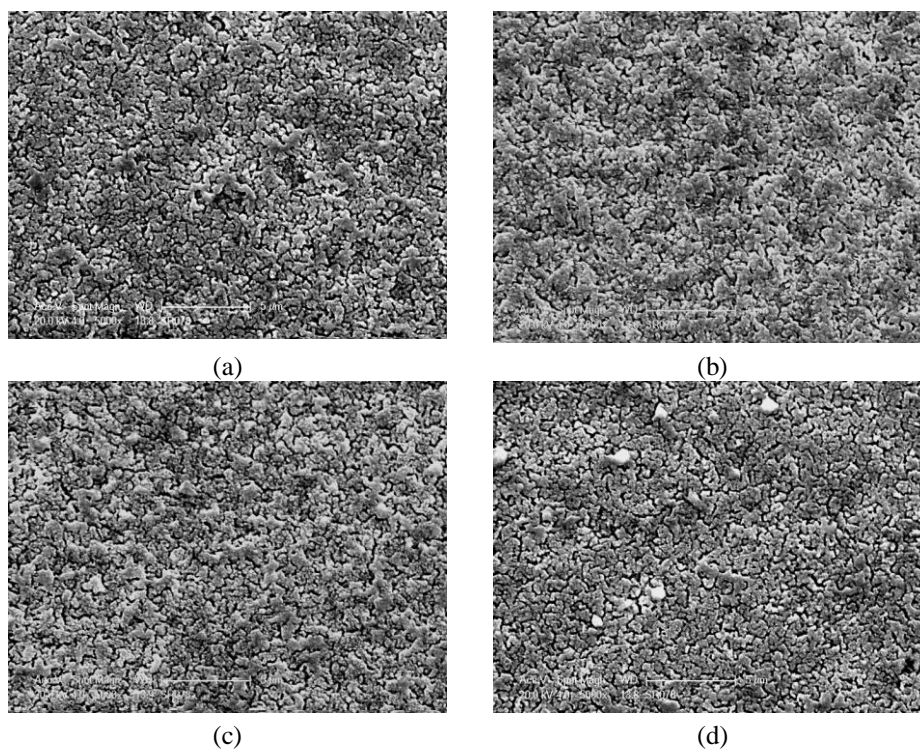


Figure 5.33 Surface morphologies of (a) F(L-C0), (b) F(L-C1), (c) F(L-C2) and (d) F(L-C3) films.

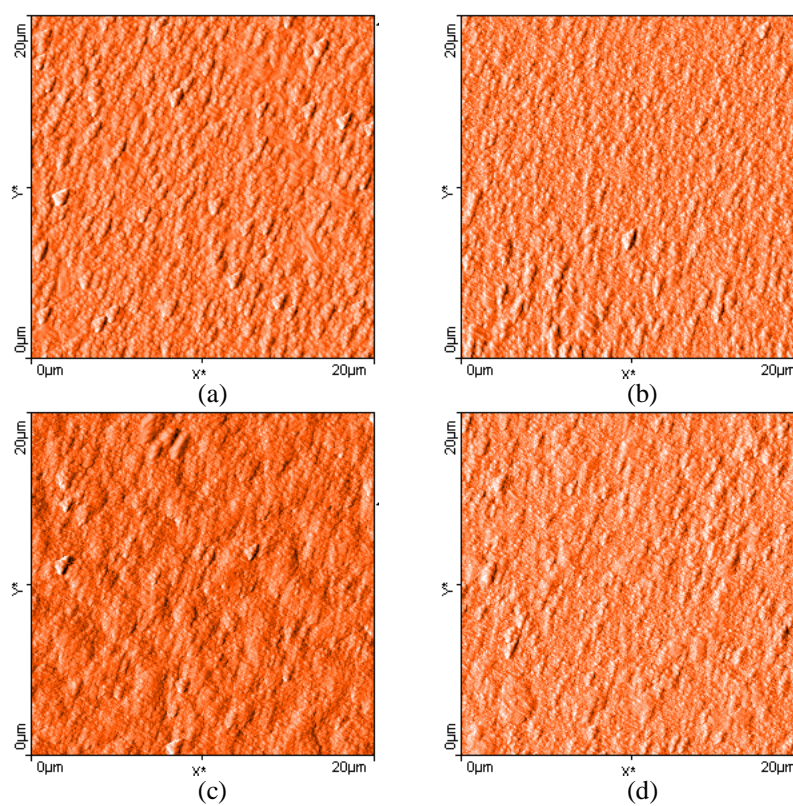


Figure 5.34 AFM images of (a) F(S-C0), (b) F(S-C3), (c) F(L-C0) and (d) F(L-C3) films.

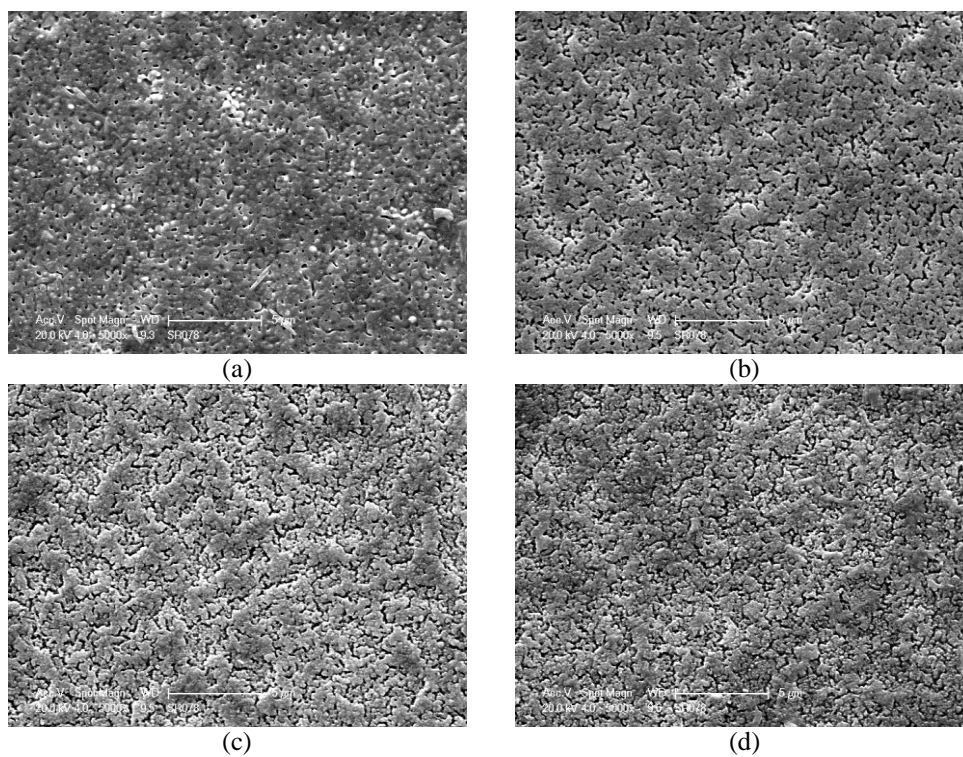


Figure 5.35 Surface morphologies of (a) F(S-D0), (b) F(S-D1), (c) F(S-D2) and (d) F(S-D3) films.

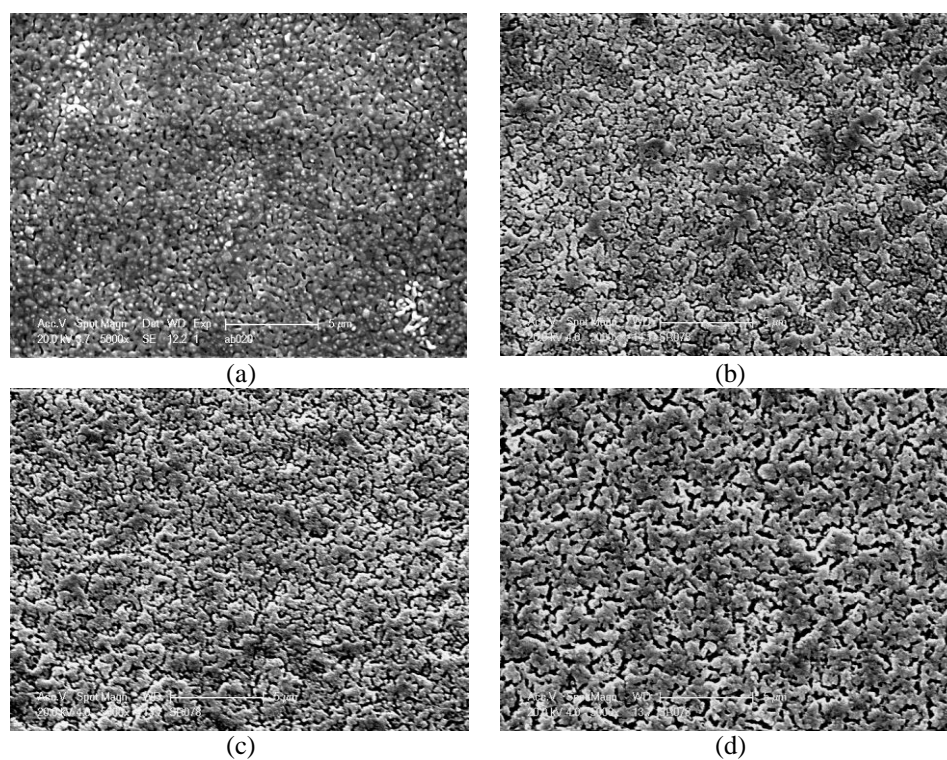


Figure 5.36 Surface morphologies of (a) F(L-D0), (b) F(L-D1), (c) F(L-D2) and (d) F(L-D3) films.

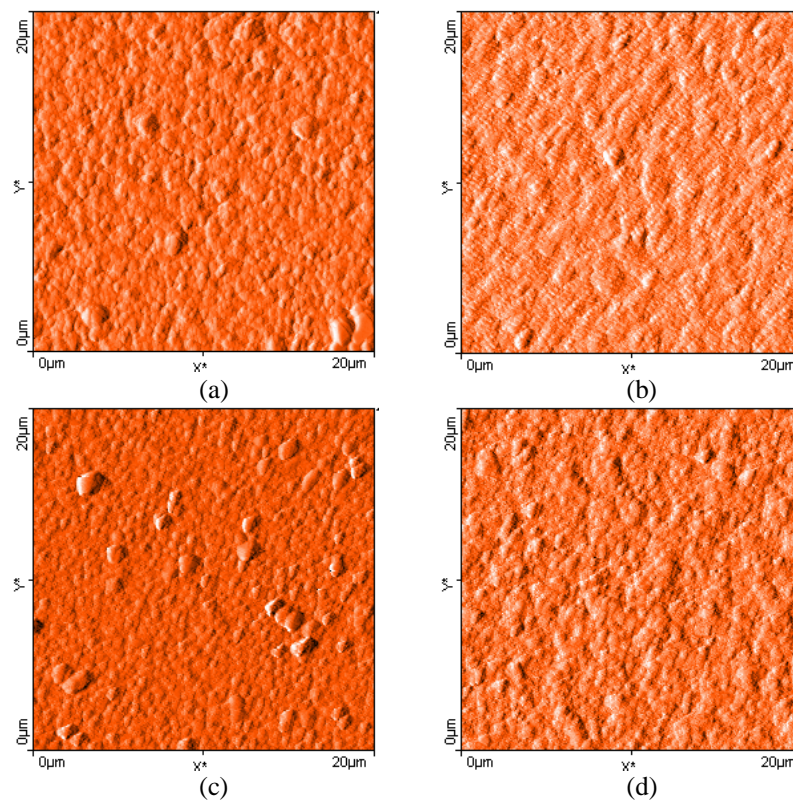


Figure 5.37 AFM images of (a) F(S-D0), (b) F(S-D3), (c) F(L-D0) and (d) F(L-D3) films.

Table 5.2 Surface roughness and film thickness measurement results of films.

Name of Films	Surface Roughness (S_a nm)	Film Thickness (nm)
F(S-B0)	1.0	230
F(S-B3)	2.48	270
F(L-B0)	4.02	228
F(L-B3)	3.91	256
F(S-C0)	3.44	220
F(S-C3)	2.34	260
F(L-C0)	2.51	238
F(L-C3)	2.26	265
F(S-D0)	2.26	226
F(S-D3)	2.22	238
F(L-D0)	4.52	242
F(L-D3)	2.01	251

5.2.4 Superconducting Properties of YBCO Thin Films Prepared from Methanol-, Ethanol- and Propionic Acid-Based Solutions with BZO Pinning Centers

To appraise the effect that the addition of BZO has on the superconducting properties of YBCO thin films, a number of measurements as inductive critical transition temperature (T_c) and critical current density (J_c) as well as transport measurement were undertaken. The more important material characteristics for these are now discussed with emphasis on the influence of BZO in YBCO films.

First of all, the T_{c90} (K) and ΔT_c (K) of all samples were measured inductively as presented in Figures 5.38-5.40 for samples prepared on STO substrates and in Figures 5.42-5.44 for samples prepared on LAO substrates. Additionally, numerical values of T_{c90} (K) and ΔT_c (K) are plotted for films prepared on STO and LAO substrates in Figures 5.41 and 5.45, respectively. Generally speaking, sharp voltage-temperature and narrow phase shift-temperature curves represent high superconducting quality. In the case of transition width (ΔT_c), the higher ΔT_c is, the worst superconducting properties are. In addition, the transition width is the measure of quality and homogeneity of the samples.

For the samples prepared on STO and LAO substrates from methanol and ethanol-based solutions, there is not a noteworthy result of measurements which can be generalized. To illustrate these, the undoped film F(S-B0) has the lowest T_c value in comparison to the F(S-B1), F(S-B2) and F(S-B3) films. In the F(S-C) series of films, T_c value decreases with dopant contribution in the structure and then increases again. F(L-B) series of films exhibit the same T_c manner as F(S-C) series whereas they have extremely large transitions. In the F(L-C) series of films, there exist a T_c fluctuation within undoped and doped samples which have very close values to each other. It is considered that these low T_c values and broad transition can be attributed to the formation of $BaCO_3$ and Y_2O_3 phases.

The T_c for the undoped film of F(S-D) series, for instance F(S-D0), is virtually 90.05 K and decreases in a linear manner as a function of increased dopant

concentration to approximately 88.15 K for the 18 mol % BZO addition. It can be expressed that the width of the superconducting transition ΔT_c remains quite good below 1 K for the undoped film as well as lower concentrations of BZO. Nevertheless, this transition width is greatly increased to around 2 K. The same trend is also observed for F(L-D) series of films. T_c values of samples decreased from 90.9 K to 89.6 K linearly as the BZO concentration increased and ΔT_c values were increased drastically from 1.0 K to 3.55 K. Zr diffusion into YBCO and substitution on yttrium (Y) sites might be the reason for lowered T_c . Moreover, the island growth surface morphology with high porosity is the other reason for decrease in T_c value.

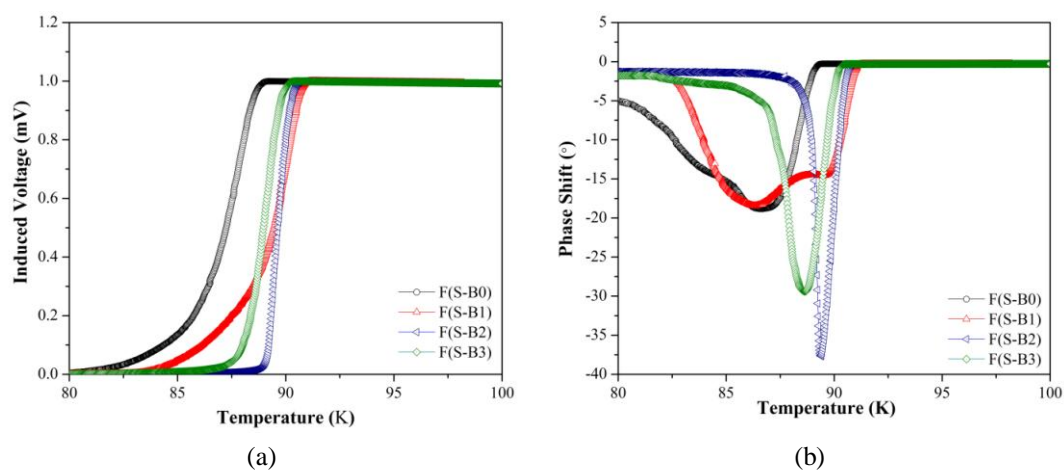


Figure 5.38 (a) Resistivity vs. temperature, (b) phase shift vs. temperature graphs of F(S-B0), F(S-B1), F(S-B2) and F(S-B3) films.

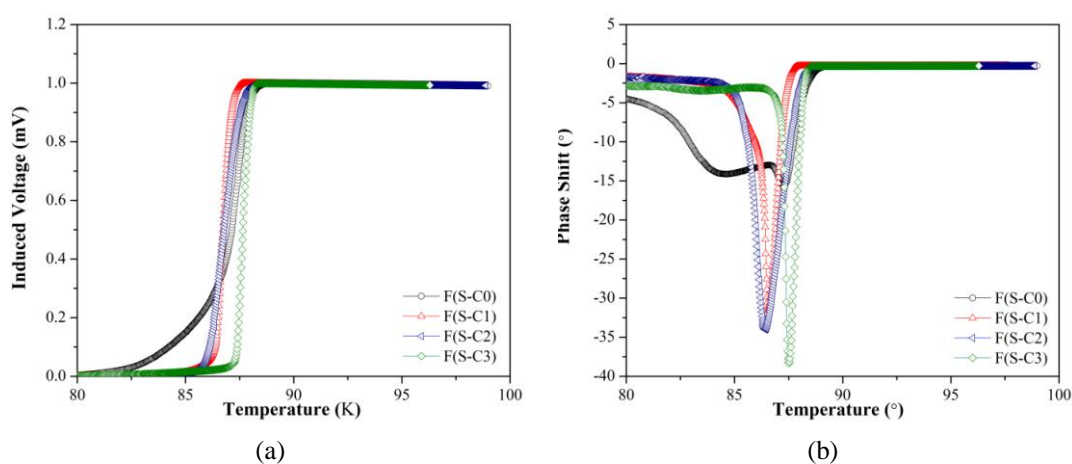


Figure 5.39 (a) Resistivity vs. temperature, (b) phase shift vs. temperature graphs of F(S-C0), F(S-C1), F(S-C2) and F(S-C3) films.

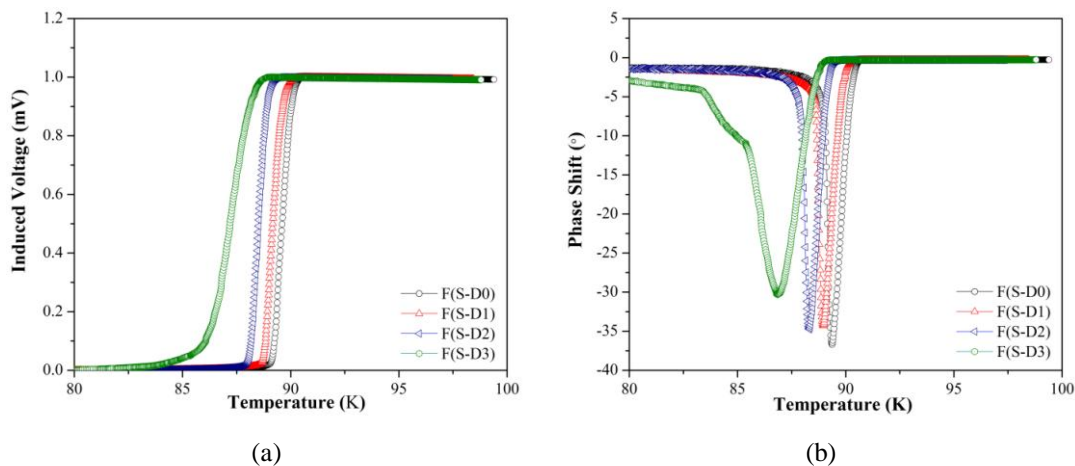


Figure 5.40 (a) Resistivity vs. temperature, (b) phase shift vs. temperature graphs of F(S-D0), F(S-D1), F(S-D2) and F(S-D3) films.

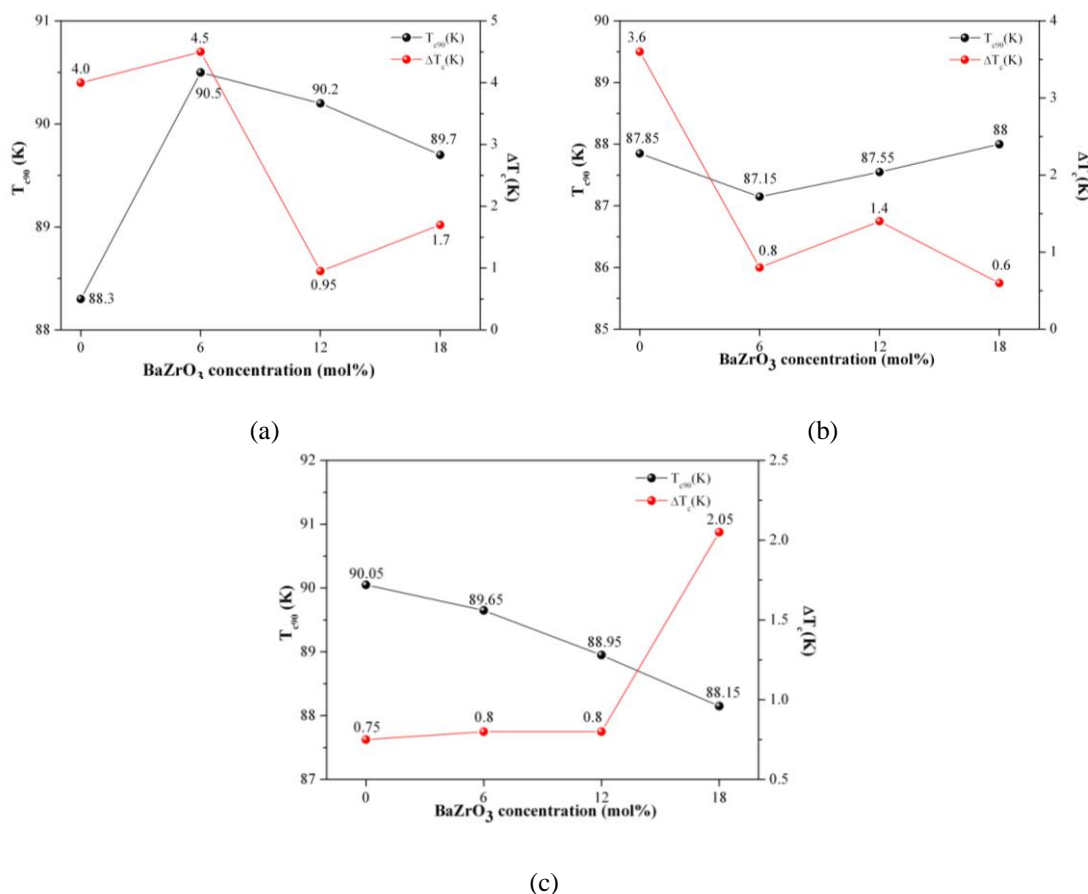


Figure 5.41 Dependence of inductively measured critical transition temperature (T_{c90}) and transition width (ΔT_c) on amount of BZO for (a) F(S-B), (b) F(S-C) and (c) F(S-D) series of films.

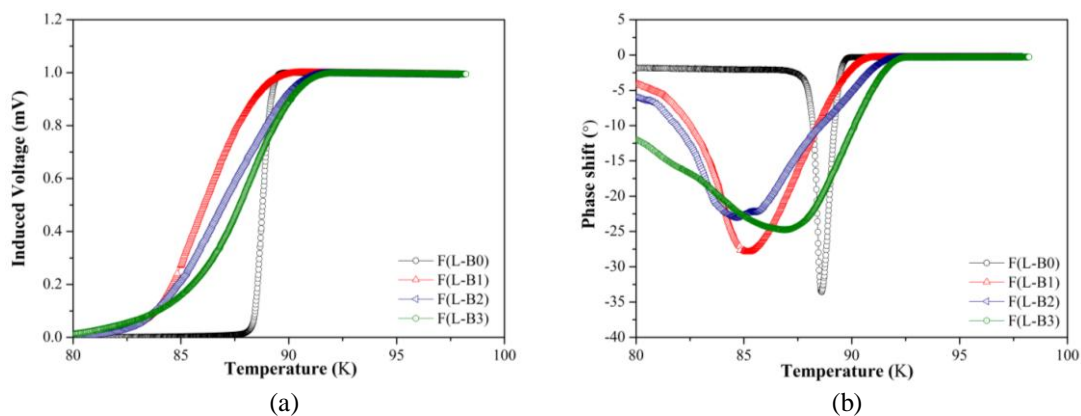


Figure 5.42 (a) Resistivity vs. temperature, (b) phase shift vs. temperature graphs of F(L-B0), F(L-B1), F(L-B2) and F(L-B3) films.

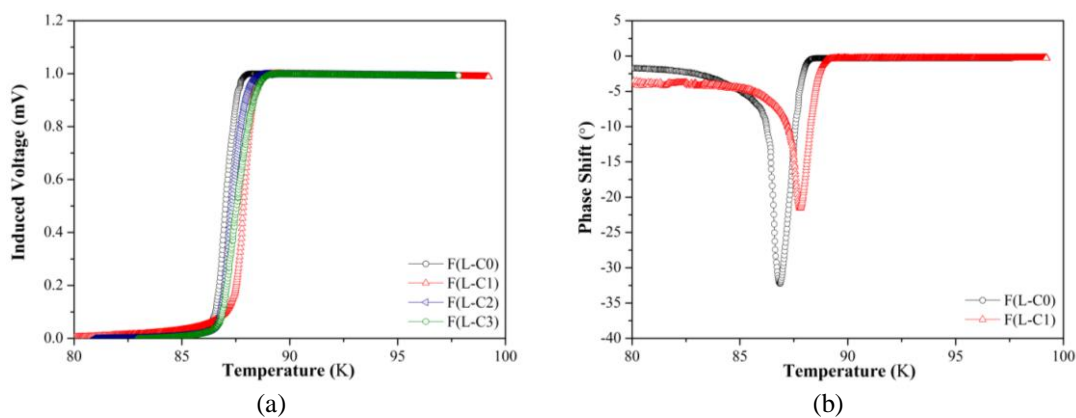


Figure 5.43 (a) Resistivity vs. temperature, (b) phase shift vs. temperature graphs of F(L-C0), F(L-C1), F(L-C2) and F(L-C3) films.

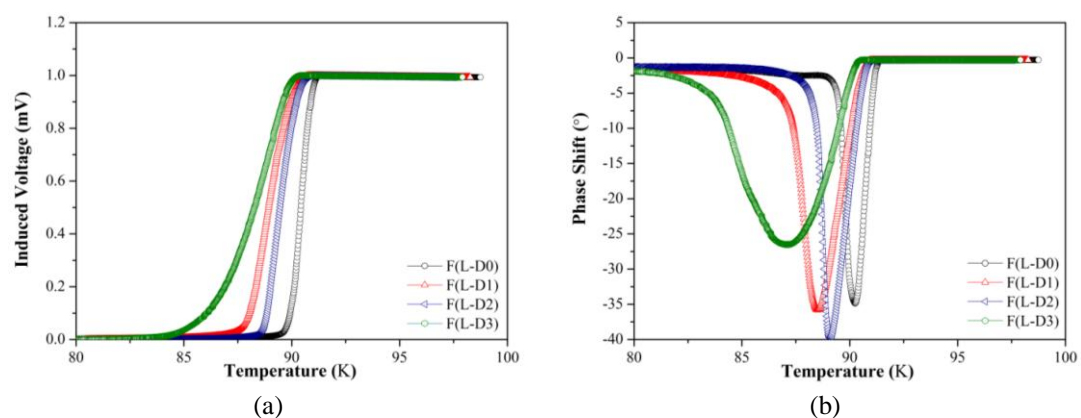


Figure 5.44 (a) Resistivity vs. temperature, (b) phase shift vs. temperature graphs of F(L-D0), F(L-D1), F(L-D2) and F(L-D3) films.

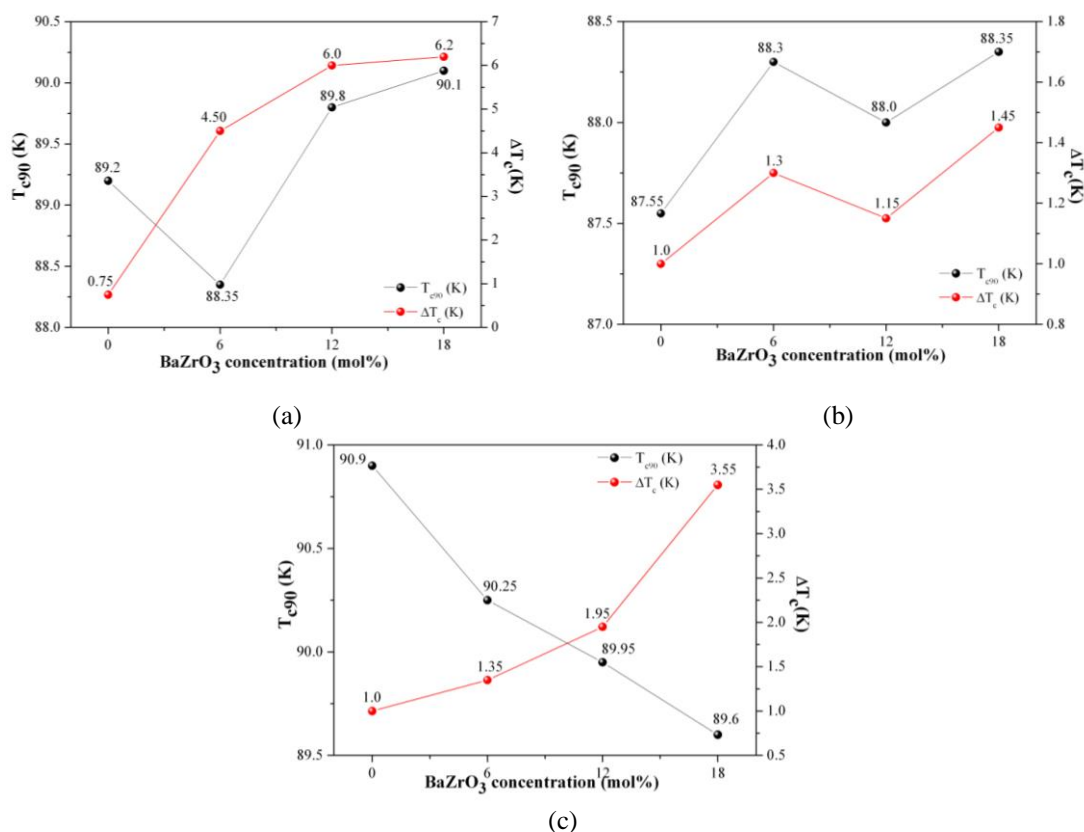


Figure 5.45 Dependence of inductively measured critical transition temperature (T_{c90}) and transition width (ΔT_c) on amount of BZO for (a) F(L-B), (b) F(L-C) and (c) F(L-D) series of films.

Similar results were obtained from critical current density (J_c) measurements as graphically shown in Figures 5.46 and 5.47. Samples prepared from methanol and ethanol-based solutions on STO and LAO substrates exhibit fluctuating J_c values with increasing dopant concentration. As experimentally proven by Chen et al., (2009), the amount of Zr dopants needs to be high enough to generate the density of defects to enhance the flux pinning in magnetic fields. However, too large amount of this nonsuperconducting content may also suppress the self-field and in-field J_c significantly. Their experimental results showed that Zr mol ratio $\sim 6.5\%$ did not significantly suppress the self-field J_c . Only samples prepared from propionic acid based solutions on STO and LAO substrates have continuously decreasing J_c values with BZO concentration. This is an expected effect for self-field conditions and further effects of BZO in in-field conditions are determined by transport measurements.

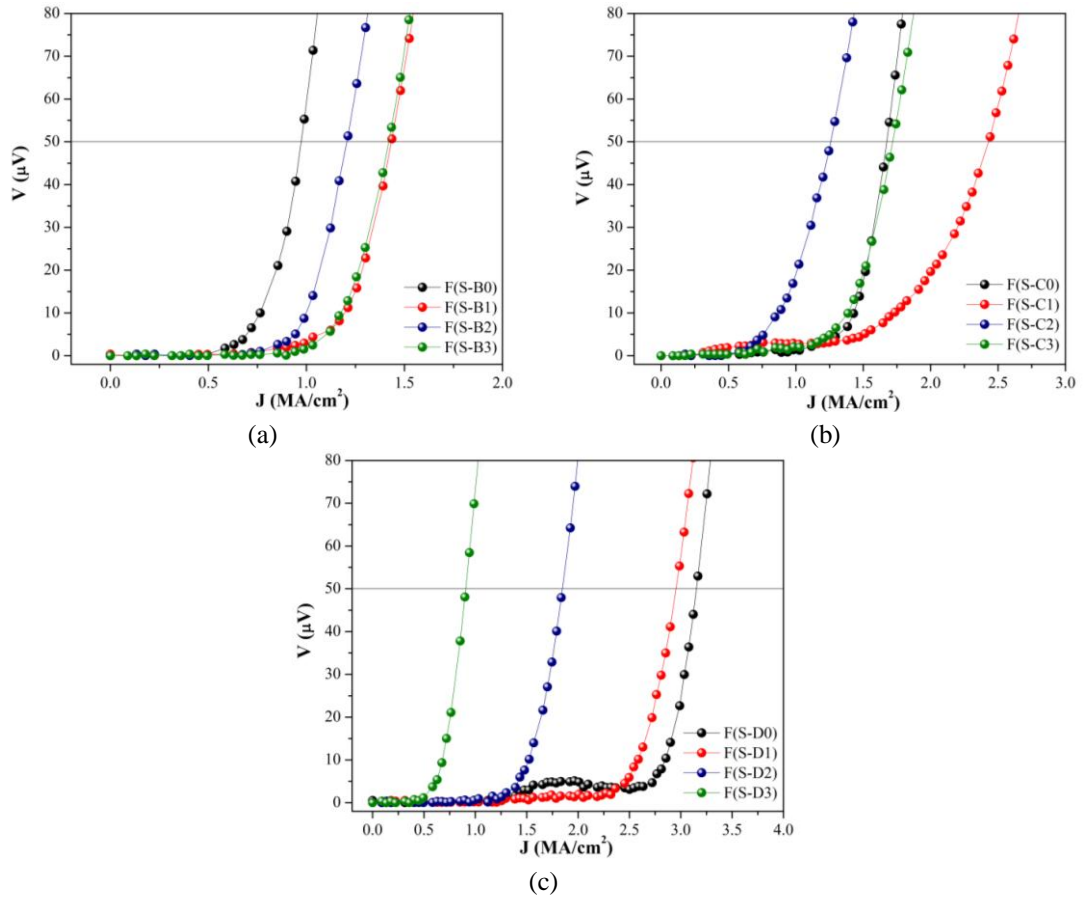


Figure 5.46 Inductive critical current density (J_c) measurements of undoped and BZO doped YBCO films at 77 K in self-field for (a) F(S-B), (b) F(S-C) and (c) F(S-D) series.

In order to perform most accurate quantitative measurements of flux pinning experiments performed J_c as a function of field and temperature. As a result of T_c and self-field J_c measurements, it is concluded that F(S-D) and F(L-D) series films have better superconducting properties which worth to perform further measurements in order to determine performance at high fields. Therefore, transport measurements were performed up to 6 T at 77 K in order to determine the magnetic field dependence of the critical current density as demonstrated in Figures 5.49 (a) and 5.50 (a).

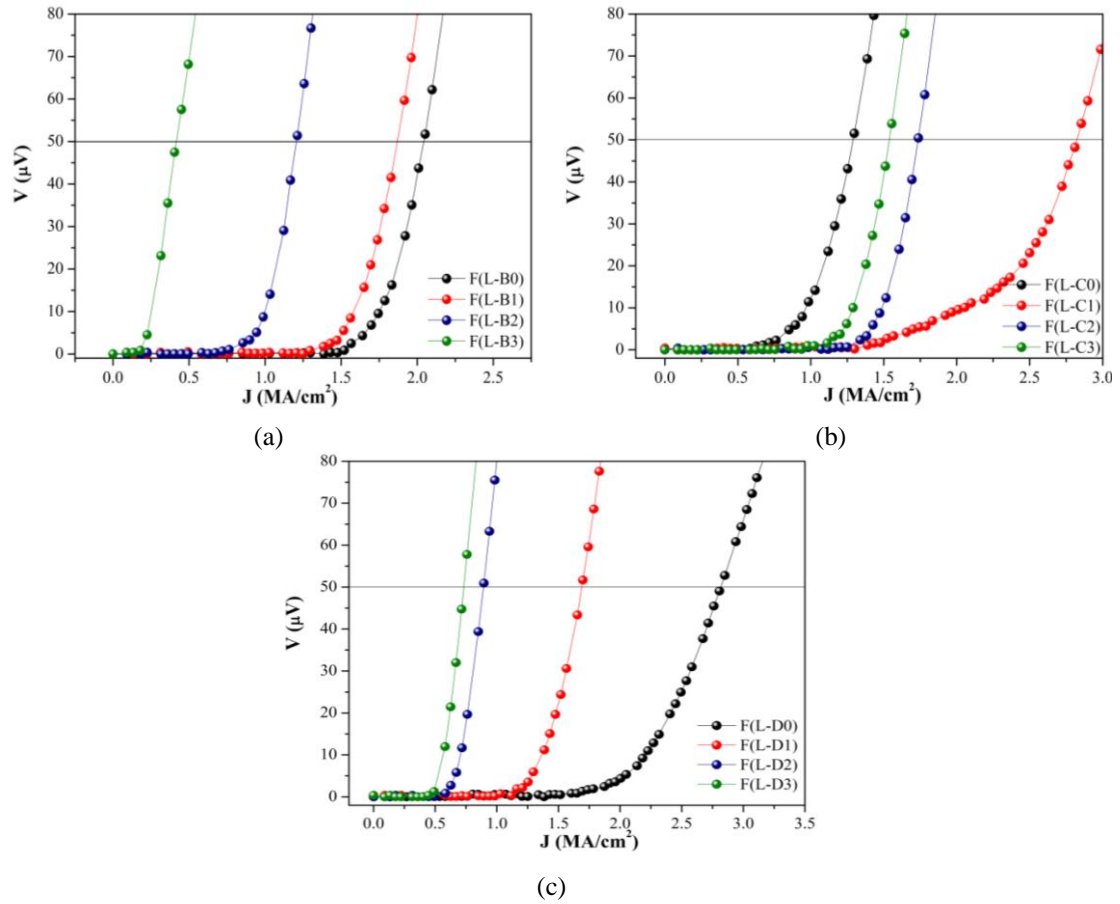


Figure 5.47 Inductive critical current density (J_c) measurements of undoped and BZO doped YBCO films at 77 K in self-field for (a) F(L-B), (b) F(L-C) and (c) F(L-D) series.

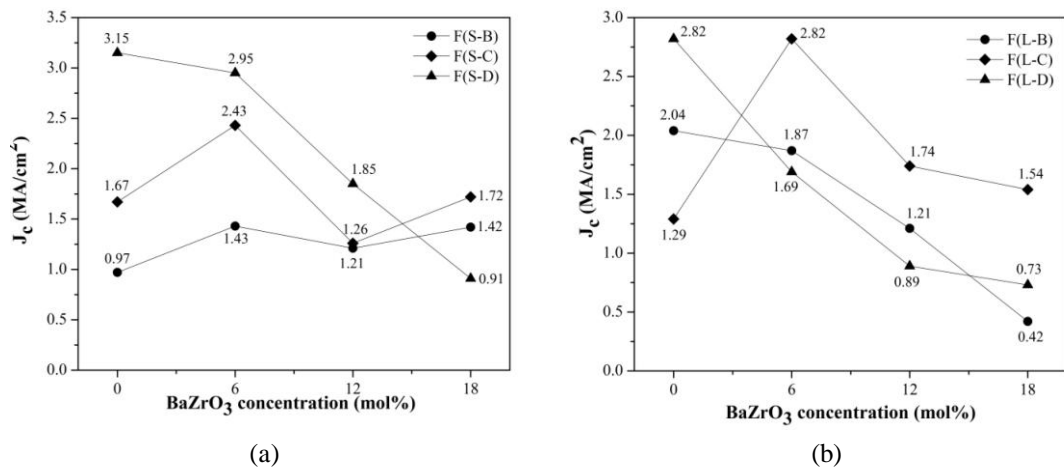
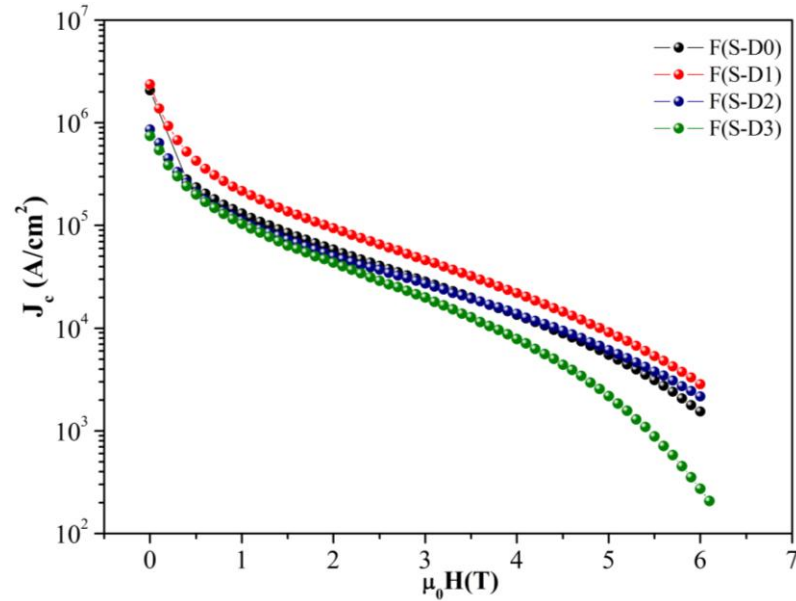
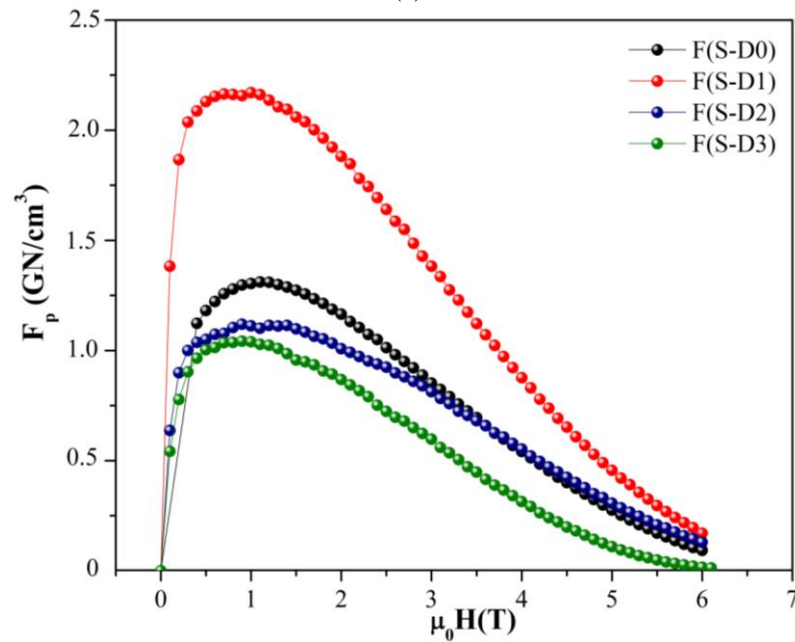


Figure 5.48 Dependence of inductively measured critical current density (J_c) on the amount of BZO for B, C and D series on (a) STO and (b) LAO substrates.



(a)

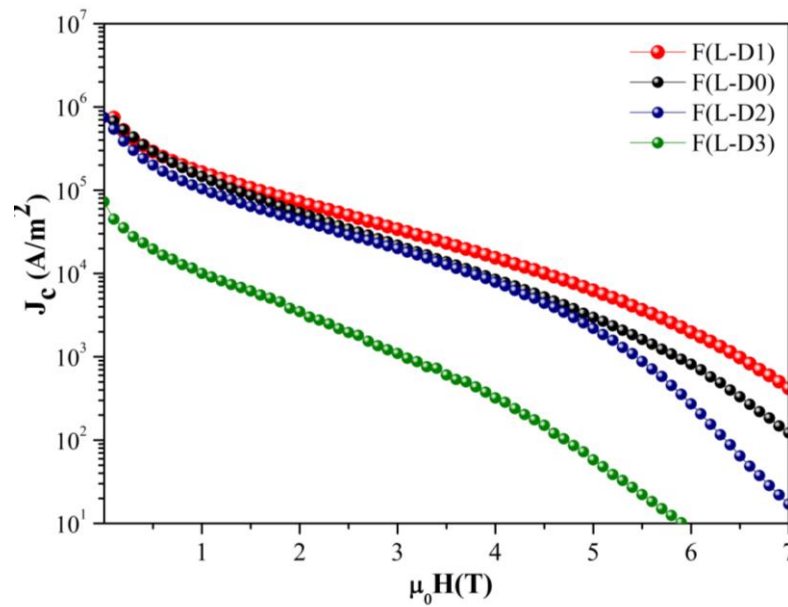


(b)

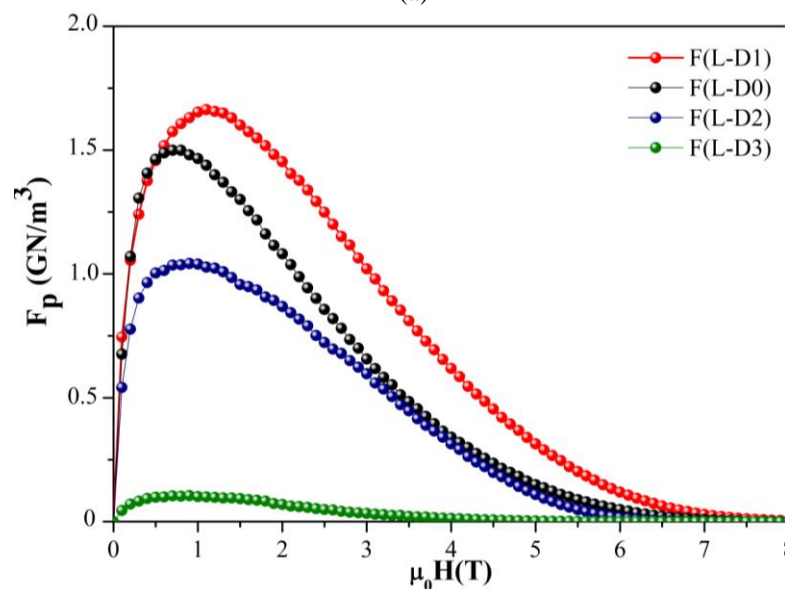
Figure 5.49 (a) Field dependence of the critical current density and (b) pinning force density up to 7 T at 77 K for F(S-D) series of films.

It can be seen that the 6 mol% BZO doped YBCO films (F(S-D1) and F(L-D1)) possess the highest J_c value for all magnetic fields. For F(S-D) series films, at fields lower than 4 T, the undoped sample has higher J_c value than 12 mol% doped sample. However, the drop rate of 12 mol% doped sample is slower than the pure YBCO and J_c value of this sample exceeds the value of undoped YBCO sample at fields higher

than 4 T. In the case of F(L-D) series films, undoped sample performed better than 12 mol% BZO doped sample. Within all the samples, the 18 mol% doped YBCO film has the lowest J_c value even at high fields which means that the superconducting structure of YBCO film is destroyed; self-field and in-field properties are suppressed with the excess amount of dopants concentration.



(a)



(b)

Figure 5.50 (a) Field dependence of the critical current density and (b) pinning force density up to 7 T at 77 K for F(L-D) series of films.

The overall increase in J_c at all magnetic fields can be more clearly seen when the magnetic field dependence of the pinning force, $F_p = J_c(B) \times B$, is presented. As shown in Figures 5.49 (b) and 5.50 (b), in spite of the fact that J_c decreases monotonically with increasing field, F_p increases to a maximum value $F_{p \max} = 2.5 \text{ GN/m}^3$ at the field of 1.5 T for F(S-D1) film and 1.70 GN/m^3 at the field of 1.5 T for F(L-D1) film.

5.3 GdBCO Thin Film Production from Gd-Acetate Based Precursor

The development of high temperature superconductor (HTS) coating with high J_c offers great promise for applications of HTS on various superconducting devices such as cable, transformer, generators and motors operating at 77 K (Kim, Lim, Kim, Hong, & Lee, 2006). YBCO is one of the most promising HTS materials because of its high irreversibility field, B_{irr} , critical current density J_c and critical transition temperature, T_c . It is the most widely and thoroughly investigated high temperature superconductor and most of the coated conductor development is undertaken on YBCO. However, high temperature superconductivity is also observed for materials in which a rare earth (RE= Gd, Eu, Sm, Er, Nd, etc.) element is substituted for Y. Therefore, REBCO is also one of the attractive HTS materials, in so far as it has exhibited higher T_c than YBCO as well as higher J_c in magnetic fields (Iguchi, Araki, Yamada, Hirabayashi, & Ikuta, 2002; Kaneko et al., 2005). Coated conductors using REBCO superconductors are expected to be used in high field applications such as nuclear magnetic resonance (NMR), superconducting magnetic energy storage system (SMES) and nuclear fusion (Haruta et al., 2006).

Recently, GdBCO have been also used for the fabrication of coated conductors and shows promising properties. Especially the higher transition temperature T_c compared to YBCO makes it a better candidate for applications at 77 K. Generally Gd is selected as a RE element in the REBCO system because of its isotropic property and additionally, Gd is a promising alternative because of strong flux pinning due to the Gd-Ba substitution. Generally speaking, REBCO systems have $RE_{1+x}Ba_{2-x}Cu_3O_{7-\delta}$ type solid solution, in which substitutions of RE elements for Ba sites considerably suppress T_c in self-field. Therefore, it is not easy to control the

superconducting properties as well as the ratio of Ba/RE. Nonetheless, in the case of in-field conditions, these solid solutions may act as intrinsic pinning centers and increase the pinning potential of the REBCO system (Kitoh et al., 2007; Kaneko et al., 2005). Additionally the very similar ionic radii of Gd and Ba results in a higher degree of disorder and, hence, in pinning sites, which further improves the pinning properties especially at elevated temperatures (Rosenzweig, Hänisch, Hühne, Holzapfel, & Schultz, 2010).

According to Haberkorn, Lovey, Condo, & Guimpel (2005), the higher T_c and J_c in $\text{GdBa}_2\text{Cu}_3\text{O}_{7-\delta}$ compared to YBCO might arise from extra stacking faults. These stacking faults are formed by growth of extra Gd layer which forms an edge dislocation and shifts the other layers such as Cu-O and Ba-O causing layer mismatch.

Kaneko et al. (2005), reported that misfit parameter of GdBCO/STO is smaller than that of YBCO/STO as listed in Table 5.3. In addition, since $\Delta G^*_{\text{REBCO}}$ is smaller than ΔG^*_{YBCO} , so nucleation rate of REBCO is suggested to be higher than that of YBCO. From these theoretical outcomes, they suggest that REBCO crystals easily nucleate and are epitaxially grown considering from the viewpoint of the lattice matching to the STO substrate.

Table 5.3 The a-axis lattice parameters and misfit parameters along the direction of $[100]_{\text{film}}$ and $[100]_{\text{STO}}$. Orientation relationships between the REBCO film and the STO substrate is $(001)_{\text{film}} \parallel (001)_{\text{STO}}$ and $[100]_{\text{film}} \parallel [100]_{\text{STO}}$. (Kaneko et al., 2005).

	a-axis lattice parameter (nm)	a-axis misfit parameter on STO (%)
YBCO	0.38877	0.444
GdBCO	0.38947	0.264
SrTiO ₃	0.3905	-

According to recent studies, GdBCO has higher T_c than YBCO, resulting in higher B_{irr} in thin films at 77 K. Also, for GdBCO thin films and coated conductors a higher critical current density J_c is reported in high magnetic fields at 77 K. Iguchi et al and Kaneko et al reported that GdBCO superconductor films on single crystalline substrates exhibited a high critical temperature and critical current density as

$T_c=92.9$ K and $J_c= 2.9$ MA/cm² (77 K, self field) respectively. The angular dependence of J_c was more isotropic for GdBCO than for YBCO and the volume of a-oriented grains does not grow as in YBCO as film thickness increases. Moreover, a lower deposition temperature and higher deposition rate were reported for pulse laser deposited, sputtered and melt-grown GdBCO than for YBCO. Therefore, GdBCO is very promising for applications and several demonstrations have been done for the performance of GdBCO as long coated conductors and test coils (Iguchi et al., 2002; Murakami, Sakai, Higuchi, & Yoo, 1996).

Though GdBCO is very promising material for application, aging effect is a drawback for fabrication of it as thin films. This effect is observed by Schlesier et al. and tried to overcome by cap layer applications (Schlesier, Huhtinen, Granroth, & Paturi, 2010).

5.3.1 Precursor Solution Characterization

GdBCO solution (SolE) was prepared by dissolving Gd, Ba and Cu acetates into deionized water in a 1:2:3 cation ratio with TFA at room temperature as described beforehand in Chapter 4. This aqueous solution was refined under vacuum atmosphere with evaporator to yield a glassy blue residue containing impurities of water and acetic acid. The residue was dissolved in sufficient ethanol and refined again to expel the impurities to yield a glassy blue residue containing ethanol. After two cycles of refining processes, the resultant blue residue was dissolved in ethanol to give a solution with a metallic ion concentration of 0.25 M.

Shear profile of the prepared solution was determined with rheological measurements under standard conditions of 25 °C, 2 hours with constantly increasing shear rates (1-1200 s⁻¹). Figure 5.51 (a) clarifies viscosity of the solution under increasing shear rate conditions. The mean viscosity value within the given ranges is 10.36 mPa.s. In order to determine the influence of temperature on viscosity characteristics of solution, measurements were performed at constant shear rate of 400 s⁻¹ and at increasing temperature from room temperature to 60 °C. Based on the

graph on Figure 5.51 (b), viscosity value was slightly decreased with increasing temperature. It was pointed out that the mean viscosity value was 7.83 mPa.s.

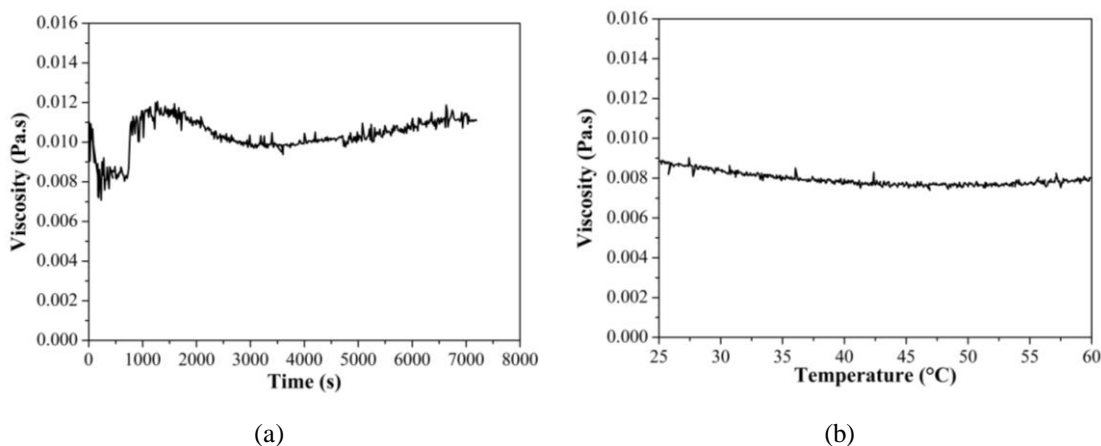


Figure 5.51 (a) Viscosity measurement of solution at room temperature and increasing shear rate. (b) Viscosity measurement of solution at increasing temperature and constant shear rate.

Figure 5.52 summarizes the decomposition thermodynamic of all precursors used in the precursor solution preparation process. Y-ac and Gd-ac exhibits similar behavior as they decompose and the great amount of mass loss is around 350 °C. In the case of Ba-ac, the only reaction is approximately 500 °C. At this temperature BaF₂ forms in the structure. For Cu-ac, the decomposition reaction takes place around 270 °C. This low reaction temperature for Cu-ac is due to its volatile character under normal atmosphere conditions. Cu compounds sublime easily unless there is a humidified atmosphere and that would cause deterioration in the stoichiometry of the structure. For Zr-pentanedionate, the reaction occurs below 200 °C which indicates that Zr substitutes into Y-sites during the pyrolysis stage of the heat treatment. Similar measurements were also performed to the Y, Ba and Cu precursors by Fang, Huang, Chen, Liaw, & Hurng, (1994), and results match to each other.

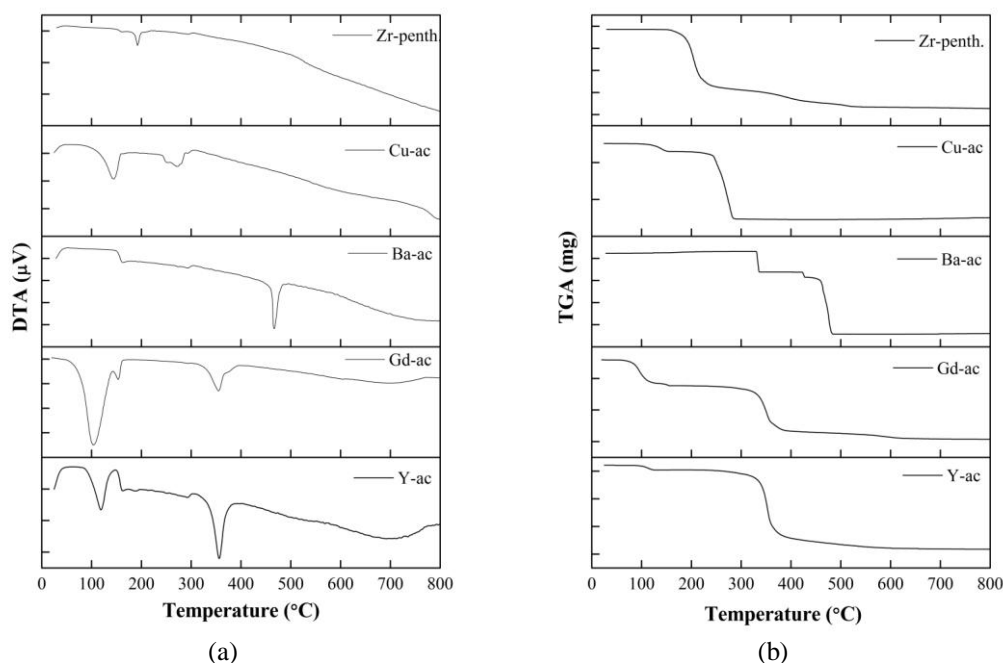


Figure 5.52 Thermal analysis and mass loss diagrams of all precursor materials.

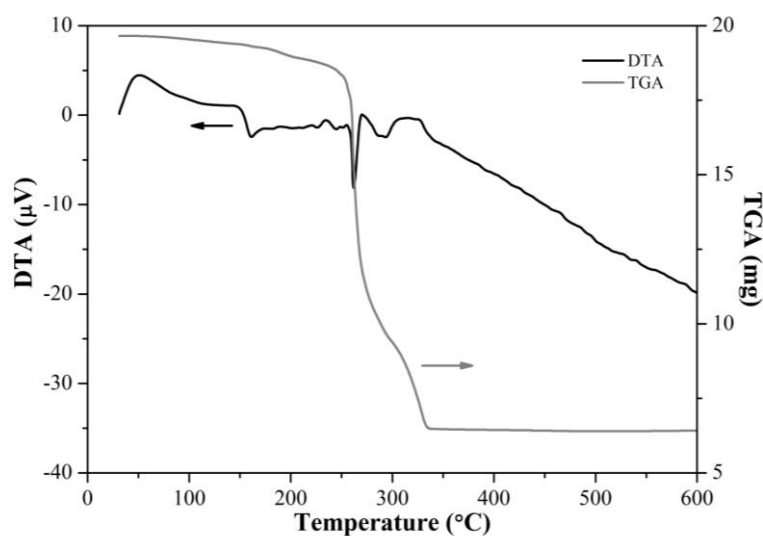


Figure 5.53 DTA/TG analysis of dry gel of precursor solution SolE.

In order to obtain information about the decomposition behavior of dry gel of precursor solution, a DTA-TGA analysis was carried out. In general, DTA-TGA spectrums are quite similar for all dried samples of ethanol and methanol based precursor solutions. This similarity comes from the chemical structures of precursor materials. Acetate based structures of Y and Gd exhibit parallel behavior as they

decompose around 350 °C. FTIR spectra of SolE and xerogel of SolE are shown in Figure 5.54. Note here that the band at high frequencies is due to the O-H stretch from water and CO₂ from the atmosphere. Apart from this, the band at 1671 cm⁻¹ belongs to the C=O of HOAc group. Bands smaller than 1400 cm⁻¹ represent the gel structure of acetate based precursor materials.

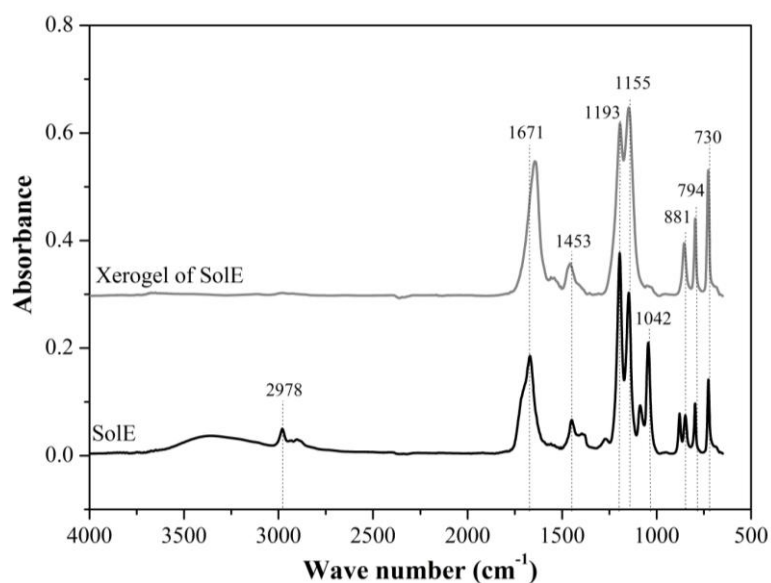


Figure 5.54 FTIR spectra of SolE and xerogel of SolE.

5.3.2 Crystallization Temperature Determination for GdBCO Thin Films

Many studies were performed (Fukushima, et al., 2007; Sutoh, et al., 2009) using pulse laser deposition technique for GdBCO thin film structures but little attention has been taken for the chemical deposition of this system. Therefore, applying the TFA-MOD method for the preparation of GdBCO films would be of great interest. In literature there are many studies about application of TFA-MOD method to the other REBCO systems. Recently in literature, Honjo et al. (2001) reported on the fabrication of a Nd-Ba-Cu-O film using TFA-MOD method with a T_c of 89 K. Apart from these researches, Haruta et al. (2006) reported that ErBCO thin films prepared by PLD method also exhibit good superconducting properties. Reports on MOD grown GdBCO films are still very limited in comparison with those on MOD grown YBCO films. Therefore, production of GdBCO superconducting thin films by MOD method is the motivation point of this study.

As reported in many studies, GdBCO thin films prepared with pulse laser deposition technique has a lower deposition temperature than YBCO. One of them is performed by Chen et al. (2009). They produced 3 different GdBCO films at 820, 830 and 840 °C by PLD method. As a result of their study, a higher deposition temperature resulted in a suppression of the J_c at B||c. There are many examples in the literature which are comparable to each other. Miyachi, Sudoh, Ichino, Yoshida, & Takai (2003) deposited GdBCO on MgO (100) substrates at a deposition temperature of 850 °C and Song et al. (2007) on SrTiO₃ (100) at 810 °C. Li, Geerk, Smithy, Liu, & Xu (1997) with sputtering method deposited on LaAlO₃ (100) with a deposition temperature of 820 °C. The highest recorded deposition temperature in the literature is 910 °C with PLD method on LAO (100) substrates (Rosenzweig et al., 2010).

In that part of the thesis, GdBCO thin films on STO single crystal substrates fabricated by the MOD process using spin coating technique at a rotation speed of 6000 rpm and acceleration speed of 6000 rpm s⁻¹ for 30 s. To optimize the processing parameters, firing temperature was varied from 780 to 810 °C. GdBCO films were characterized and effects of firing temperature on the microstructures and superconducting properties were reported.

The XRD patterns of GdBCO films fired 780-810 °C are shown in Figure 5.55. It is clear that at all temperatures (h00) STO and (00l) GdBCO orientations are observable which means that all GdBCO films are strongly c-axis oriented. With increasing firing temperature to 800 °C, intensities of GdBCO peaks are also increased. However, the peak intensities of the GdBCO films fired at 810 °C are abruptly decreased, which is presumably caused by the thermal decomposition of the GdBCO phase. Iguchi et al. reported that GdBCO was decomposed below the stability line, given by $\log(P_{O_2} (Pa)) = 13.1 - 13.1 \times 10^4 / T(K)$, during the MOD process. According to this relation, the decomposition temperature of GdBCO film in 100 ppm Ar/O₂ atmosphere is ~810 °C, which is in good agreement with our results (Iguchi et al., 2002). The peak intensities of (004), (007) and (008) orientations in the

800 °C heat treated sample are much higher than the same orientations of other samples.

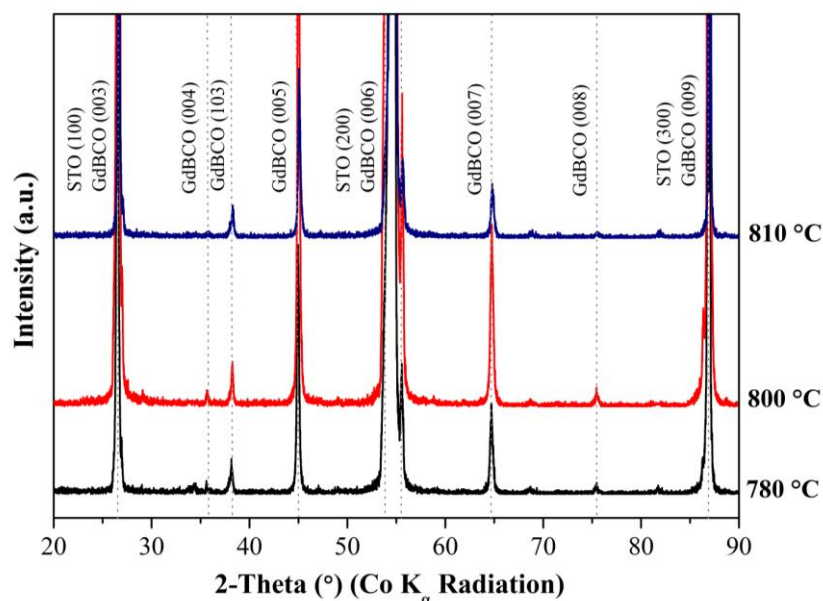


Figure 5.55 X-ray θ -2 θ scans of samples heat treated at 780, 800 and 810 °C with a CoK_α radiation. (GdBCO JCPDS card no: 01-086-0474, STO JCPDS card no: 035-0734).

The surface morphologies of samples crystallized at 780, 800 and 810 °C are shown in Figure 5.56. It is clear from the images that samples heat treated at 780 and 810 °C involves a-axis oriented grains. Notably in the 810 °C heat treated samples, the size of a-axis oriented grains are much longer than the 780 °C heat treated sample. The surface of sample which is heat treated at 800 °C is completely c-axis oriented, continuous and crack free.

The inductive measurements of critical transition temperature T_{c90} and ΔT_c are shown in Figure 5.57. Due to the large amount of a-axis oriented grains in the structures of samples heat treated at 780 and 810 °C, their T_{c90} values are lower and ΔT_c values are higher in comparison to the 800 °C heat treated sample. Table 5.4 summarizes all measurement results including the critical current density (J_c) for 3 different samples according to their heat treatment temperatures. It is apparent that the best results of T_{c90} , ΔT_c and J_c are obtained from the sample heat treated at

800 °C. All these results of characterizations have taken into consideration and it has decided to heat treat all samples of GdBCO at 800 °C.

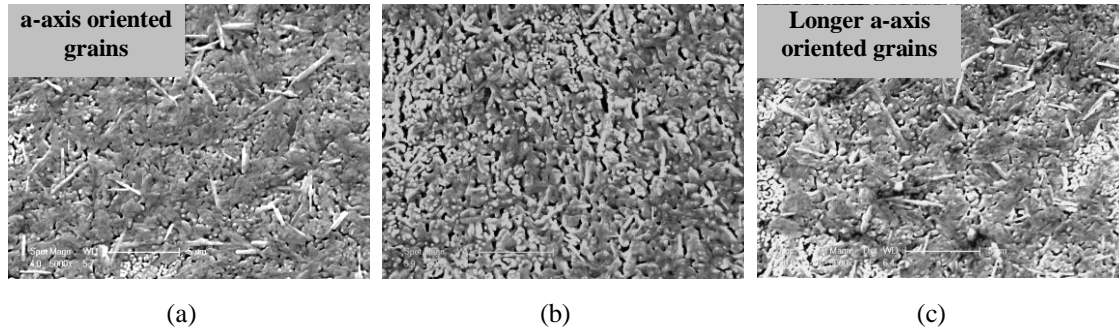


Figure 5.56 Surface morphologies of GdBCO samples heat treated at (a) 780, (b) 800 and (c) 810 °C. There are no a-axis oriented grains in the 800 °C heat treated sample.

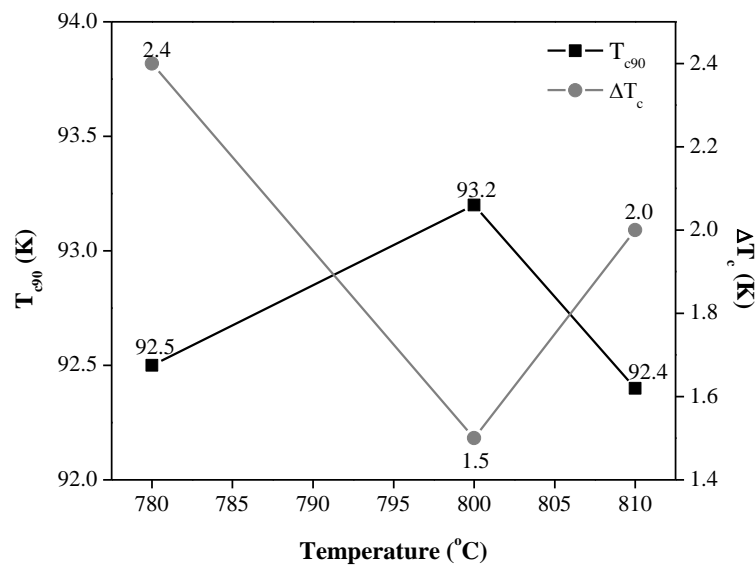


Figure 5.57 T_{c90} , and ΔT_c of samples heat treated at 780, 800 and 810 °C respectively.

Table 5.4 T_{c90} , ΔT_c and self-field J_c values of samples heat treated at from 780 to 810 °C.

Heat Treatment Temperature (°C)	T_{c90} (K)	ΔT_c (K)	J_c (MA/cm ²)
780	92.5	2.4	1.39
800	93.2	1.5	2.53
810	92.4	2.0	1.35

5.3.3 Structural Properties of GdBCO Thin Films with BZO Pinning Centres

GdBCO solution was divided into four parts each 10 ml, and different amounts of zirconium were added to each part by dissolving Zr(IV)-2.4-pentanedionate in the solutions. The Zr concentrations were adjusted to 0, 6, 12 and 18 mol% BaZrO₃ regarding to stoichiometric precursors. (100) oriented STO and LAO single crystal materials with dimensions of 10x10x1 mm³ were used as substrates to prepare GdBCO films by virtue of spin coating technique at a rotation speed of 6000 rpm and acceleration speed of 6000 rpm s⁻¹ for 30 s.

Figures 5.58 and 5.59 show the θ -2 θ diffraction patterns of undoped and BZO doped GdBCO films on STO and LAO substrates. Generally in these patterns, the major peaks correspond to the (001) reflections of the GdBCO phase and (100) reflections of STO and LAO substrates which indicates that the GdBCO films have a strong c-axis orientation. Based on the amount of dopant concentration, there is a slight increase at the BaZrO₃ (200) peak intensity for both series of samples. For the samples prepared on STO substrates, (004) peak intensity at $2\theta=35.6^\circ$ is lower for undoped sample than the doped sample. Besides, (103) orientation of GdBCO is apparent for the undoped sample whereas it is not for doped samples. This indicates that the structure of pure GdBCO sample becomes well-textured as the dopant introduced into the structure. Furthermore, increase in the (008) YBCO peak intensity with increasing BZO amount is evidence for this structural change. These results are not well-matched with the results of samples prepared on LAO substrates. (004) peak intensity is higher for undoped sample whereas it decreases when BZO dopant introduced into the structure. The textured structure of sample F(L-E0) deteriorated as (103) orientation of GdBCO become observable for the F(L-E1), F(L-E2) and F(L-E3) films.

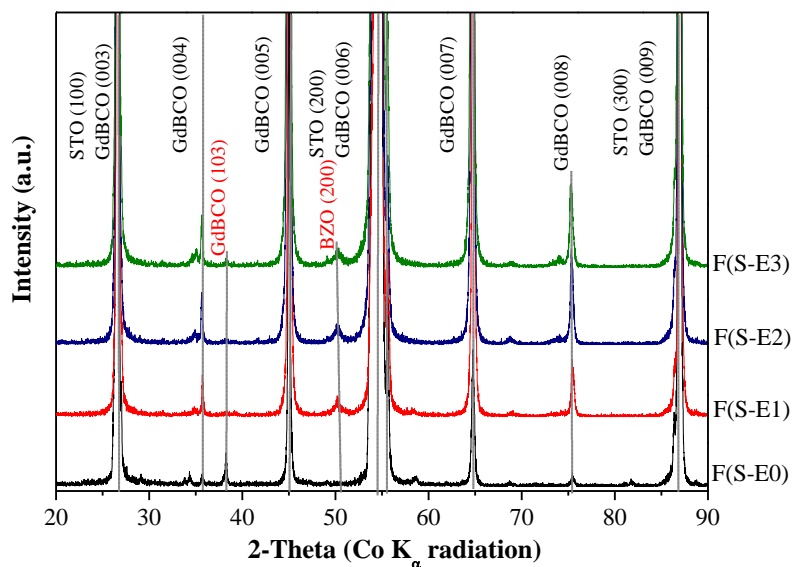


Figure 5.58 X-ray θ - 2θ scans of F(S-E0), F(S-E1), F(S-E2) and F(S-E3) films with a Co K_{α} radiation. (GdBCO JCPDS card no: 01-086-0474, BaZrO₃ JCPDS card no: 01-074-1299).

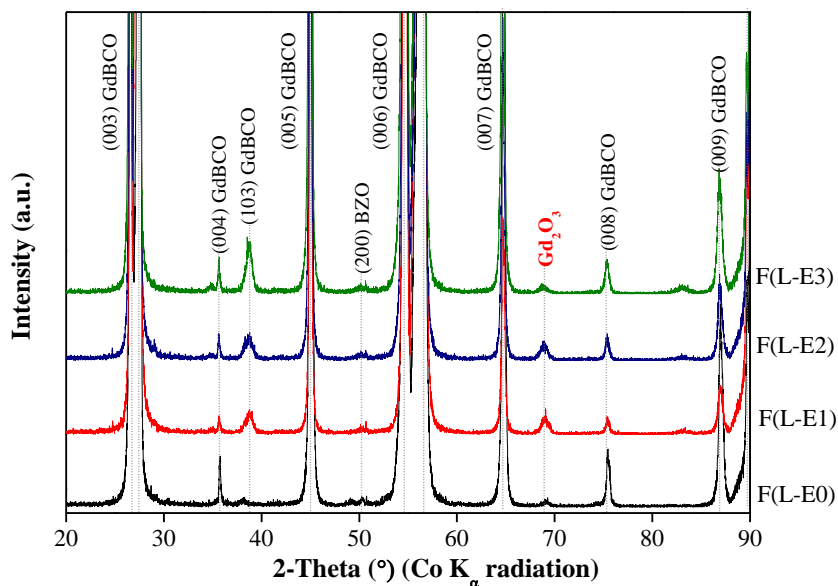


Figure 5.59 X-ray θ - 2θ scans of F(L-E0), F(L-E1), F(L-E2) and F(L-E3) films with a Co K_{α} radiation. (Gd₂O₃ JCPDS card no: 00-043-1015).

The in-plane texture analyses including ϕ -scan were carried out for the doped samples on both STO and LAO substrates. The samples with the highest dopant concentrations were chosen for texture measurements in order to obtain satisfactory data from BZO reflections.

In general, texture measurements revealed a perfect cube-on-cube epitaxial relationship between the STO/LAO substrates and GdBCO thin films. Figures 5.60 and 5.62 illustrate pole figure results of films of F(S-E3) and F(L-E3), respectively. The symmetric distribution of the pole peaks reveals that the GdBCO have textured structure on both STO and LAO substrates. The GdBCO (102) pole figures possess four evenly distributed, symmetric poles over the 360° ϕ -angle range indicating the texture and c-axis orientation. The minor texture components in the pole figures of (110) BZO represent the random oriented structure of these particles in the GdBCO matrix. There is not any additional a-axis oriented texture component was detected in the corresponding measurements.

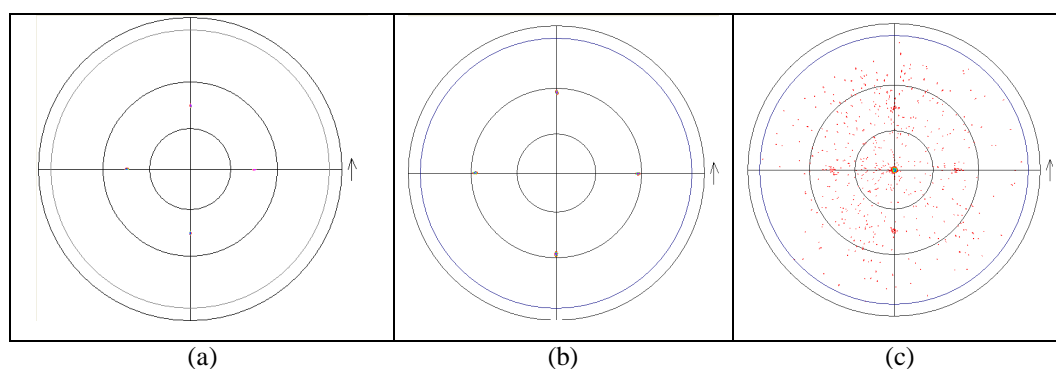


Figure 5.60 X-ray pole figure of (a) (110) reflection of STO, (b) (102) reflection of GdBCO and (c) (110) reflection of BZO.

The FWHM (full-width-at-half-maximum) values of GdBCO films are depicted in Figures 5.61 and 5.63 for F(S-E3) and F(L-E3) films. FWHM of GdBCO on STO and LAO substrates are 1.84 and 3.78, respectively. The ϕ -scan for BZO peak gives a wide-angle intensity distribution with FWHM is 8.74 and 9.77 suggesting a highly random orientation distribution of these particles in the oriented GdBCO structure for both substrates. Generally all scans have four sharp peaks in the case of low FWHM

values and textured structures, whereas the peak intensities are low and width of peaks is thick for random distributed structures.

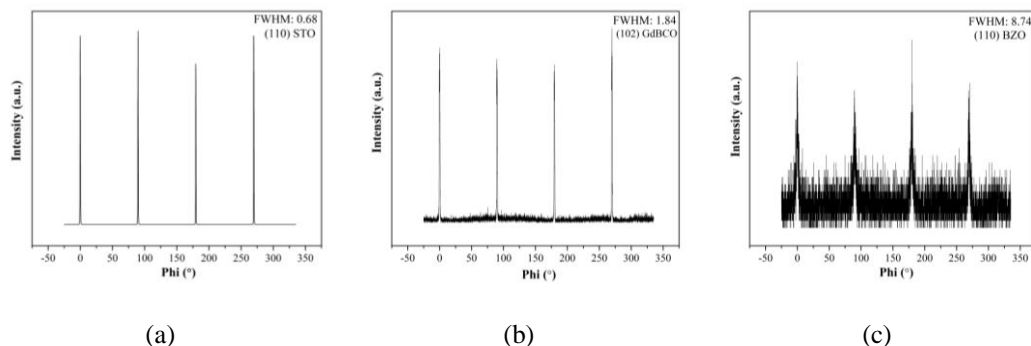


Figure 5.61 Φ -scans of (a) (110) STO, (b) (102) GdBCO and (c) (110) BZO for film F(S-E3).

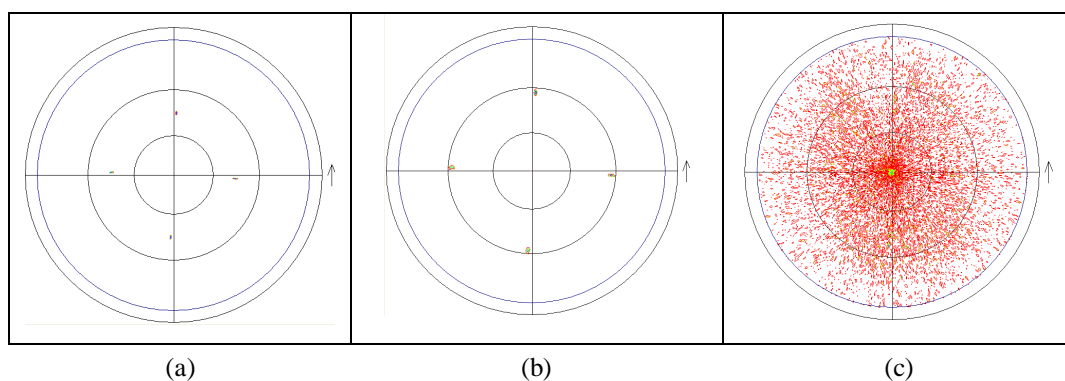


Figure 5.62 X-ray pole figures of (a) (110) reflection of LAO, (b) (102) reflection of GdBCO and (c) (110) reflection of BZO.

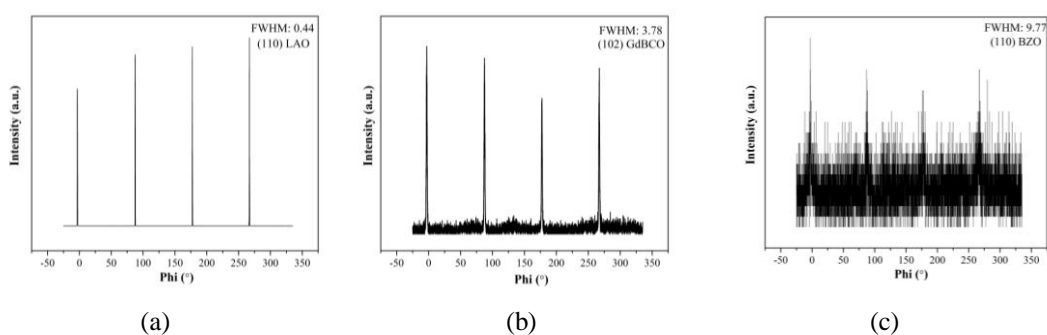


Figure 5.63 Φ -scans of (a) (110) LAO, (b) (102) GdBCO and (c) (110) BZO for film F(L-E3).

The surface morphology of the grown undoped and doped GdBCO samples was studied in detail using SEM as depicted in Figures 5.64 and 5.65. A typical pinhole surface structure was observed on all samples. On F(S-E) series films, the undoped

F(S-E0) film has a smooth, crack free surface and formed by c-axis oriented grains. BZO doped GdBCO films present a denser surface structure with decreasing porosity compared with the undoped GdBCO films. It is also straightforward to note that the film porosity is progressively reduced when the dopant concentration is increased but all doped samples have randomly dispersed a-axis orientated grains. This is a limitation for the superconducting current and it must find its way in a percolative process.

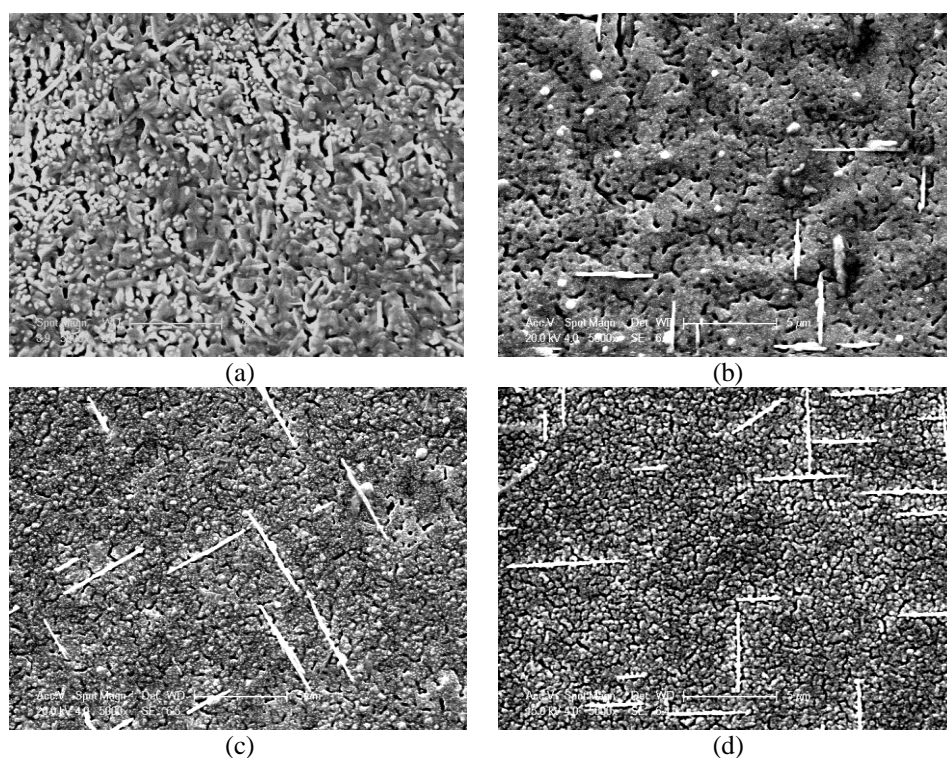


Figure 5.64 Surface morphologies of (a) F(S-E0), (b) F(S-E1), (c) F(S-E2) and (d) F(S-E3) films.

Table 5.5 Surface roughness and film thickness measurement results of samples.

Name of Film	Surface Roughness (S_a nm)	Film Thickness (nm)
F(S-E0)	2.69	221
F(S-E3)	2.45	237
F(L-E0)	3.35	229
F(L-E3)	1.67	242

On L series samples, only F(L-E2) film with a 12 mol% BZO concentration has randomly oriented a-axis grains on the sample surface. On the other hand, 18 mol%

BZO doped sample surface has finer sized grains in comparison to the large grains of 6 and 12 mol% BZO doped sample surfaces. Generally, all these images show that the surfaces are smooth with high density and the grains are grown as large as interconnected platelets that lie parallel to the surface.

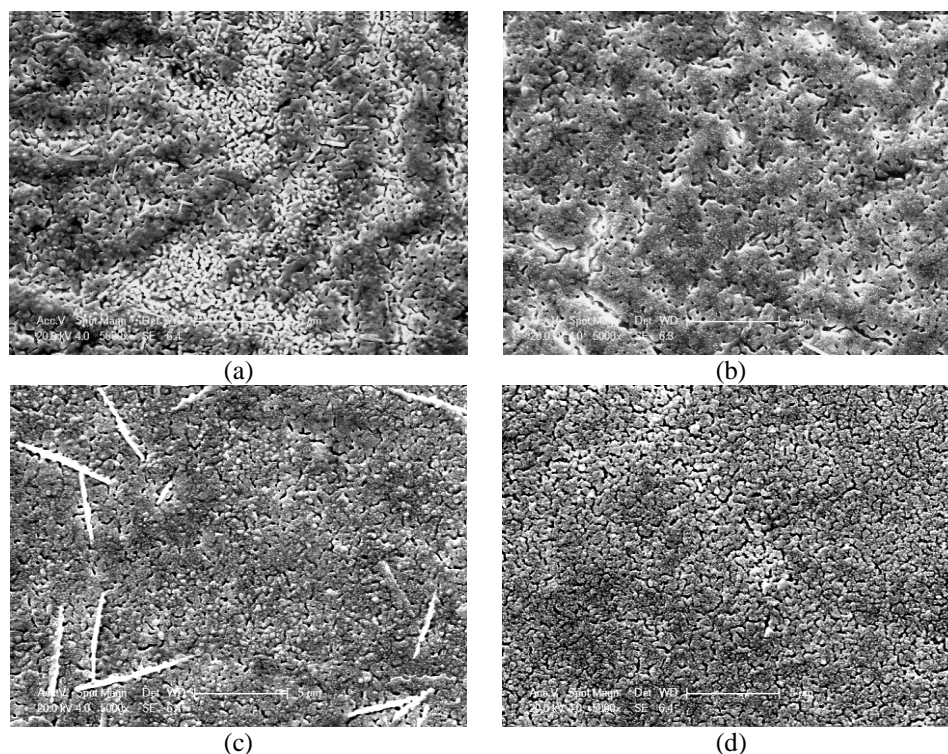


Figure 5.65 Surface morphologies of (a) F(L-E0), (b) F(L-E1), (c) F(L-E2) and (d) F(L-E3) films.

The AFM characterization was also performed to the samples for surface roughness and film thickness determination. The average surface roughness (S_a) of the films were determined in a scan area of $20\ \mu\text{m} \times 20\ \mu\text{m}$. All S_a values and film thicknesses are listed in Table 5.5. AFM scans of F(S-E0), F(S-E3), F(L-E0) and F(L-E3) films are shown in Figure 5.66. The a-axis grain oriented grain structure of 18 mol% BZO doped GdBCO film on STO substrate is more discernible in the AFM image. AFM images for all samples are compatible with SEM surface morphology investigations. It was determined that all film thickness values are in the range of 220-240 nm and average roughness values of doped samples have declining trend.

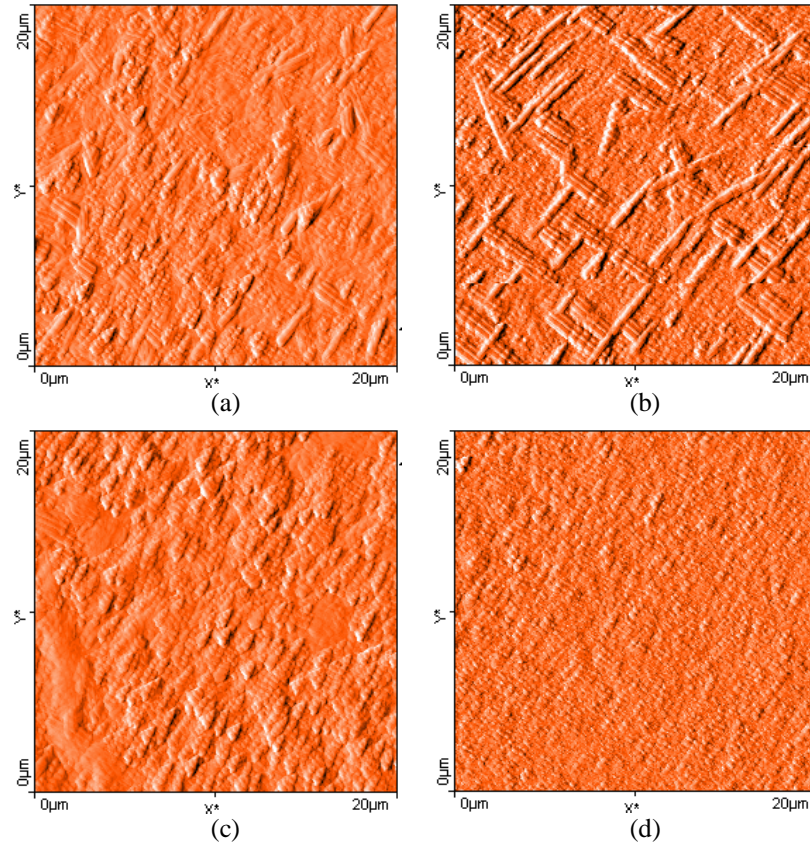


Figure 5.66 AFM images of (a) F(S-E0), (b) F(S-E3), (c) F(L-E0) and (d) F(L-E3) films.

5.3.4 Superconducting Properties of GdBCO Thin Films with BZO Pinning Centers

The dependence of inductively measured critical transition temperature (T_c) and transition width (ΔT_c) on the amount of BZO in the structure are shown for S-series samples in Figure 5.67 (a) and for L-series samples in Figure 5.68 (a). The data indicate that the highest critical temperatures for the GdBCO thin films were accomplished with values of 93.1 K and 93.2 K for F(S-E0) and F(L-E0) films, respectively. As a general trend, the T_{c90} value for all samples decreases monotonously with increasing dopant concentration in the structure. Zr diffusion into GdBCO and substitution on gadolinium (Gd) sites is the reason for lowered T_{c90} as discussed in the previous parts of this chapter. Depending on this, F(S-E3) and F(L-E3) films have the highest ΔT_c values which indicate the higher inhomogeneity of them.

Inductive measurements of the critical current density (J_c) at 77 K in self-field was performed for all samples and the results are given in Figure 5.67 (b) and 5.68 (b). It is shown that the highest J_c 's are 2.53 MA/cm² and 1.96 MA/cm² for undoped GdBCO samples of S-series and L-series, respectively.

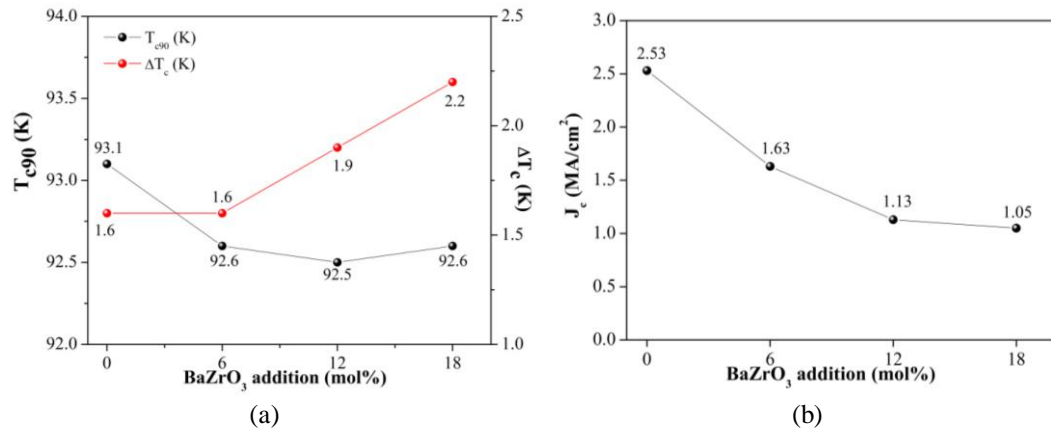


Figure 5.67 Dependence of inductively measured (a) critical transition temperature (T_{c90}) and transition width (ΔT_c), (b) critical current density (J_c) on amount of BZO for all samples prepared on STO substrates.

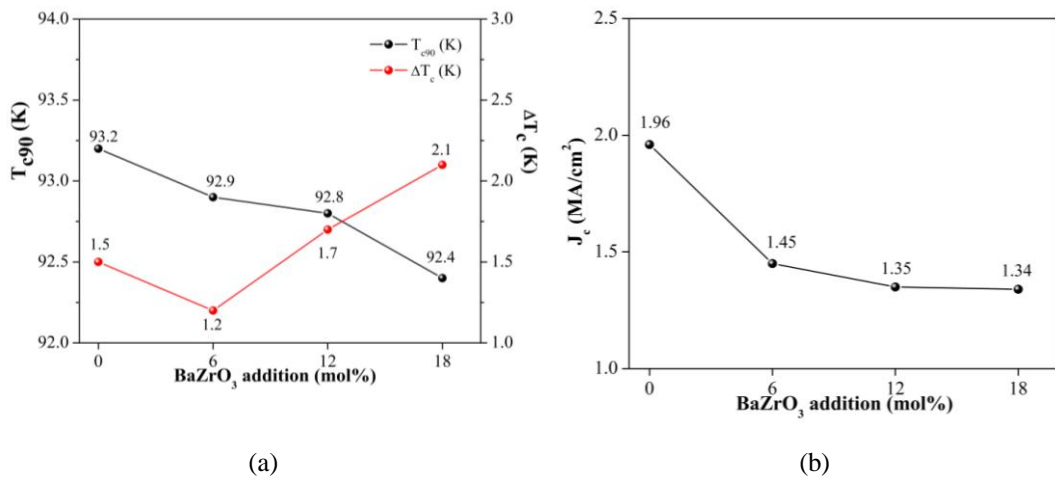


Figure 5.68 Dependence of inductively measured (a) critical transition temperature (T_{c90}) and transition width (ΔT_c), (b) critical current density (J_c) on the amount of BZO for all samples prepared on LAO substrates.

It is required that REBCO coated conductors have a high critical current density under a magnetic field at the liquid nitrogen temperature 77 K comparable to conventional metallic superconductors at 4.2 K (Haruta et al., 2006). In order to

observe the influence of dopant to the superconducting properties it is required to carry out critical current measurements under magnetic field conditions. The dependence of J_c on the magnetic field applied parallel to the c-axis up to 9 T or 6 T at 77 K for the GdBCO films containing 6, 12 and 18 mol% BZO are shown in Figures 5.70 (a) and 5.71 (a).

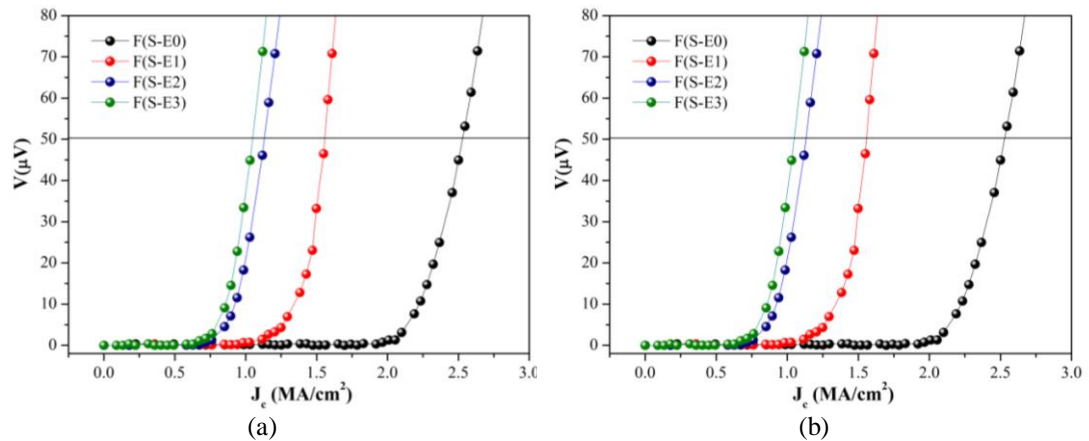


Figure 5.69 Inductive critical current density (J_c) measurements of undoped and BZO doped GdBCO samples at 77 K in self-field on (a) STO and (b) LAO substrates.

It is decided to perform transport measurements for samples on both STO and LAO substrates because of their similar inductive measurement results. It is clear that the 12 mol% BZO doped GdBCO sample on STO substrate has the highest J_c value for all magnetic fields. At fields lower than 2 T, the 18 mol% doped sample has higher J_c value than 6 mol% and undoped sample, but the drop rate of it is quite fast and J_c becomes lower at higher fields than 2 T. For the L series samples, F(L-E1) and F(L-E2) possesses more or less same J_c values up to 4 T, and then there is a slight increase at the J_c of F(L-E1) up to 6 T.

Within two sample groups the values of J_c are enhanced on 6 and 12 mol% BZO doped samples. This fact indicates that effective pinning centres have been introduced in terms of the BZO doping. Nevertheless, the 18 mol% doped GdBCO film has the lowest J_c value especially at high fields which means that the superconducting structure of GdBCO film is destroyed; self-field and in-field properties are suppressed with the excess amount of dopant concentration.

The overall increase in J_c at all magnetic fields is more clear seen when the magnetic field dependence of the pinning force, $F_p = J_c(B) \times B$, is presented in Figure 5.70 (b) and 5.71 (b). Even though J_c decreases monotonically with increasing field, F_p increases to a maximum value $F_{p \max} = 1.35 \text{ GN/m}^3$ at the field of 4 Tesla for F(S-E2) film and 1.3 GN/m^3 at the field of 1.5 Tesla for F(L-E1) film.

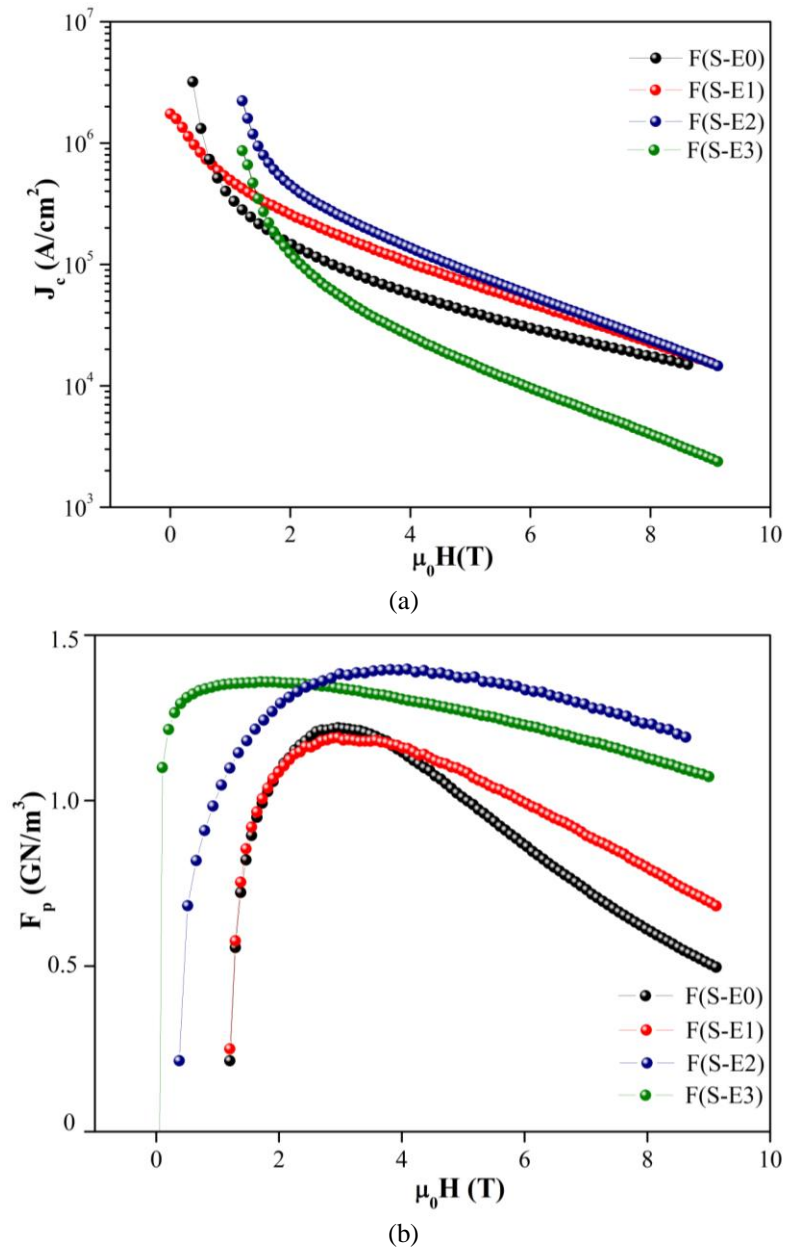
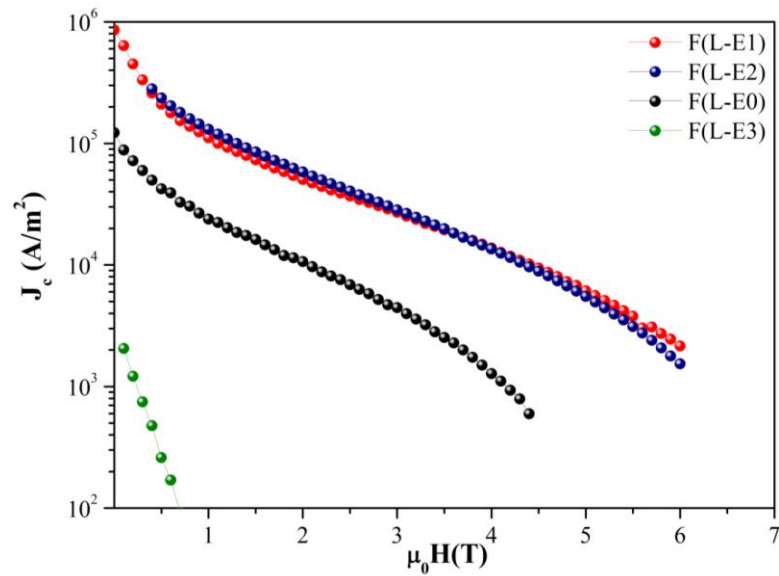
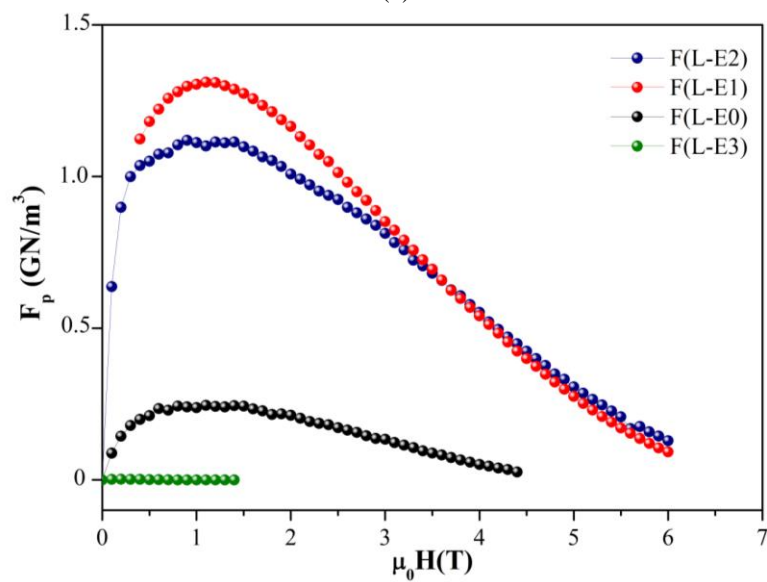


Figure 5.70 (a) Field dependence of the critical current density and (b) pinning force density up to 9 T at 77 K for F(S-E) group of films.



(a)



(b)

Figure 5.71 (a) Field dependence of the critical current density and (b) pinning force density up to 6 T at 77 K for F(L-E) group of films.

CHAPTER SIX

CONCLUSIONS AND FUTURE PLANS

YBCO and GdBCO superconducting thin films were successfully prepared from different kinds of solutions via TFA-MOD method on STO and LAO single crystal substrates and BZO was incorporated into the structures of them as artificial pinning centers. Fundamental structural and electrical properties of these films were investigated to determine the effect of solvent and BZO dopant concentration to the structure. The summarized results can be outlined as follows:

1) In solution characteristics, contact angle and rheological properties of YBCO and GdBCO based solutions were investigated. Contact angle values of all solutions are lower than 90° ; therefore it is possible to express that these solutions can wet the single crystal substrates. Higher contact angle values may lead to thicker films with high stress concentration regions. A detailed rheological characterization was performed to determine shear profile and scrutinize effect of temperature on viscosity. For all solutions, viscosity value is low at slow shear rates but it increases and stays nearly constant with increasing shear rate. For the measurements performed under increasing temperature conditions, it is possible to point out that viscosity is independent from the shear rate and stays nearly constant with increasing shear rate or temperature values.

2) For the process optimization, proper heat treatment regime was determined as a combination of DTA-TG, and FTIR results. During the heat treatment process, dry gas treatment up to 60°C prevents the gel film from absorbing humidity that would deteriorate film integrity. Above 60°C , humidified O_2 is introduced to suppress the sublimation of Cu trifluoroacetate. Metal trifluoroacetates decompose and harmful gaseous residues are removed during the pyrolysis to give a precursor film. After that, the fluoride containing precursor film is fired at a maximum temperature of 780°C under humidified N_2 mixed with 100 ppm O_2 and then oxygenated at 450°C to obtain the final superconducting film.

3) In order to determine the structure and growth orientation of the films, XRD was performed on the YBCO and GdBCO films. In XRD patterns, generally the major peaks correspond to the (001) reflections of the YBCO and GdBCO phases and (100) STO or LAO substrate which indicates that the films have a strong c-axis texture. BZO (200) peaks are very weak compared with the YBCO and GdBCO (001) peaks and the intensities of BZO (200) increases slightly with increasing BZO concentration. The textured structure of many films deteriorates with increasing BZO concentration and (103) orientation of YBCO or GdBCO becomes observable. Additional to different orientation, there are also some impurity phases as Y_2O_3 / Gd_2O_3 and $BaCO_3$ in the structures of films. These kinds of unwanted phases may affect the textured structure of films.

4) Texture measurements were also performed parallel to phase analysis. In the (102) pole figures of both films, the presence of only one sharp peak with fourfold symmetry confirms the epitaxial growth of YBCO and GdBCO films on to the STO and LAO substrates. (110) pole figure reflections of BZO phase on STO and LAO substrates explain us that BZO nanoparticles are randomly oriented and distributed within the matrix. The FWHM values of phi scans for (102) reflections of YBCO and GdBCO films are at most ~ 2 that these values confirm the good degree of epitaxial growth of YBCO and GdBCO films on STO and LAO substrates. The ϕ -scan for BZO peak gives a wide-angle intensity distribution with FWHM is 3.97 and 11.51 for YBCO samples and 8.74 and 9.77 for GdBCO samples suggesting a highly random orientation distribution of these particles in the oriented structure on STO and LAO substrates.

5) The surface morphologies and characteristics of YBCO and GdBCO films on single crystal STO and LAO substrates were examined by using SEM and AFM. The surface morphologies of all samples generally exhibit continuous and flat surfaces with the characteristic porosity and outgrowths of the c-axis growth. the presence of some a-axis oriented grains is denoted by needle-shape grains with average size of 1-2 μm . In our samples, broadly speaking BZO doped YBCO films present a denser surface structure with decreasing porosity compared with the undoped YBCO and

GdBCO films. F(L-D3) is the only exception which has a larger grain size with higher porosity concentration. Additionally, all doped samples of GdBCO films have randomly dispersed a-axis orientated grains. This is a limitation for the superconducting current it is possible to detect the influence of a-axis growth and porosity through measurements of T_c and J_c .

6) The dependence of inductively measured critical transition temperature (T_c) and transition width (ΔT_c) on the amount of BZO in the structure were measured for all samples. For the samples prepared on STO and LAO substrates from methanol and ethanol-based solutions, there is not a noteworthy result of measurements which can be generalized. The T_{c90} values of samples prepared from propionic acid based solutions (S-D) decreases with increasing dopant concentration from 90.05 to 88.15 K whereas ΔT_c value is increasing from 0.75 to 2.05 K. The data for the GdBCO thin films indicate that the highest critical temperatures were achieved with values of 93.1 K and 93.2 K for samples F(S-E0) and F(L-E0), respectively. As a general trend, the T_{c90} value for all samples decreases monotonously with increasing dopant concentration in the structure. Zr diffusion into REBCO and substitution on RE (Y or Gd) sites is the reason for lowered T_{c90} .

7) Inductive measurements of the critical current density (J_c) at 77 K in self-field was performed for all samples. Samples prepared from methanol and ethanol-based solutions on STO and LAO substrates exhibit fluctuating J_c values with increasing dopant concentration. Only samples prepared from propionic acid based solutions on STO and LAO substrates have continuously decreasing J_c values with BZO concentration. It is shown that the highest J_c 's are 3.15 MA/cm² and 2.82 MA/cm² for undoped YBCO samples of S-series and L-series, 2.53 MA/cm² and 1.96 MA/cm² for undoped GdBCO samples of S-series and L-series, respectively. This is an expected effect for self-field conditions and further effects of BZO in in-field conditions are determined by transport measurements.

8) As a result of T_c and self-field J_c measurements, it is concluded that F(S-D) and F(L-D) samples possess better superconducting properties which worth to perform

further measurements for YBCO samples in order to determine performance at high fields. Additionally, same measurement was also applied to the GdBCO samples on both STO and LAO substrates. 6 mol% BZO doped YBCO samples (F(S-D1) and F(L-D1)) possess the highest J_c value for all magnetic fields. F_p increases to a maximum value $F_{p \max} = 2.5 \text{ GN/m}^3$ at the field of 1.5 T for sample F(S-D1) and 1.70 GN/m^3 at the field of 1.5 T for sample F(L-D1). According to the measurement results of GdBCO samples, the 12 mol % BZO doped GdBCO sample on STO substrate has the highest J_c value for all magnetic fields. For the L series samples, F(L-E1) and F(L-E2) possesses more or less same J_c values up to 4 T, and then there is a slight increase at the J_c of F(L-E1) up to 6 T. Although J_c decreases monotonically with increasing field, F_p increases to a maximum value $F_{p \max} = 1.35 \text{ GN/m}^3$ at the field of 4 T for F(S-E2) sample and 1.3 GN/m^3 at the field of 1.5 T for sample F(L-E1). Within all the samples, the 18 mol % doped samples have the lowest J_c value even at high fields which means that the superconducting structure of are destroyed; self-field and in-field properties are suppressed with the excess amount of dopants concentration.

Since superconductivity is a wide field of science and still has some unknown points, it is possible to extend this work further. As a future plan, first of all, it is possible to use different rare earth elements instead of yttrium to observe the superconductivity parameters. Also, there are many artificial pinning center possibilities such as BaHfO_3 , BaIrO_3 and BaSnO_3 other than BaZrO_3 . It worths to measure their effect in thin film structure and for further characterization transmission electron microscopy (TEM) investigation is required to determine size, shape and distribution of these APC particles.

The experimental results discussed in the thesis show that the critical current carrying capability is highly sensitive to the morphology of the film. Because of this reason, a well-aligned and homogeneous surface morphology is needed for thin films. Polymer addition (PVB, PVP, PEG, etc.) in the precursor solution may modify the surface morphology, form a denser surface structure by decreasing porosity and eliminate the obstacles for current flow.

To conclude, the transfer of superconducting thin films to the industrial applications such as superconducting power transport cables, superconducting generators, bolometers, etc. is the main aim of the studies in this field. After optimising all parameters, it is going to be possible to prepare prototip applications of these films.

REFERENCES

- Abrikosov, A. A. (1957). *Zhurnal Eksperimentalnoi I Teoreticheskoi Fiziki*, 32, 1442-1446.
- Alecu, G. (2004). Crystal structures of some high-temperature superconductors. *Romanian Reports in Physics*, 56, 404-412.
- Araki, T., & Hirabayashi, I. (2003). Review of a chemical approach to $\text{YBa}_2\text{Cu}_3\text{O}_{7-x}$ coated superconductors-metal organic deposition using trifluoroacetates. *Superconductor Science and Technology*, 16, R71-R94.
- Bardeen, J., Cooper, L. N., & Schrieffer, J. R. (1957). Microscopic theory of superconductivity. *Physical Review*, 106, 162-164.
- Barnes, H. A., Hutton, J. E., & Walters, K. (1989). *An introduction to rheology*. Amsterdam: Elsevier Science Publishers B.V.
- Bednorz, J. G., & Müller, K. A. (1987). Perovskite-type oxides -the new approach to high- T_c superconductivity. *Nobel Lecture*, 1-34.
- Breeze, S. R., & Wang, S. (1999). The preparation of YBCO epitaxial superconducting films by a chemical solution deposition process. *Journal of Materials Science*, 34, 1099-1106.
- Bhuiyan, M. S., Paranthaman, M., & Salama, K. (2006). Solution-derived textured oxide thin films-a review. *Superconductor Science and Technology*, 19, R1-R21.
- Cai, C., Hänisch, J., Gemming, T., & Holzapfel, B. (2005). Anisotropic enhancement of flux pinning in mixed rare earth 123-type thin films. *IEEE Transactions on Applied Superconductivity*, 15, 3738-3741.

- Cai, C., Holzapfel, B., Hanisch, J., Fernandez, L., & Schultz, L. (2004). Magnetotransport and flux pinning characteristics in $\text{RBa}_2\text{Cu}_3\text{O}_{7-d}$ (R=Gd, Nd, Eu) and $(\text{Gd}_{1/3}\text{Eu}_{1/3}\text{Nd}_{1/3})\text{Ba}_2\text{Cu}_3\text{O}_{7-d}$ high- T_c superconducting thin films on SrTiO_3 (100). *Physical Review B*, 69 (104531), 1-5.
- Callister D. W. (2000). *Materials science and engineering an introduction* (5). USA: Wiley.
- Campbell, A M., & Evetts, J. E. (1972). Flux vortices and transport currents in type II superconductors. *Advances in Physics*, 21, 199-428.
- Castano, O., Cavallaro, A., Palau, A., Gonzales, C., Rossell, M., Puig, T., et al. (2003). High quality $\text{YBa}_2\text{Cu}_3\text{O}_7$ thin films grown by trifluoroacetates metalorganic deposition. *Superconductor Science and Technology*, 16, 45-53.
- Castano, O., Cavallaro, A., Palau, A., Gonzales, J. C., Rossell, M., Puig, T., et al. (2003). Influence of porosity on the critical currents of trifluoroacetate-mod $\text{YBa}_2\text{Cu}_3\text{O}_7$ films. *IEEE Transactions on Applied Superconductivity*, 13, 2504-2507.
- Cavallaro, A. (2005). *Optimisation of CSD buffer layers for $\text{YBa}_2\text{Cu}_3\text{O}_7$ coated conductor development*. Barcelona University, Graduate School of Natural and Applied Sciences, PhD Thesis.
- Chen, Y., Selvamanickam, V., Zhang, Y., Zuev, Y., Cantoni, C., Specht, E., et al. (2009). Enhanced flux pinning by BaZrO_3 and $(\text{Gd},\text{Y})_2\text{O}_3$ nanostructures in metal organic chemical vapor deposited GdYBCO high temperature superconductor tapes. *Applied Physics Letters*, 94 (062513), 1-3.
- Clem, J. R. (1991). Two-dimensional vortices in a stack of thin superconducting films: a model for high-temperature superconducting multilayers. *Physical Review B*, 43, 7837-7846.

- Cyrot, M., & Pavuna, D. *Introduction to superconductivity and high T_c materials*. (1995). Singapore; London: World Scientific.
- Dam, B., Huijbregtse, J. M., Klaassen, F. C., van der Geest, R. C. F., Doornbos, G., & Rector, J. H. (1999). Origin of high critical currents in $\text{YBa}_2\text{Cu}_3\text{O}_{7-\delta}$ superconducting thin films. *Nature*, 399, 439-442.
- Evetts, J. E., & Datta, T. (1992). Oxide Superconductors: Physical Properties. In *Concise Encyclopedia of Superconducting and Magnetic Materials*.
- Durrell, J. H. (2001). *Critical current anisotropy in high temperature superconductors*. University of Cambridge, Graduate School of Natural and Applied Sciences, PhD Thesis.
- Engel, S., Thersleff, T., Hühne, R., Schultz, L., & Holzappel, B. (2007). Enhanced flux pinning in $\text{YBa}_2\text{Cu}_3\text{O}_7$ layers by the formation of nanosized BaHfO_3 precipitates using the chemical deposition method. *Applied Physics Letters*, 90 (102505) 1-3.
- Essmann, U., & Trauble, H. (1967). The direct observation of individual flux lines in type II superconductors. *Physics Letters A*, 24, 526-527.
- Fang, S. C., Huang, C. H., Chen, I. C., Liaw, C. F., & Hurng, W. M. (1994). Preparation of ybco superconductor thin film by spin-coating method with metal-organic precursors. *Journal of Materials Science*, 29, 99-102.
- Feenstra, R., Lindemer, T. B., Bundai, J. D., & Galloway, M. D. (1991). Effect of oxygen pressure on the synthesis of $\text{YBa}_2\text{Cu}_3\text{O}_{7-x}$ thin films by post-deposition annealing. *Journal of Applied Physics*, 69, 6569-6585.

- Finlayson, A. P., Mouganie, T., Cordero-Cabrera, M. C., & Glowacki, B. A. (2007). Phase transformation analysis throughout an anhydrous fluorine based sol-gel YBCO processing route. *Materials Chemistry and Physics*, *105*, 99-104.
- Fukushima, H., Ibi, A., Takahashi, H., Kuriki, R., Miyata, S., Yamada, Y., et al. (2007). Properties of long GdBCO coated conductor by IBAD-PLD method-the first GdBCO coil test. *IEEE Transactions on Applied Superconductivity*, *17*, 3367-3370.
- Gazquez, J., Sandiumenge, F., Coll, M., Pomar, A., Mestres, N., Puig, T., et al. (2006). Precursor evolution and nucleation mechanism of $\text{YBa}_2\text{Cu}_3\text{O}_x$ films by TFA metal-organic decomposition. *Chemistry of Materials*, *18*, 6211-6219.
- Ginzburg, V. L., & Landau L. D. (1950). *Zhurnal Eksperimentalnoi I Teoreticheskoi Fiziki*, *20*, 1064-1084.
- Goebel, G. (2005). *Superconductivity*, Public Domain, Retrieved May 8, 2006 from <http://www.vectorsite.net/ttspon.html>.
- Gonzales, J. C. (2005). *Coated conductors and chemical solution growth of ybco films: a micro-Raman spectroscopy study*. Barcelona University, Graduate School of Natural and Applied Sciences, PhD Thesis.
- Gupta, A., Jagannathan, R., Cooper, E. I., Giess, E. A., Landman, J. I. & Hussey, B. W. (1988). Superconducting oxide films with high transition temperature prepared from metal trifluoroacetate precursors. *Applied Physics Letters*, *52*, 2077-2082.
- Gutierrez, J., Llordes, A., Gazquez, J., Gibert, M., Roma N., Richart, S., et al., (2007). Strong isotropic flux pinning in solution-derived $\text{YBa}_2\text{Cu}_3\text{O}_{7-x}$ nanocomposite superconductor films. *Nature Materials*, *6*, 367-373.

- Haberkorn, N., Lovey, F., Condó, A. M. & Guimpel, J. (2005). High-resolution transmission electron microscopy study of the interfaces and stacking defects in superconducting/magnetic perovskite superlattices. *Journal of Applied Physics*, 97 (053511), 1-7.
- Hänisch, J., Cai, C., Stehr, V., Hühne, R., Lyubina, J., Nenkov, K., et al. (2006). Formation and pinning properties of growth-controlled nanoscale precipitates in $\text{YBa}_2\text{Cu}_3\text{O}_{7-\delta}$ /transition metal quasi-multilayers. *Superconductor Science and Technology*, 19, 534-540.
- Harrington, S. A., Durrell, J. H., Maiorov, B., Wang H., Wimbush, S. C., & Kursumovic, A. (2009). Self-assembled, rare earth tantalate pyrochlore nanoparticles for superior flux pinning in $\text{YBa}_2\text{Cu}_3\text{O}_{7-x}$ films. *Superconductor Science and Technology*, 22 (022001), 1-7.
- Haruta, M., Fujiyoshi, T., Sueyoshi, T., Dezaki, K., Ichigosaki, D., Miyahara, K., et al. (2006). Flux pinning properties of $\text{ErBa}_2\text{Cu}_3\text{O}_y$ thin films with BaZrO_3 nanorods. *Superconductor Science and Technology*, 19, 803-807.
- Haugan, T., Barnes, P. N., Wheeler, R., Meisenkothen, F. & Sumption, M. (2004). Addition of nanoparticle dispersions to enhance flux pinning of the $\text{YBa}_2\text{Cu}_3\text{O}_{7-x}$ superconductor. *Nature*, 430, 867-870.
- Hogg, M. J. (1999). *Vortex dynamics and flux pinning in YBCO low-angle grain boundaries*, University of Cambridge, Graduate School of Natural and Applied Sciences, PhD Thesis.
- Honjo, T., Fuji, H., Huang, D., Nakamura, Y., Izumi, T., & Shiohara, Y. (2001). Preparation of $\text{REBa}_2\text{Cu}_3\text{O}_{7-x}$ films grown by metal trifluoroacetate precursors. *Physica C*, 357-360, 999-1002.

- Honjo, T., Nakamura, Y., Teranishi, R., Tokunaga, Y., Fuji, H., Shibata, J., et al. (2003). Fabrication and growth mechanism of YBCO coated conductors by TFA-MOD process. *Physica C*, 392-396, 873-881.
- Hott, R. (2003). Application fields of high-temperature superconductors. In *High temperature superconductivity 2- Engineering applications* (35-48). Berlin: Springer.
- Iguchi, T., Araki, T., Yamada, Y., Hirabayashi, I. & Ikuta, H. (2002). Fabrication of Gd-Ba-Cu-O films by the metal-organic deposition method using trifluoroacetates. *Superconductor Science and Technology*, 15, 1415-1420.
- Inam, A., Hegde, M. S., Wu, X. D., Venkatesan, T., England, P., Miceli, P. F., et al. (1988). As-deposited high T_c and J_c superconducting thin films made at low temperatures. *Applied Physics Letters*, 53 (10), 908-910.
- Jin, L. H., Zhang, Y., Yu, Z. M., Yan, G., Li, C. S., Lu, Y. F., et al. (2010). Effect of relative humidity on morphology of YBCO films prepared by CSD method. *Physica C*, 470, 1257-1260.
- Jooss, C., Warthmann, R., & Kronmüller H. (2000). Pinning mechanism of vortices at antiphase boundaries in $YBa_2Cu_3O_{7-\delta}$. *Physical Review B*, 61, 12433-12446.
- Jooss, C., Warthmann, R., Kronmüller, H., Haage, T., Habermeier, H. U. & Zegenhagen, J. (1999). Vortex pinning due to strong quasiparticle scattering at antiphase boundaries in $YBa_2Cu_3O_{7-\delta}$. *Physical Review Letters*, 82, 632-635.
- Kaneko, A., Matsuda, J., Teranishi, R., Nakaoka, K., Aoki, Y., Fuji, H., et al. (2005). Fabrication of $Y_{1-x}RE_xBa_2Cu_3O_{7-y}$ film by advanced TFA-MOD process. *Physica C*, 426-431, 949-953.

- Kim, B. J., Lim, S. W., Kim, H. J., Hong, G. W. & Lee, H. G. (2006). New MOD solution for the preparation of high J_c REBCO superconducting films. *Physica C*, 445-448, 582-586.
- Kitoh, Y., Matsuda, J., Suzuki, K., Nakaoka, K., Sutoh, Y., Nakai, A., et al. (2007). Effect of metal composition ratios of solutions on J_c -B properties of REBCO coated conductors fabricated by advanced TFA-MOD process. *Physica C*, 463-465, 523-526.
- Knoth, K., Engel, S., Apetrii, C., Falter, M., Schlobach, B., Hühne, R., et al. (2006). Chemical solution deposition of $YBa_2Cu_3O_{7-x}$ coated conductors. *Current Opinion in solid State and Materials Science*, 10, 205-216.
- Lee, J. W., Shin, G. M., Moon S. H. & Yoo S. I. (2010). High- J_c $GdBa_2Cu_3O_{7-\delta}$ films fabricated by the metal-organic deposition process. *Physica C*, 470, 1253-1256.
- Li, Y., Geerk, J., Smithy, R., Liu, X., & Xu, J. (1997). Optimization of T_c of epitaxial $GdBaCuO$ growth superconducting thin film by inverted cylindrical sputtering. *Physica C*, 282-287 (2), 625-626.
- Lim, J. H., Jang, S. H., Kim, J. H, Kim, K. T., Joo, J., Jung, S. B., et al. (2005). Fabrication of YBCO coated conductor by TFA-MOD method in route of dissolving Y211 and $Ba_3Cu_5O_8$ powders in TFA. *Physica C*, 426-431, 973-978.
- Llordes, A., Zalamova, K., Ricart, S., Puig, T., Hardy, A., & Obradors, X. (2010). Evolution of metal-trifluoroacetate precursors in the thermal decomposition toward high-performance $YBa_2Cu_3O_7$ superconducting films. *Chemistry of Materials*, 22 (5), 1686-1694.
- London, F., & London, H. (1935). The electromagnetic equations of the supraconductor. *Proceedings of the Royal Society A*, 149 (866), 71-88.

- MacManus-Driscoll, J. L., Foltyn, S. R., Jia, Q. X., Wang, H., Serquis, A., Civale, L., et al. (2004). Strongly enhanced current densities in superconducting coated conductors of $\text{YBa}_2\text{Cu}_3\text{O}_{7-x} + \text{BaZrO}_3$. *Nature Materials*, 3, 439-443.
- Maiorov, B., Baily, S. A., Zhou, H., Ugurlu, O., Kennison, J. A., Dowden, P. C., et al. (2009). Synergetic combination of different types of defect to optimize pinning landscape using BaZrO_3 -doped $\text{YBa}_2\text{Cu}_3\text{O}_7$. *Nature Materials*, 8, 398-404.
- Malkin, A. Y. (1994). *Rheology Fundamentals*. Canada: ChemTec Publishing.
- Mele, P., Matsumoto, K., Horide, T., Ichinose, A., Mukaida, M., Yoshida, Y., et al. (2008). Ultra-high flux pinning properties of BaMO_3 -doped $\text{YBa}_2\text{Cu}_3\text{O}_{7-x}$ thin films ($M = \text{Zr}, \text{Sn}$). *Superconductor Science and Technology*, 21, 032002.
- Miyachi, K., Sudoh, K., Ichino, Y., Yoshida, Y., & Takai, Y. (2003). The effect of the substitution of Gd for Ba site on $\text{Gd}_{1+x}\text{Ba}_{2-x}\text{Cu}_3\text{O}_{6+\delta}$ thin films. *Physica C*, 392-396, 1261-1264.
- Onnes, H. K. (1911). The Superconductivity of mercury. *Comm. Phys. Lab. Univ. Leiden*, 122-124.
- Owens, F. J., & Poole, C. P. Jr. (1996). *The new superconductors*. New York: Plenum Press.
- Petrisor, T., & Ciontea, L. (2006). The development of mod-tfa precursors for the deposition of thick YBCO films on metallic substrates for the superconducting coated conductors fabrication. In *Magnet structure and integration, Annual report of the EURATOM-MedC association*. (97-103). Cluj- Napoca.
- Pinol, S. & Castano, O. (2006). Water vapour pressure influence on the kinetics of the superconducting YBCO thin films epitaxial growth by the TFA–MOD method, *Physica C*, 450, 48-55.

- Puig, T., Gonzalez, J. C., Pomar, A., Mestres, N., Castano, O., Coll, M., et al. (2005). Influence of growth conditions on the microstructure and critical currents of TFA-MOD $\text{YBa}_2\text{Cu}_3\text{O}_7$ films. *Superconductor Science and Technology*, 18, 1141-1150.
- Reich, E., Thersleff, T., Hühne, R., Iida K., Schultz L., & Holzapfel, B. (2009). Structural and pinning properties of $\text{Y}_2\text{Ba}_4\text{CuMO}_y$ (M=Nb,Zr)/ $\text{YBa}_2\text{Cu}_3\text{O}_{7-x}$ quasimultilayers fabricated by off-axis pulsed laser deposition. *Superconductor Science and Technology*, 22, 105004.
- Roas, B., Hensel, B., Endres, G., Schultz, L., & Saemann-Ischenko, G. (1989). Superconducting properties of irradiation-induced effects in epitaxial YBaCuO thin-films. *Thin Solid Films*, 174, 179-183.
- Roas, B., Schultz, L., & Endres, G. (1988). Epitaxial growth of $\text{YBa}_2\text{Cu}_3\text{O}_{7-x}$ thin films by a laser evaporation process. *Applied Physics Letter*, 53, 1557-1559.
- Rosenzweig, St., Hänisch, J., Hühne, R., Holzapfel, B., Schultz, L. (2010). T_c optimisation of $\text{GdBa}_2\text{Cu}_3\text{O}_7$ thin films grown by pulsed laser deposition. *Journal of Physics: Conference Series*, 234, 1-5.
- Roma, N., Morlens, S., Ricart, S., Zalamova, K., Moreto, J. M., Pomar, A., et al. (2006). Acid anhydrides: a simple route to highly pure organometallic solutions for superconducting films. *Superconductor Science and Technology*, 19, 521-527.
- Rutters, N. (2001). *Microstructural development and superconducting parameters of the $\text{YBa}_2\text{Cu}_3\text{O}_{7-\delta}$ coated conductor*. University of Cambridge, Graduate School of Natural and Applied Sciences, PhD Thesis.
- Schlesier, K., Huhtinen, H., Granroth, S. & Paturi, P. (2010). An aging effect and its origin in GdBCO thin films. *Journal of Physics: Conference Series*, 234, 1-9.

- Schlesier, K., Huhtinen, H., Paturi, P., Stepanov, Y. P., & Laih, R. (2009). Structural and superconducting properties of undoped and BZO-doped GdBCO thin films. *IEEE Transactions on Applied Superconductivity*, *19*, 3407-3411.
- Schramm, G. (2000). *A practical approach to rheology and rheometry* (2nd ed.). Karlsruhe: Gebrueder HAAKE GmbH.
- Schwartz, R.W. (1997). Chemical Solution Deposition of Perovskite Thin Films. *Chemistry of Materials*, *9*, 2325-2340.
- Schwartz, R. W., Schneller, T., & Waser, R. (2004). Chemical solution deposition of electronic oxide films. *Comptes Rendus Chimie*, *7*, 433-461.
- Shaked, H., Keane, P. M., Rodriguez, J. C., Owen, F. F., Hitterman, R. L., & Jorgensen, J. D. (1994). *Crystal structures of the high- T_c superconducting copper-oxides*. Amsterdam: Elsevier Science B.V.
- Sheahan, T. P. (2002). Magnetism and currents in superconductors. In *The Introduction to high-temperature superconductivity*. Newyork: Kluwer Academic Publishers.
- Shekhter, R. I., Galperin, Y., Garelik, L. Y, Isacson, A. & Jonson, M. (2003). Shuttling of electrons and cooper pairs. *Journal of Physics: Condensed Matter*, *15*, R441-R469.
- Sheth, A., Schmidt, H., & Lasrado, V. (1998). Review and evaluation of methods for appication of epitaxial buffer and superconductor layers. *Applied Superconductivity*, *6*, 855-873.
- Shin, G. M., Wee, S. H., Lee, H. G., Hong, G. W., Song, K. J., Park, C., et al. (2005). Fabrication of high- J_c ybco films by the tfa-mod process using YBCO powder as precursor. *IEEE Transactions on Applied Superconductivity*, *15*, 2649-2651.

- Somwangthanaroj, A. (2010). *Rheology and polymer characterization*, from <http://pioneer.netserv.chula.ac.th/~sanongn1/course.html>.
- Song, S. H., Ko, K. P., Ko, R. K., Song, K. J., Moon, S. H., & Yoo, S. I., (2007). High- J_c GdBa₂Cu₃O₇ thin films on SrTiO₃ substrates by pulsed laser deposition. *Physica C*, 463-465, 497-500.
- Suenaga, M. (2002). BaF₂ processes for YBa₂Cu₃O₇ conductors: promises and challenges. *Physica C*, 378-391, 1045-1050.
- Sutoh, Y., Miura, M., Yoshizumi, M., Izumi, T., Miyata, S., Yamada, Y., et al. (2009). Fabrication of high I_c film for GdBCO coated conductor by continuous in-plume PLD. *Physica C*, 469, 1307-1310.
- Thersleff, T. (2011). *The nanoscale characterization of functional superconducting thin films*. Dresden University, Graduate School of Natural and Applied Sciences, PhD Thesis.
- Tinkham, M. (1996). *Introduction to Superconductivity*. McGraw Hill.
- Thuy, T., Hoste, S., Herman, G., Buysser, K. & Driessche, I. (2009). Sol-gel chemistry of an aqueous precursor solution for YBCO thin films. *Journal of Sol-Gel Science and Technology*, 52 (1), 124-133.
- Waldram, J. R. (1996). *Superconductivity of metals and cuprates*. London: IOP.
- Wang, L., Shi, D. Q., Zhu, X. B., Li, Q., Yamashita, T., Taylor, R., Barry, J. & Dou, S. X. (2010). Ethanol-based TFA-MOD method for preparation of YBCO films. *Physica C*, 470, 1016-1017.
- Warnes, W. H. (2003). *Principles of superconductivity*. ASM Handbook, Vol 2, 1030-1042. ASM International.

- Whelan, C. (2003). BCS theory of superconductivity, *Physical Review*.
- Xu, C., Hu, A., Sakai, N., Izumi, M., Hirabayashi, I. (2006). Flux pinning properties and superconductivity of Gd-123 superconductor with addition of nanosized SnO₂/ZrO₂ particles. *Physica C*, 445-448, 357-360.
- Xu, Y., & Shi, D. (n.d.). *A review of coated conductor development*. Department of Chemical and Materials Engineering, University of Cincinnati 2 Metals & Ceramics Division, Oak Ridge National Laboratory (ORNL).
- Yamada, K., Ichinose, A., Tomokiyo, Y., Shingai, Y., Matsumoto, K., Yoshida, Y., et al. (2007). Moire Fringe Analysis of BaZrO₃ Nanorods in ErBa₂Cu₃O_{7-x} Films. *Japanese Journal of Applied Physics*, 46, 708-711.
- Yamada, K., Mukaida, M., Kai, H., Teranishi, R., Ichinose, A., Kita R., et al. (2008). Transmission electron microscopy characterization of nanorods in BaNb₂O₆-doped ErBa₂Cu₃O_{7-x}. Films. *Applied Physics Letters*, 92 (112503), 1-8.
- Yamagiwa, K., Araki, T., Takahashi, Y., Hiei, H., Kim, S. B., Matsumoto, K., et al. (2001). Epitaxial growth of REBa₂Cu₃O_{7-x} films on various substrates by chemical solution deposition. *Journal of Crystal Growth*, 229, 353-357.
- Yoshida, Y., Matsumoto, K., Miura, M., Ichino, Y., Takai, Y., Ichinose, A., et al. (2006). Controlled nanoparticulate flux pinning structures in RE_{1+x}Ba_{2-x}Cu₃O_y films. *Physica C*, 445-448, 637-642.
- Zalamova, K., Roma, N., Pomar, A., Morlens, S., Puig, T., Gazquez, J., et al. (2006). Smooth Stress Relief of Trifluoroacetate Metal-Organic Solutions for YBa₂Cu₃O₇ Film Growth. *Chemistry of Materials*, 18, 5897-5906.

Zhao, G., Lei, L., Liu, X. & Chen, Y. (2008). Effect of copper content in precursor solution on the superconducting properties of YBCO films derived from low-fluorine solution. *Physica C*, 468, 2317-2321.

Zheng, D. N., Campbell, A. M., Johnson, J. D., Cooper, J. R., Blunt, F. J., & Porch, A. (1994). Magnetic susceptibilities, critical fields and critical currents of Co- and Zn-doped $\text{YBa}_2\text{Cu}_3\text{O}_7$. *Physical Review B*, 49, 1417-1426.